



UPPSALA
UNIVERSITET

*Digital Comprehensive Summaries of Uppsala Dissertations
from the Faculty of Science and Technology 1825*

Solid-State Nanopores for Sensing

From Theory to Applications

CHENYU WEN



ACTA
UNIVERSITATIS
UPSALIENSIS
UPPSALA
2019

ISSN 1651-6214
ISBN 978-91-513-0689-6
urn:nbn:se:uu:diva-384667

Dissertation presented at Uppsala University to be publicly examined in Polhemsalen, Ångströmlaboratoriet, Lägerhyddsvägen 1, Uppsala, Friday, 6 September 2019 at 13:15 for the degree of Doctor of Philosophy. The examination will be conducted in English. Faculty examiner: Professor Ulrich F. Keyser (University of Cambridge).

Abstract

Wen, C. 2019. Solid-State Nanopores for Sensing. From Theory to Applications. *Digital Comprehensive Summaries of Uppsala Dissertations from the Faculty of Science and Technology* 1825. 107 pp. Uppsala: Acta Universitatis Upsaliensis. ISBN 978-91-513-0689-6.

Nanopore based sensing technology has been widely studied for a broad range of applications including DNA sequencing, protein profiling, metabolite molecules, and ions detection. The nanopore technology offers an unprecedented technological solution to meeting the demands of precision medicine on rapid, in-field, and low-cost biomolecule analysis. In general, nanopores are categorized in two families: solid-state nanopore (SSNP) and biological nanopore. The former is formed in a solid-state membrane made of SiN_x , SiO_2 , silicon, graphene, MoS_2 , etc., while the latter represents natural protein ion-channels in cell membranes. Compared to biological pores, SSNPs are mechanically robust and their fabrication is compatible with traditional semiconductor processes, which may pave the way to their large-scale fabrication and high-density integration with standard control electronics. However, challenges remain for SSNPs, including poor stability, low repeatability, and relatively high background noise level. This thesis explores SSNPs from basic physical mechanisms to versatile applications, by entailing a balance between theory and experiment.

The thesis starts with theoretical models of nanopores. First, resistance of the open pore state is studied based on the distribution of electric field. An important concept, effective transport length, is introduced to quantify the extent of the high field region. Based on this conductance model, the nanopores size of various geometrical shapes can be extracted from a simple resistance measurement. Second, the physical causality of ionic current rectification of geometrically asymmetrical nanopores is unveiled. Third, the origin of low-frequency noise is identified. The contribution of each noise component at different conditions is compared. Forth, a simple nano-disk model is used to describe the blockage of ionic current caused by DNA translocation. The signal and noise properties are analyzed at system level.

Then, nanopore sensing experiments are implemented on cylinder SiN_x nanopores and truncated-pyramid silicon nanopores (TPP). Prior to a systematic study, a low noise electrical characterization platform for nanopore devices is established. Signal acquisition guidelines and data processing flow are standardized. The effects of electroosmotic vortex in TPP on protein translocation dynamics are excavated. The autogenic translocation of DNA and proteins driven by the pW-level power generated by an electrolyte concentration gradient is demonstrated. Furthermore, by extending to a multiple pore system, the group translocation behavior of nanoparticles is studied. Various application scenarios, different analyte categories and divergent device structures accompanying with flexible configurations clearly point to the tremendous potential of SSNPs as a versatile sensor.

Keywords: solid-state nanopore, ionic current, current blockage, effective transport length, noise, surface charge, translocation, biomolecule, electroosmotic flow, vortex, autogenic translocation, multiple nanopores

Chenyu Wen, Department of Engineering Sciences, Solid State Electronics, Box 534, Uppsala University, SE-75121 Uppsala, Sweden.

© Chenyu Wen 2019

ISSN 1651-6214

ISBN 978-91-513-0689-6

urn:nbn:se:uu:diva-384667 (<http://urn.kb.se/resolve?urn=urn:nbn:se:uu:diva-384667>)

γνωθι σεαυτόν

To myself and my beloved parents

List of Papers

This thesis is based on the following papers, which are referred to in the text by their Roman numerals.

- I **Wen C.**, Zhang Z., Zhang S.-L. (2017) Physical model for rapid and accurate determination of nanopore size via conductance measurement. *ACS Sensors*, 2:1523-1530.
- II Arjmandi-Tash H., Bellunato A., **Wen C.**, Olsthoorn R. C., Scheicher R. H., Zhang S.-L., Schneider G. F. (2018) Zero-depth interfacial nanopore capillaries. *Advanced Materials*, 30:1703602.
- III **Wen C.**, Zeng S., Li S., Zhang Z., Zhang S.-L. (2019) On rectification of ionic current in nanopores. *Analytical Chemistry* (re-submitted)
- IV **Wen C.***, Zeng S.* , Arstila K., Sajavaara T., Zhu Y., Zhang Z., Zhang S.-L. (2017) Generalized noise study of solid-state nanopores at low frequencies. *ACS Sensors*, 2:300-307.
- V **Wen C.**, Zeng S., Zhang Z., Hjort K., Scheicher R., Zhang, S.-L. (2016) On nanopore DNA sequencing by signal and noise analysis of ionic current. *Nanotechnology*, 27:215502.
- VI Zeng S.* , **Wen C.***, Solomon P., Zhang S.-L., Zhang Z. (2019) Rectification of protein translocation in truncated-pyramidal nanopores caused by the formation of electroosmotic vortex. *Nature Nanotechnology*. (re-submitted)
- VII **Wen C.**, Li S., Zeng S., Zhang Z., Zhang S.-L. (2019) Autogenic analyte translocation in nanopores. *Nano Energy*, 60:503-509.
- VIII **Wen C.**, Zeng S., Zhang Z., Zhang S.-L. (2018) Group behavior of nanoparticles translocating multiple nanopores. *Analytical Chemistry*. 90:13483-13490.

*The authors contributed equally to the work.

Reprints were made with permission from the respective publishers.

Publications not included in this thesis

- I Zeng S., **Wen C.**, Li S., Chen X., Chen S., Zhang S.-L., Zhang Z. (2019) Controlled size reduction to form solid-state nanopores via electron beam induced carbon deposition. *Nanotechnology* (submitted)
- II Zeng S.^{*}, **Wen C.**^{*}, Zhang S.-L., Zhang Z. (2019) Individually addressable nanopore array integrated with microfluidics and multiplexer. *IEEE sensor journal* (submitted)
- III Zhao J., Song M., **Wen C.**, Majee S., Yang D., Wu B., Zhang S.-L., Zhang Z.-B. (2018) Microstructure-tunable highly conductive graphene-metal composites achieved by inkjet printing and low temperature annealing. *Journal of Micromechanics and Microengineering*. 28, 035006.
- IV Zhao J., **Wen C.**, Sun R., Zhang S.-L., Wu B., Zhang Z.-B. (2019) A sequential process of graphene exfoliation and site-selective copper/graphene metallization enabled by multifunctional 1-pyrenebutyric acid tetrabutylammonium salt. *ACS Applied Materials and Interfaces*. 11, 6448-6455.
- V Zhao J., Pan R., Sun R., **Wen C.**, Zhang S.-L., Wu B., Nyholm L., Zhang Z.-B. (2019) High-conductivity reduced-graphene-oxide/copper aerogel for energy storage. *Nano Energy*. 60, 760–767.
- VI Yang H.^{*}, Li C.^{*}, Yue L., **Wen C.**, Zhang J., Wu D. (2019) Improving electrical performance of few-layer MoS₂ FETs via microwave annealing. *IEEE Electron Device Letters*. (accepted)
- VII Tseng C.-W., **Wen C.**, Huang D.-C., Lai C.-H., Chen S., Hu Q., Chen X., Xu X., Zhang S.-L., Tao Y.-T., Zhang Z. (2019) Synergy of ionic and dipolar effects by molecular design for pH sensing beyond the Nernstian limit. *Advanced Science* (submitted)

^{*}The authors contributed equally to the work.

Contents

1. Introduction.....	13
1.1. Molecular detection methods in precision medicine	13
1.2. Nanopore based sensors	14
1.3. Solid-state nanopores vs. biological nanopores	18
1.4. From sequencer to profilometer	19
1.5 Challenges in large-scale real-life applications	20
1.6. Scope of this thesis	21
2. Understanding of solid-state nanopore sensors	23
2.1. Physics of nanopore conductance	24
2.1.1. Electric field distribution in a nanopore.....	24
2.1.2. Effective transport length and conductance model.....	25
2.1.3. Effective transport length of zero-depth interfacial nanopores	30
2.1.4. Surface charge extraction from conductance measurement	31
2.2. Mechanism of rectification in nanopore ionic current.....	33
2.2.1. Steady state at a given bias voltage.....	33
2.2.2. Dependence of effective transport length on bias polarity	35
2.3. Origins of nanopore noise	40
2.3.1. Identification of noise components	40
2.3.2. Low-frequency noise properties.....	42
2.3.3. Origin of the flicker noise.....	44
2.3.4. Overall noise model.....	45
2.4. Characteristics of signal and noise	46
2.4.1. Correlation of signal amplitude to nanopore geometry	46
2.4.2. Translocation manner	49
2.4.3. Noise properties	50
2.4.4. Signal to noise ratio of nanopores	51
2.5. Summary of this chapter.....	53
3. Sensor applications of solid-state nanopores	54
3.1. Device and measurement setup.....	54
3.1.1. Device fabrication.....	54
3.1.2. Sample preparation.....	55
3.1.3. Measurement setup.....	56
3.1.4. Data acquisition	57
3.2. DNA translocation in SiN _x nanopores	59

3.3. Protein translocation in truncated-pyramid nanopores	63
3.3.1. Formation of vortex in truncated-pyramid nanopores	63
3.3.2. Influence of vortex on protein translocation	65
3.3.3. Translocation of IgG ₁ at different pH	69
3.3.4. Merits of analyzing frequency of translocation events	70
3.4. Autogenic analyte translocation in nanopores	71
3.4.1. Mechanism of nanopore generator	71
3.4.2. Electrical characterization of autogenic L-LDH translocation	73
3.4.3. Optical characterization of autogenic λ -DNA translocation	74
3.5. Group behavior of nanoparticles transiting multiple nanopores.	76
3.5.1. Simulation of a multiple pore system	77
3.5.2. Signal properties of group translocation	80
3.5.3. Group translocation behaviors under different conditions	80
3.5.4. Potential applications	83
3.6. Summary of this chapter	85
4. Summary and outlook	86
Sammanfattning på Svenska	89
Acknowledgement	93
References	96

Abbreviations

2D	Two dimensional
3D	Three dimensional
EDL	Electrical double layer
FTE	Frequency of translocation events
Ip	Isoelectric point
I-V	Current-voltage
LO	Larger opening
LPF	Low-pass filter
MspA	<i>Mycobacterium smegmatis</i> protein A
PM	Precision medicine
PMMA	Polymethyl methacrylate
PSD	Power spectrum density
PZC	Point of zero charge
RMS	Root-mean-square
RTN	Random telegraph noise
SEM	Scan electron microscope
SNR	Signal to noise ratio
SO	Small opening
STD	Standard deviation
ssDNA	Single stranded DNA
TEM	Transmission electron microscope
TPP	Truncated-pyramid nanopore
α -HL	α -hemolysin
a	Side length of nanopore
a_i (i=1..4)	Factors of noise components
a_e	Current noise parameter for electrodes
C_{chip}	Capacitance of nanopore membrane
C_{total}	Total capacitance of system
c_0	Concentration of electrolyte
c_H	High concentration of electrolyte
c_L	Low concentration of electrolyte
D_a	Diffusion coefficient of anions
D_c	Diffusion coefficient of cations
d	Dielectric loss factor
d_D	Diameter of nucleotide

d_p	Diameter of nanopore
d_s	Distance between adjacent nucleotides in DAN strand
E	Electric field intensity
e_n	Equivalent voltage noise of the amplifier input
G	Conductance
G_b	Bulk conductance
G_s	Surface conductance
F	Faraday constant
F_{EOF}	Electroosmotic force
F_{elec}	Electrophoresis force
f	Frequency
f_c	Cut-off frequency
$f_{\text{diff_a}}$	Diffusion flux of anions
$f_{\text{diff_c}}$	Diffusion flux of cations
$f_{\text{el_a}}$	Drift flux of anions
$f_{\text{el_c}}$	Drift flux of cations
h	Thickness of nanopore membrane
I	Current
I_0	Open-pore current
I_B	Bulk current
I_b	Blockage current
I_{osm}	Osmotic current
I_{redox}	Redox current
I_s	Surface current
I_{sc}	Short circuit current
k	Boltzmann constant
L_{acc}	Effective transport length of access region
L_{eff}	Effective transport length
N	Number of pores
N_A	Avogadro constant
$N_{\text{C(S/B)}}$	Total number of conducting carriers (in EDL/bulk region)
q	Elementary charge
R	Resistance
R_g	Gas constant
$R_{a,o}$	Access resistance at open-pore state
$R_{a,b}$	Access resistance at blockage state
R_{in}	Internal resistance of nanopore system
$R_{p,o}$	Pore resistance at open-pore state
$R_{p,b}$	Pore resistance at blockage state
$R_{t,o}$	Total resistance at open-pore state
$R_{t,b}$	Total resistance at blockage state
RF	Rectification factor
S	Selectivity of ion flux
S_0	Minimum cross-section area

S_I	Equi-field hemisphere area
S_I	Current noise PSD
S_{IB}	PSD of current flicker noise from bulk conductance
S_{IC}	PSD of current capacitive noise
S_{ID}	PSD of current dielectric noise
S_{IE}	PSD of current noise from electrodes
S_{IS}	PSD of current flicker noise from surface conductance
S_{IT}	PSD of current thermal noise
S_N	Total PSD of N nanopores
S_i	PSD of i^{th} nanopore in N pore array
$S_{i,j}$	Cross PSD of ionic current from i^{th} and j^{th} pores
T	Temperature
t_+	Transfer number of cations
U	Bias voltage
V_{oc}	Open circuit voltage
V_{osm}	Osmotic voltage
V_{redox}	Redox voltage
v	Translocation speed
α_H	Hooge parameter
β	Exponent of f of $1/f$ -shape noise
γ	Activity coefficient of electrolyte
Δc	Build-in concentration different
ΔI_{\max}	Maximum current change
ΔI_{\min}	Minimum current change
ΔR_p	Resistance change caused by single nucleotide blockage in pore region
ΔR_a	Resistance change caused by single nucleotide blockage in access region
ζ	Ratio of the diffusion coefficients of anion and cation
θ	Angle of nanopore sloped sidewall
μ_a	Mobility of anions
μ_c	Mobility of cations
v	Weighting factor
ρ	Resistivity of electrolyte
σ	Surface charge density
τ_0	Dwell time of open-pore state
τ_b	Dwell time of blockage state

1. Introduction

Health is an eternal topic of human being. With the extensive accumulation of knowledge, the tremendous leap of medical technology, and the huge improvement of sanitary condition, human life expectation has been significantly prolonged. In current era, continuously growing demands on higher quality of life, not only longer lifespan, and the looming aging problem of society pull and push the major innovations in medicine and healthcare from the two sides, respectively. It has been igniting the concept of precision medicine (PM) with vigorous potential. PM suggests a revolutionary medical paradigm that concerns two phases [1], [2]: 1. Refined individual diagnosis at molecular level for customized treatment; 2. Tailored medical products, such as drugs, medical instruments, artificial organs, *etc.*, to individual patients. In this paradigm, molecular biology technologies are widely desired and various kinds of biological sensors are urgently appealed [3], not only for personal diagnosis but also for medical product design. In addition, marriage between biological techniques and electronic sensors gives birth to manifold low-cost portable medical devices [4], which create feasible ways to bring our fancy concepts to daily life, such as telemedicine, Internet of Things, smart healthcare, big data based diagnosis, *etc.*

1.1. Molecular detection methods in precision medicine

Inspection of biological molecule is the technical foundation for PM, from which exhaustive personal biological information can be acquired, analyzed, archived, retrieved, and compared. Different from the traditional assays in medical diagnosis, such as blood analysis, urinalysis, biopsy, electrophysiological analysis, and medical imaging, original information about genes and their expressions, protein activity, and endocrine state are accessed by emerging technologies at molecule and cell level, such as DNA/RNA sequencing, gene probing, protein mapping, *etc.* In addition, wearable devices for long-term continuous monitoring of physiological status and in-field rapid assay equipment are other markets of PM.

Nowadays, molecular genetic test is commonly adopted in diagnosis and risk assessment of many genetic diseases, such as [5]–[7]: Angelman syndrome, Huntington’s disease, Prader-Willi syndrome, DiGeorge syndrome, cardiovascular diseases, breast cancer, *etc.* It is mainly based on hybridiza-

tion of target DNA to its complementary probes, which will further induce other detectable signals, such as fluorescent illumination and autoradiogram [7], [8]. It can ascertain various kinds of mutations in gene, including common and rare point mutations, copy number variants, uniparental disomy, balanced inversions or translocations, and repeated expansions [5], [7]. The mature technologies include short tandem repeat analysis, restriction fragment length polymorphism analysis, signal-nucleotide polymorphism analysis, fluorescent *in situ* hybridization, comparative genomic hybridization, Southern blot, and multiplex ligation-dependent probe amplification [5], [8], [9]. Furthermore, DNA sequencing technologies are applied to specified genes (panel and pathway sequences), whole-exome, even whole-genome, from which the exact sequence of DNA is obtained and scrutinized [5], [10], [11]. Therefore, abnormal mutations can be captured.

Proteins are not only important bricks to build human bodies, but also functional tiny machines to operate bodies. Thousands of proteins possessing different functions work collaboratively in cells to maintain the basic metabolism [12]. Therefore, detection of proteins, as well as assessment of their activity, is a direct way to learn the physical status of bodies and even address related diseases [13], [14], such as cystic fibrosis, nephrogenic diabetes insipidus, Alzheimer's disease, breast cancer, *etc.* The commonly used clinical technologies for protein detection are based on the bio-specific interactions, for example, antibody-antigen and enzyme-substrate [15]–[17]. The interactions are visualized by fluorescent labels, chromatic labels, nanoparticles, *etc.*, and further quantified through standard methods, such as enzyme-linked immunosorbent assay, protein immunoprecipitation, immunostaining, and immunoelectrophoresis [16], [18], [19]. Identification of the sequence of amino acids in a protein is not so easy as sequencing a DNA, and the only methods currently available are Edman degradation and mass spectrometry [12], still expecting technological breakthroughs.

Furthermore, monitoring the characteristic small chemical molecules is another important scope to follow patients' illness condition clinically, as well as people's health condition in daily life, such as glucose, hormones, metabolites, and ions [20]–[22]. The commonly used methods include electrochemical assay [23], optical label [24], electronics [25], chromatography [26], *etc.*

1.2. Nanopore based sensors

Nanopore based biomolecular sensing is a newly emerged technology in recent three decades. Inspired by the principle of cell counter [27], it is demonstrating its powerful capability and unique advantages on sensing biomolecules with an extremely high sensitivity reaching single-molecule level, which has been attracting more and more attentions from various

fields. The working principle of nanopore sensing can be explained by referring Figure 1.1. A nanoscale pore is drilled through a thin membrane. The membrane is immersed in an electrolyte and separates it to two compartments. The only connection path is the nanopore in between. An external bias voltage is added on the electrolyte across the nanopore membrane through a couple of Ag/AgCl electrodes. Consequently, an ionic current is formed through the nanopore. Furthermore, when analytes are added to one side of the nanopore, they will be driven by electric field or other effects induced by the field, and translocate through the nanopore. During their passage, the pore will be occupied to certain extent, resulting in a decreased current under general conditions. The translocation caused negative current pulses, usually named spikes, carry analyte information, such as size, charge, and concentration. Deciphering the features of the spike waveform, accompanying with their stochastic behaviors, we can dig out this information.

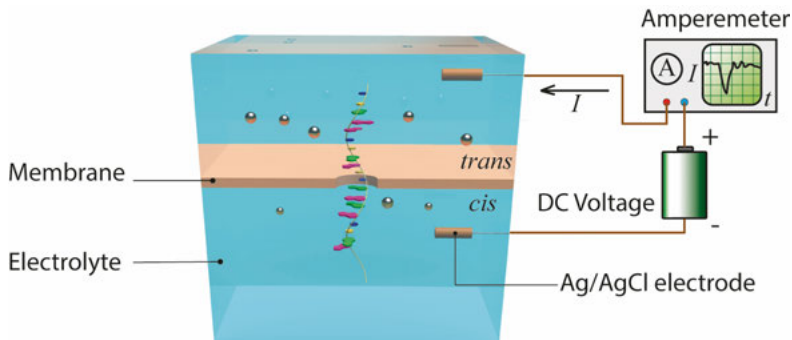


Figure 1.1. Schematics showing the structure of nanopore sensing system.

According to the material and fabrication method, nanopores can be divided into two big categories [28], namely biological nanopores and solid-state nanopores. The former are natural protein ion channels found in the cell lipid membrane, which have determinate diameters ranging from 1 nm to 4 nm [29], such as α -hemolysin (α -HL) [30], *Mycobacterium smegmatis* protein A (MspA) [31], Phi29 connector [32], Aerolysin [33], Cytolysin A [34], Outer Membrane Protein G [35], *etc.* (Figure 1.2). The latter are artificially formed pores in solid-state membranes, such as SiN_x [36], SiO_2 [37], silicon [38], graphene [39], MoS_2 [40] and polymers [41], by using focused ion beam [42], electron beam [43], electrical breakdown [44], electrochemical etching [45], and electron beam lithography followed by etching [46]. Moreover, people have tried to insert a biological nanopore into a solid-state pore [47], [48] for combining advantages inherited from both, which are named hybrid nanopores. The pros and cons of different categories will be discussed in Section 1.3 in detail.

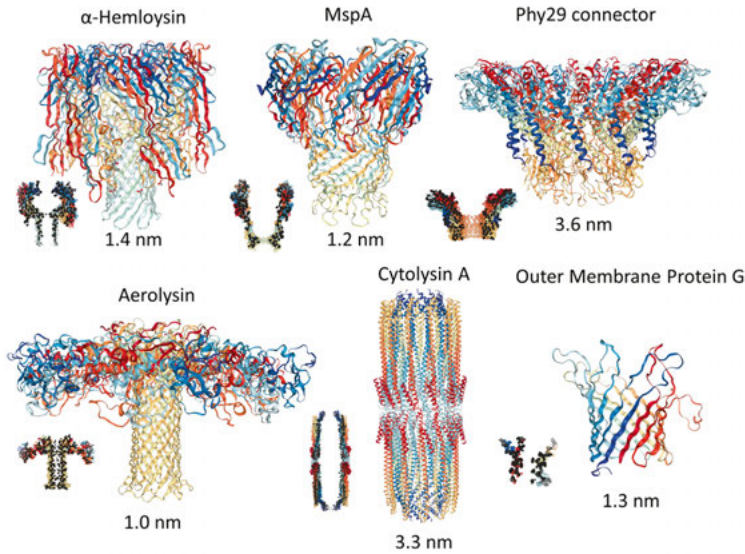


Figure 1.2. Structure of biological nanopores. The cross-section profiles are shown at the left down corner of each pore and the corresponding diameters of the narrowest part are listed below. Figures are from Protein Data Bank.

Nanopore sensors have been used in many fields, primarily brought up shouldering an aim to sequence DNA by several laboratories during the 1980s [49]. Several research groups have already achieved DNA sequencing on modified biological nanopores [50]–[53]. To enhance the signal, many subtle mechanisms have been introduced, such as directional mutation involving special chemical groups to strengthen the interaction with nucleotides [54], labelling big tags on corresponding nucleotides [55], clamping DNA by enzyme to slow down the translocation speed [52], *etc.* Hagan Baylay, *et al.* have founded Oxford Nanopore Co. in 2005 and transferred laboratory prototypes of DNA sequencer to a series of commercial products, such as MinION [56] (Figure 1.3). Nanopore sequencing leads the third-generation DNA sequencing technology owning a very long read (2 M base pairs [56]). Different from the previous technologies, the third-generation technologies pursue for single molecule detectability, avoiding polymerase chain reaction and duplication errors wherefrom, and ultra-long read, relieving huge pressure on the DNA segment splicing processes after sequencing, reducing the requisite to reading depth, and raising accuracy [10], [57]–[59]. The long-read technology realizes many possibilities, such as *de novo* assembly for accurate assemblies, targeted sequencing genomes containing stretches of highly repetitive elements, full length sequencing of isoforms, detection of structural variants, *etc.*, which are believed to be challenging or even impossible with the previous technologies [60].



Figure 1.3. MinION sequencer from Oxford Nanopore Technology Co. The figure is taken from the website of Oxford Nanopore Technology Co. [56]

Besides, nanopore sensors have shown many other successful applications on detection of nucleic acid structures [61], [62], nucleotides [63], genes [64]–[66], proteins [35], [67], [68], microRNA [69]–[71], peptides [72], chemical molecules [73], [74] and ions [75], [76]. It is really the technology that can easily capture single-molecule interactions, pushing the sensitivity to its limit. In addition, the selectivity to target analytes can be precisely introduced by anchoring corresponding probes [77]–[79], functionalizing the surface [67], and mutating certain amino acids [80], [81]. It can be also used to perceive dynamic processes, such as DNA-protein interaction [82], [83], ligand-ion/molecule interaction [75], [84], catalytic reaction, *etc.* Some beautiful examples are given here: Erik C. Yusko, *et al.* used lipid bilayer functionalized nanopores with specified anchor probes to distinguish different protein profiles [85]; Wayne Yang, *et al.* introduced CRISPR-dCas9 to specifically hybridize target sequence on DNA, which could become detectable by solid-state nanopore [86]; Nicholas Bel, *et al.* designed nanostructures on DNA strand, which could cause personalized translocation waveform in nanopipette and could be used to code different antibody-antigen interaction [87]; Ren Ren, *et al.* designed a control gate near the mouth of nanopipette, which could modulate the translocation of analytes [77].

In addition, micropores, *i.e.*, pores of diameter in micrometers, are used to detect pollens [88], bacteria [89], and particles [90], which enrich the extension of nanopore sensing. Furthermore, with the assistance of advanced data analyzing algorithms, such as waveform extraction and correction [91]–[93], deep learning [94], and wavelet analysis [95], nanopore sensing technology is becoming more powerful, robust, mature, and precise, and gradually taking its position in future PM.

Figure 1.4 shows the number of publications in the nanopore field from 1990-01 to 2019-04. The orange area represents the number of publications with the keyword “nanopores”, while the blue one focuses on “solid-state nanopores”. In the figure, the dot line displays the percentage of publications about solid-state nanopores. All the data are collected from *Web of Science* database [96]. It can be seen that the nanopore research still has a very strong growth momentum nowadays. Moreover, the work about solid-state na-

nopores appeared around 2000, and after a rapid increase for a decade, they represent a stable share after 2010.

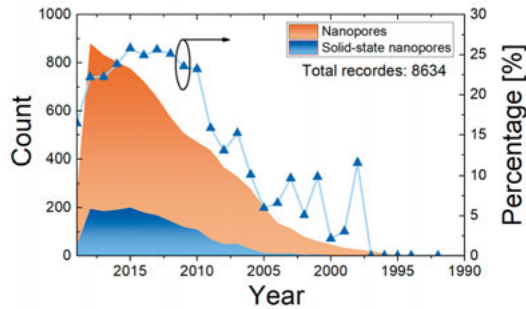


Figure 1.4. Numbers of publications about nanopores and the percentage of solid-state nanopores, during the year 1990-2019.

1.3. Solid-state nanopores vs. biological nanopores

Biological nanopores are the first group of actors on stage since 1980s. They were firstly used to detect DNA molecules. Until 2001, with the full understanding and development of ion/electron beam drilling techniques, solid-state nanopores were realized in SiN_x and SiO_2 membranes, then in graphene and MoS_2 . Different properties of these two categories can be summarized from the following aspects, listed in Table 1.1.

Table 1.1 Comparison between solid-state nanopores and biological nanopores

	Solid-state nanopore	Biological nanopore
Geometry	Variable	Determinate
Fabrication	Massive, wafer scale	Small scale (~hundreds)
Material	Multiple choices	Protein (amino acids)
Directional functionalization	Poor controllability	Atomic level precision
Material stability	Robust	Fragile
Measurement repeatability	Low	High
Background noise	High	Low

The geometry (*i.e.* size, shape, and thickness) of solid-state nanopores is engineerable to fit different application scenarios, while that of biological nanopores is fixed. Though scientists have tamed various biological pores, their diameters only cover the range from 1 to 4 nm [29], which may limit their applications. Solid-state nanopores can be fabricated on wafer scale by,

for example, electron beam lithography and etching, which is compatible with semiconductor processes and facilitates the process integration with readout electronics for high-throughput parallelized architecture [97]. Furthermore, a library of materials can be selected for different purposes. On the contrary, biological nanopores are fabricated through solution based biological techniques. These techniques are believed to be relatively weak on the controllability and hard to transfer to a largescale industry fabrication line. In general, biomaterials, such as lipid membranes, protein nanopores, and functionalized enzymes are relatively fragile compared to rigid solid-state materials, since they are usually necessary to be stored in aqueous circumstance with special care. However, biological pores naturally possess many unique merits which are lacks for solid-state ones. By the edit of the original DNA sequences of biological pores, every amino acid composing the pore is substitutable. It enables that well-designed active sites/functional groups/linkers can be implanted in a designed position with atomic precision and the local physiochemical microenvironment can be adjusted accurately. Thanks to the stable physiochemical properties in and around the biological nanopores, it is likely to give stable and repeatable experimental results. Furthermore, the natural anti-adsorption property of lipid bilayer [98] and protein surface could be a reason for a much low noise level achievable [28], [99]. For example, the noise root-mean-square (RMS) for solid-state nanopores is seldom smaller than 1 pA [99]–[102], which can be easily achieved with biological ones [103], [104]. Seizing on the advantages of solid-state nanopores and relying on the strong support of electronics knowledge and semiconductor fabrication experiences, my PhD study focuses on solid-state nanopores, which is also the protagonist of this thesis.

1.4. From sequencer to profilometer

Nanopore technology was firstly brought up pursuing for DNA sequencing during the 1980s [49]. Preliminary experiments were implemented on biological nanopores, mainly α -HL [30], [103]–[106]. With the appearance of solid-state nanopores in 2001 [49], the pursuit of DNA sequencing is extended to the solid-state ones [36], [107], [108], due to their merits such as high-robustness device, high-throughput parallelized configuration, high-density integration, and good semiconductor process compatibility. However, this leap was too big and early to be realistic. In spite of solid-state nanopores, at early 21st century scientists did not find the right way yet to achieve the DNA sequencing even on the biological ones. Until 2011 two breakthrough techniques, engineering of MspA pore and control of translocation speed by phi29 DNA polymerase, with biological nanopores are achieved leading to the success of DNA sequencing [49]. The problems were obvious and severe for solid-state nanopores: poor spatial resolution and

high background noise, which worsen the signal to noise ratio (SNR) from both signal and noise sides. Therefore, seeking stronger signals with higher spatial resolution is hoped for nanopores of smaller size in a thinner membrane. Nanopores of sub-5 nm diameter, comparable with the geometry of biological nanopores, were drilled in SiN_x membrane successfully [42]. In addition, two-dimensional (2D) materials, such as graphene and MoS₂, were used as the membrane for their extreme small thickness [109]. Unfortunately, these efforts did not really help much. High translocation speed, strong conglutination of DNA on the membrane, mechanical instability, complicated surface physicochemical conditions, and even higher noise level of nanopores in the 2D materials are all vital factors [110]–[112] ruining major benefits from the pore shrinkage and thinning. Turning eyes back on the success of biological nanopores on DNA sequencing, it seems that their key strategies are difficult to be transplanted to the solid-state system. As discussed in last section, many key techniques in biological pores are difficult to implement on solid-state ones, though some trials were reported [85], [113]–[116]. These issues include introducing special functional groups precisely at certain position in nanopore, anchoring enzyme to grab target DNA and slow down its translocation speed, and functionalizing suitable molecules on the nanopore surface to stabilize its physicochemical properties.

Therefore, the merits of solid-state nanopores and their applications were reconsidered and the old question was asked again: what is the suitable target for solid-state nanopore sensing? Flexible selection of nanopore material, tailorable size and shape, massive production and compatible with semiconductor processes are all the sparkle superiorities of solid-state nanopores. Temperately putting down the obsession of DNA sequencing, a wider picture is expanded at horizon. Protein profiling is a typical one of the promising stories [85], [117], [118]. Adequately benefiting from the advantages of solid-state nanopores, many interesting and important detections can be developed, such as, DNA-protein complex [82], [119], microRNA-protein complex [70], aptamer-lysozyme interaction [120], biotin-avidin interaction [121], antibody-antigen interaction [77], [78], enzyme ubiquitination [122], special structured RNA [62], DNA methylation [123]. Besides, the platform has been even extended to matrix paralyzed devices [124], [125].

1.5 Challenges in large-scale real-life applications

Although solid-state nanopores hold promises for so many tempting future applications and shown their powerful capability in sensing various kinds of analytes, there are still many unavoidable problems impeding their commercialization for real-life applications. Poor repeatability is one of the crucial problems. The same nanopore may give totally different background noise levels and translocation behaviors for the same analytes at different times of

measurement, even under the same measurement conditions. This is attributed to the nonrepeatable physicochemical microenvironment in and around the pore, including surface charge density, wettability, chemical groups, adsorption of contaminants, *etc.* [126], [127], [111], which are extremely difficult to be well controlled in every measurement. Even though a very carefully cleaning process has been done prior to the measurement, such as long-term oxygen plasma treatment and piranha soaking, high repeatability of the translocation outcome cannot be guaranteed [128], [129].

Another crucial problem is instability during measurement. It is related to the sticky surface of solid-state materials, especially graphene [111], [127] which renders adsorption of hydrated ions, analyte molecules, and other contaminants, even clogging of nanopores. It can cause fluctuation/drift of the background current, appearance of sudden step-like changes of current, and even total blockage of nanopores. Consequently, the translocation process is influenced to deviate from the assumption of a stationary stochastic process.

Furthermore, relatively high noise level of solid-state nanopores is a problem worthy attention [101], [130]–[133]. To achieve a higher time and spatial resolution, the ability of distinguishing weak signals from the background noise is necessary. Therefore, a low noise nanopore is a prerequisite for high quality sensing.

Based on the above considerations, understanding translocation process and the physical mechanisms behind is necessary and urgent. Only by tracing back to the origins of the problems, can we have a chance to resolve them.

1.6. Scope of this thesis

This thesis aims at a comprehensive investigation of mechanisms in solid-state nanopore sensing, and, especially, understanding the electrical properties of open-pore state, translocation process and signal generation, as well as background noise origins. In this way, a fundamental theoretical frame is to be established, where further insights, models, refinements, and corrections can be structurally replenished, as bricks, in the right places. Furthermore, a standardized experimental platform is to be constructed. In detail, the right way to prepare samples, acquire data, process data, and analyze results needs developing under the guidance of theories. In addition, novel methodologies of sensing are to be explored by novel device structures and measurement configurations. The structure of this thesis can be summarized as Figure 1.5 and the detailed organization is as follow:

Chapter 2 constructs the backbone theory for solid-state nanopore sensing. Staring from a generalized resistance model for arbitrary shapes of nanopores at open-pore state (**Paper I**), the core concept, effective transport

length, determining the electric properties of nanopores is strictly defined. Focusing on the electric field distribution, the electric property of a novel structure, zero-depth interfacial nanopore, is analyzed (**Paper II**). Seizing the high-electric-field region in nanopores, the causal chain of ionic current rectification of asymmetrical nanopores are found, and an analytical model is established (**Paper III**). Then, the origins of noise in solid-state nanopores are identified and a comprehensive model is presented (**Paper IV**). Finally, in the perspective of system level, the signal and noise properties of nanopore DNA sequencing are analyzed, which confine the signal margin under certain noise level. The analysis indicates the direction of improving SNR (**Paper V**).

Chapter 3 focuses on the experimental implementation of nanopore based sensing. First, the measurement protocol is standardized and the principles in data acquisition are discussed in particular. Second, the translocation data processing is demonstrated by DNA translocating SiN_x nanopores. Third, protein translocations in truncated-pyramid nanopores (TPP) are carefully studied. The electroosmotic vortex is formed in such a structure, which strongly influences the translocation behavior of protein with the size comparable to the nanopore (**Paper VI**). Forth, the electrolyte concentration gradient across a nanopore can generate power, which is strong enough to drive the translocation of proteins and λ -DNA. This autogenic translocation nature of nanopores can facilitate simplification of readout circuit design, increase of integration density, and improvement of amplification performance (**Paper VII**). Last, the group translocation behavior of nanoparticles in multiple nanopores is studied. The output current from an array of nanopores is the superposition of current from each pore in the array. It carries information about the analytes and can be deciphered by analyzing features in the ionic current (**Paper VIII**).

This thesis is concluded with Chapter 4 where a general summary and a future outlook are outlined.

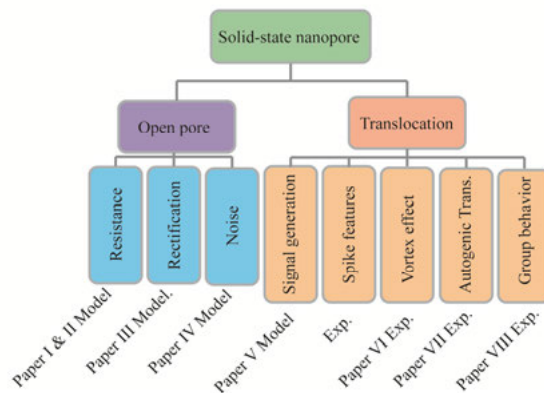


Figure 1.5. Structure of this thesis and organization of related materials.

2. Understanding of solid-state nanopore sensors

Nanopore sensors gradually show their intoxicating charm contained in their succinct structure and single molecule distinguishability. However, the physical processes and mechanisms involved in are not as simple as it seems to be. The coarse outline of nanopores is just a resistor, described by Ohm's law, with a regulatable resistance by translocating analytes. As summarized in Figure 2.1, many complicated physical processes play crucial roles to modulate the apparent electrical properties and to shape the analyte translocation behaviors. These processes include surface charge dynamics in electrical double layer (EDL) [134], ion transport in electric field [135] and concentration gradient [136], hydrodynamics of electroosmotic flow [137], [138], hydrated ion friction with pore wall [139], [140], diffusion and capture of analytes [141], kinetics of analyte deformation and interaction with pore surface [112], [142], [143], competition between electrophoresis force and hydro-viscous force on analyte [144], steric occupation of analyte in the pore and electric field redistribution [145], *etc.* Constricted physical factors, such as electric field, fluidics, and ion flux, in nanoscale space is the origin of the single molecular sensitivity and the unavoidable complexity as well, which offers chances, although challengeable, for sensing in different perspectives. Therefore, understanding of mechanisms involved in nanopore sensing is a foundation for further applications. Let's initiate this fascinating journey from the very beginning and simple case, resistance of open-pore state, and reveal its mystery and beauty step by step.

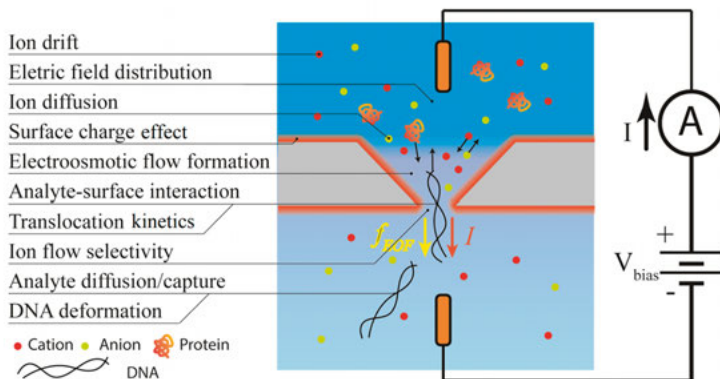


Figure 2.1. Physical processes involved in a nanopore sensing system.

2.1. Physics of nanopore conductance

Conductance is a basic electrical parameter for nanopore sensors, which is determined by the electric field distribution in the pore structure. With a simple assumption of an uniform electrical conductivity, the conductance, G , of a cylinder nanopore has a clear relationship with its geometry [146].

$$G = \left(\frac{4\rho h}{\pi d_p^2} + \frac{\rho}{d_p} \right)^{-1} \quad (2-1)$$

where, d_p and h are the diameter and thickness of nanopore, respectively. ρ is the resistivity of the electrolyte. The first term in the parentheses represents the resistance generated by the cylinder volume of the pore [147], while the second term describes the resistance from the two access regions at the mouth of nanopore caused by the crowd of ions from the spacious reservoir region flowing toward a constrained pore region [148].

Instead of tedious and costly high-resolution electron microscopy technology, the size of nanopore can be derived from the simple conductance measurement assisted by conductance models. The aforementioned model works well in many cylinder nanopores. However, for other shapes obtained by commonly used fabrication technologies, such as cone shape [149], hour-glass shape [150], truncated pyramid shape [151], triangular prisms shape [152], *etc.*, such an algebraic expression cannot be found even invoking the complex mathematic descriptions of the geometries and other mathematical tricks, for example, a hyperbolic function for hourglass shaped nanopores [147], correction parameters for triangular shaped nanopores [152], and integral equation for irregular geometrical profiles of nanopores [153]. The case by case study entangling with sophisticated mathematical tools is not an efficient way to solve the nanopore conductance problem. A general method is needed to bridge between the conductance and the geometry for any shape of nanopores. An entirely new perception, therefore, should be sought from the physical essence of the resistance.

2.1.1. Electric field distribution in a nanopore

The nanoscale space of nanopores constrains the electric field in and the ion drift fluxes driven by the field. The constraint is the origin of resistance. In other words, the constrained region bears the highest electric field in the system (Figure 2.2 (b)) and the major voltage drop, according to Gauss's law. By referring to a typical cylinder nanopore illustrated in Figure 2.2 (a), our model takes on the well-known relationship for object conductance in basic physics:

$$G = \frac{S_0}{\rho L_{eff}} \quad (2-2)$$

where S_0 is the minimum cross-section area and L_{eff} is the length of the resistor extending from the nanopore to the two sides into the electrolyte, named effective transport length. Moreover, as shown in Figure 2.2 (c), the electric field intensity decays approximately in an exponential manner away from the center of nanopore where it reaches the maximum. Therefore, L_{eff} is defined to be equal to the sum of the distances from the center of the nanopore where the electric field is at its maximum intensity to the two points along the nanopore axis where the electric field falls to e^{-1} of this maximum at both upward and downward directions, and it measures the length of high-electric-field region.

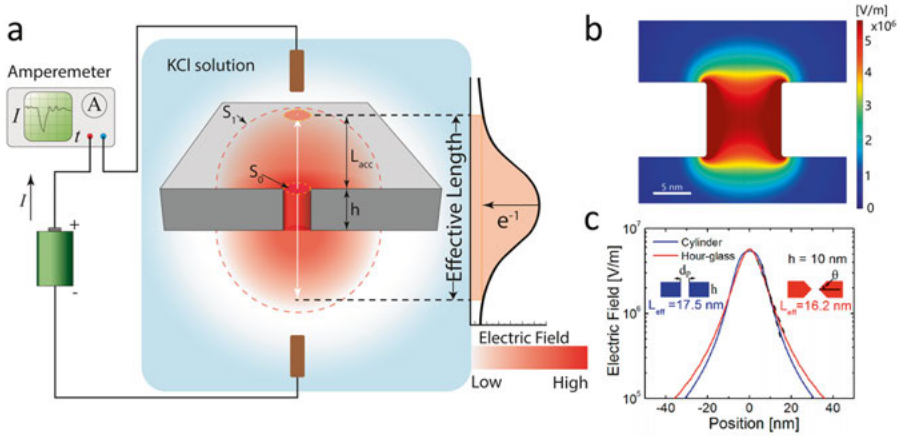


Figure 2.2. Conductance model based on the concept of effective transport length. (a) Schematic showing the distribution of electric field in a cylinder nanopore. The equi-field surfaces S_1 and S_0 are circled by dash lines, from which the concept of effective transport length is built. (b) Simulation results of the electric field distribution in a nanopore with a 1 M KCl solution at a 100 mV voltage bias, with the field peaking in the middle of the cylinder pore and decaying outward along the nanopore axis. Nanopore diameter $d_p = 10 \text{ nm}$, membrane thickness $h = 10 \text{ nm}$. (c) Distribution of electric field along the nanopore axis for two different nanopores, cylinder (blue) and hour-glass (red), with the zero point being set at the pore center and dash lines representing ideal exponential functions. Cylinder nanopore: $d_p = 10 \text{ nm}$ and $h = 10 \text{ nm}$; hour-glass nanopore: $d_p = 10 \text{ nm}$, $h = 10 \text{ nm}$, and half-wedge angle $\theta = 60^\circ$.

2.1.2. Effective transport length and conductance model

In next step, the relationship between L_{eff} and the nanopore geometry is to be found, so that an analytical expression of conductance linking to the geometry can be derived. According to Ohm's law, the density of ionic current is linearly proportional to the intensity of electric field. Therefore, they share the same distribution pattern. As no source exists along the path of the ionic

current, the total current passing through any equi-field surface (e.g. S_1) is equal to that through S_0 . In other words, on the specific equi-field surface S_1 where $S_1=e \times S_0$ holds, the current density and the electric field on S_1 are both e^{-1} of their counterparts on S_0 . Hence, L_{eff} is twice the distance from the pore center to S_1 for a symmetrical system. The electrical problem is then now converted to a geometrical problem that can be readily solved analytically.

For a cylinder pore, the area of the equi-field surface S_1 can be estimated as a hemisphere of diameter L_{acc} with a projected pore area embedded in.

$$\frac{S_1}{S_0} = \frac{2\pi L_{\text{acc}}^2 + S_0}{S_0} = e \quad (2-3)$$

$$S_0 = \frac{1}{4}\pi d_p^2 \quad (2-4)$$

with the solution $L_{\text{acc}}=0.46d_p$. Therefore,

$$L_{\text{eff}} = h + 2L_{\text{acc}} = h + 0.92d_p \quad (2-5)$$

Following a similar method, L_{eff} of other shapes of nanopores can be expressed by geometry parameters algebraically. For example, an hourglass shape can be approximated by two head-to-head identical truncated cones. The equi-field surface can be regarded as a hemisphere intercepted by the sloped sidewall of the cones, if it locates in the pore (*i.e.* $L_{\text{eff}} < h$). Otherwise, it is just a complete hemisphere as that in the cylinder nanopore case for $L_{\text{eff}} > h$. A linear relationship between L_{eff} and the critical length x (d_p for circle cross-section pores and side length a for square and triangle cross-section pores) is founded for different shapes of nanopores holding the form of:

$$L_{\text{eff}} = b + kx \quad (2-6)$$

And the detailed expressions of the factors b and k are listed in Table 2.1 for various pore shapes.




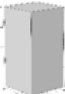



Substitute Eq. 2-6 into Eq. 2-2, the solution to d_p can be obtained for circular pores.

$$d_p = \frac{1.94G\rho + \sqrt{3.39G^2\rho^2 + 4\pi hG\rho}}{\pi}, \text{ for cylinder pores} \quad (2-7)$$

$$d_p = \frac{3.68G\rho}{\pi\sqrt{1-\sin\theta}}, \text{ for hourglass pores with } L_{\text{eff}} \leq h \quad (2-8a)$$

$$d_p = \frac{1.84G\rho + \sqrt{3.39G^2\rho^2 + 4\pi hG\rho(1-\sqrt{1-\sin\theta})}}{\pi}, \text{ for hourglass pores with } L_{\text{eff}} \geq h. \quad (2-8b)$$

Table 2.1 Parameters b and k in Eq. 2-6 for various shapes of nanopores

Shape	Schematics		k	b
Cylinder			0.92	h
Hourglass		$h > L_{\text{eff}}$	$0.92 / \sqrt{1 - \sin \theta}$	0
		$h < L_{\text{eff}}$	0.92	$h(1 - \sqrt{1 - \sin \theta})$
Truncated-cone		$h > L_{\text{eff}}$	$0.46(1 + 1 / \sqrt{1 - \sin \theta})$	0
		$h < L_{\text{eff}}$	0.92	$h(1 - \sqrt{1 - \sin \theta})$
Square column			1.05	h
Square hourglass		$h > L_{\text{eff}}$	$1.05 / \sqrt{1 - \sin \theta}$	0
		$h < L_{\text{eff}}$	1.05	$h(1 - \sqrt{1 - \sin \theta})$
Truncated-pyramid		$h > L_{\text{eff}}$	$0.525(1 + 1 / \sqrt{1 - \sin \theta})$	0
		$h < L_{\text{eff}}$	1.05	$h(1 - \sqrt{1 - \sin \theta})$
Triangular prism			0.688	h
$L_{\text{eff}} = kx + b$ ($x = d_p$ for circular pores; $x = a$ for square pores)				

The formulas for square pores can be derived in the same way. L_{eff} of different shapes of the nanopores in $h=20$ nm-thick membrane is compared in Figure 2.3. It shows that L_{eff} of different shapes of nanopores has different growth rates with the increase of the critical length. The column nanopores, such as cylinder, square-column, and triangular prism, always contain a membrane thickness h in L_{eff} , so their L_{eff} approaches the limit of h at the extreme with the critical length. Truncated cones own the shortest L_{eff} at small d_p and is defeated by triangular prisms when the critical length is larger than 30 nm. Moreover, square columns have the longest L_{eff} among the aforementioned shapes in the whole range of the critical length.

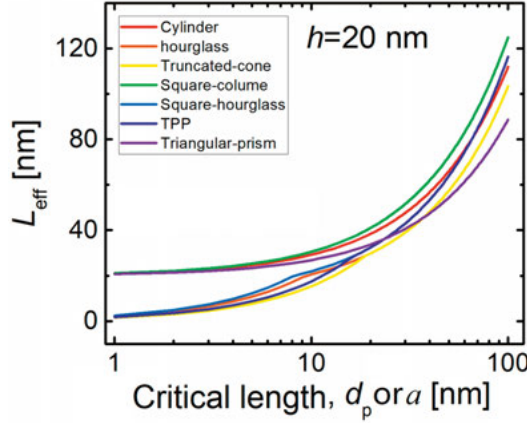


Figure 2.3 Effective transport length of nanopores of various shapes in a 20 nm thick membrane.

In order to verify our model, we compared both simulation and experimental results with corresponding conductance calculated by our model of cylinder and hourglass nanopores with different diameters and membrane thicknesses, as shown in Figure 2.4. The model coincides with the simulation and experimental results perfectly, which indicates that it has captured the essence of the physical picture of nanopore resistance, *i.e.*, electric field distribution, and is a powerful tool to extract the size of nanopore from a simple conductance measurement.

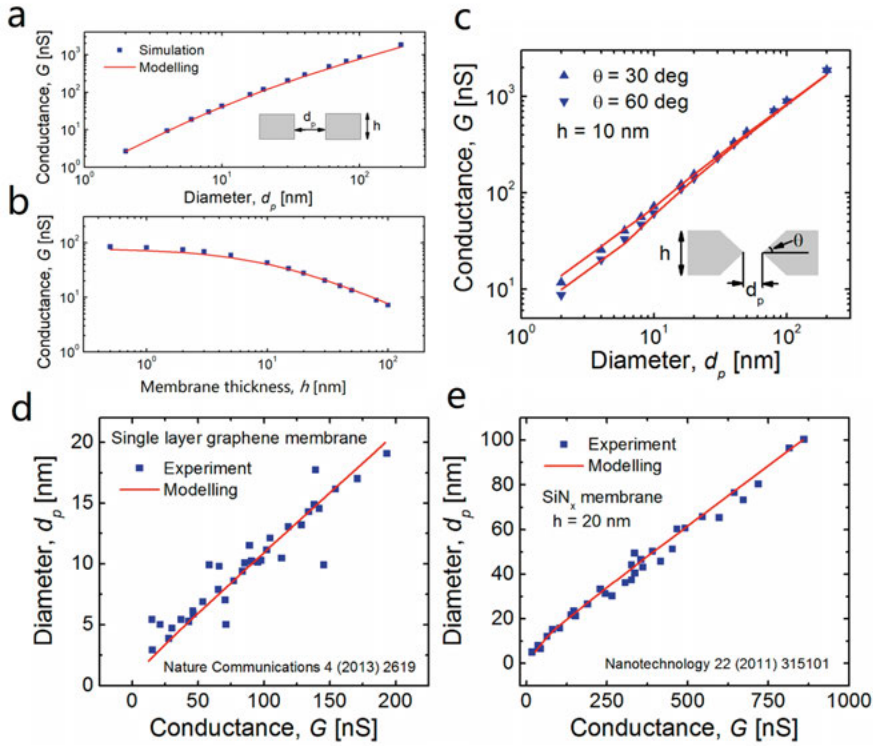


Figure 2.4. Model validation by comparison with numerical simulation and experimental data. (a, b) Variation of G with d_p and h for cylinder nanopores respectively, showing an excellent agreement between modeling (red lines) and simulation (blue symbols). h is fixed to 10 nm in (a) and d_p is fixed to 10 nm in (b). (c) Variation of G with d_p for two different hourglass nanopores with $\theta=30^\circ$ (triangles), and 60° (up-side-down triangles) and $h=10$ nm, again showing an excellent agreement between modeling (red lines) and simulation (blue symbols). Electrolyte: 1 M KCl solution, voltage bias: 100 mV for all cases. Nanopore diameters extracted from their conductance measurement results by applying our model (red line), in comparison with original experimental data (blue symbols) for (d) nanopores in atomic-thick single-layer graphene and (e) nanopores in SiN_x thin-film membrane of 20 nm thickness, both measured in a 1 M KCl solution. Adapted with permission from [154]. Copyright (2018) American Chemical Society.

During the derivation of the model, a homogeneous conductivity is an assumption, which means the influence of surface charges on the pore wall is not included. Therefore, it is worth estimating the error caused by the surface charge. Comparing COMSOL simulated conductance with that predicted by our model, Figure 2.5 shows the variation of relative error in G with the surface charge density for cylinder pores of different diameters. The relative

error is defined as the relative difference in G between the model predicted value and the simulated one, referring to the simulation results. As expected, the relative error of G is higher for a smaller pore with a higher density of surface charge, since in this situation, surface conductance can dominate. Nevertheless, the largest relative error in G is below 10% even for the smallest nanopore of $d_p=2$ nm with the highest charge density at 0.06 C/m^2 . This charge density is reasonable for SiN_x and SiO_2 nanopores in pH-neutral solutions [155]–[157]. The correction of the model by considering the surface conductance can be found in Section 2.1.4.

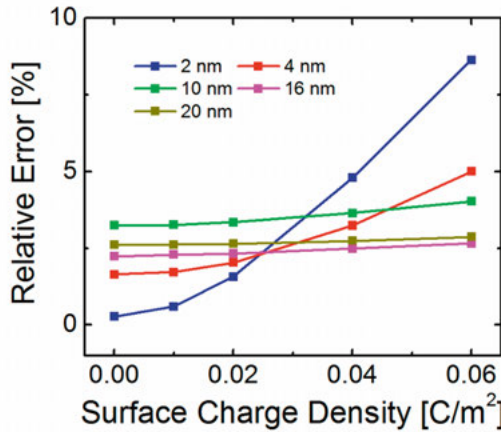


Figure 2.5. Variation of relative error in G with surface charge density for nanopores of 2, 4 10, 16, and 20 nm diameter all with $h=10$ nm. Adapted with permission from [154]. Copyright (2018) American Chemical Society.

2.1.3. Effective transport length of zero-depth interfacial nanopores

A novel structure of nanopore is proposed to achieve L_{eff} as small as possible pursuing a better spatial resolution of the analyte profile reflected in block-age current fluctuations (see more discussion in Section 2.4). As shown in Figure 2.6 (a), two nano-trenches in thin slabs are superimposed with a crossing configuration to form a shared interface with mathematically zero thickness. This structure is fabricated by dissolving two superimposed and crossing metallic nanorods, molded in polymeric slabs. The width of the two trenches, thickness of the slabs, and the angle of the crossed trenches influence the resistance of the interfacial nanopore. As shown in Figure 2.6 (b), since the geometry of the high electric field region of the conventional square-column pore and the interfacial pore is significantly different, L_{eff} gives a totally different dependence on the side length of nanopore, illustrated in Figure 2.6 (c, d). L_{eff} of the interfacial nanopore increases and then levels off with the increase of slab thickness h . In addition, the saturated

level is determined by the trench width a . The smaller a , the shorter L_{eff} . Furthermore, compared with the conventional square column nanopores with the membrane thickness of $2h$, as shown in Figure 2.6 (c), zero-depth interfacial nanopores possess a much smaller L_{eff} , and the advantage is more significant for the pores with larger h .

Zero-depth interfacial nanopores avoid the contribution of membrane thickness (pore region) to the effective transport length (*c.f.* Figure 2.6 (b)), which largely confines the electric field in a range as small as possible benefiting the spatial resolution for sensing.

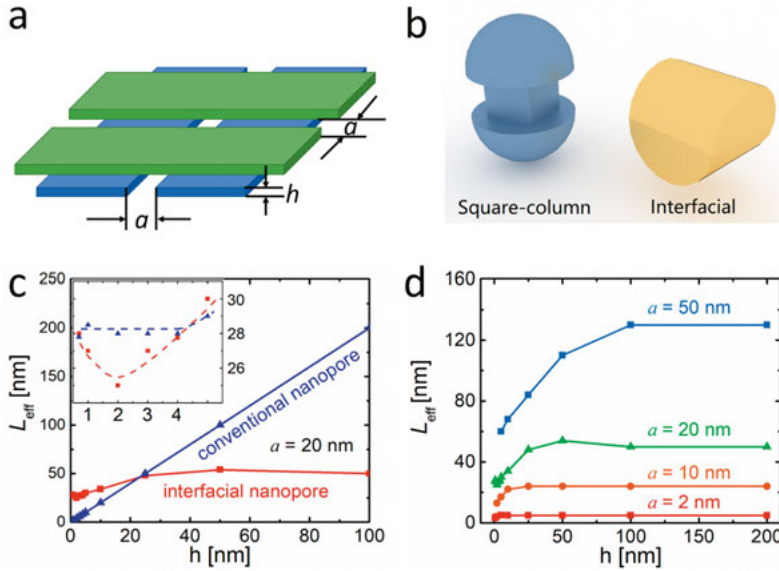


Figure 2.6. Electrical characteristics of the zero-depth interfacial nanopore. (a) Schematic showing the structure of the zero-depth interfacial nanopore. (b) The geometry of the high electric field region in the conventional square-column nanopore and the interfacial nanopore. (c) Comparison of the simulated L_{eff} of the interfacial and conventional nanopores for different thicknesses: The membrane thickness of the conventional nanopore is $2h$ to be comparable with the interfacial nanopore formed by superimposing two trenches in slabs with the thickness of h each. Both nanopores are of squared shape openings of $20 \text{ nm} \times 20 \text{ nm}$. The inset focuses on a small window for very small h . The vertical and horizontal axis of the inset figure have the same unit as the main panel. (d) Evolution of L_{eff} of interfacial nanopores for different h and a .

2.1.4. Surface charge extraction from conductance measurement

In previous sections, a uniform conductivity of electrolyte in the nanopore system is assumed. However, a layer of surface charge accompanying with

EDL is difficult to be avoided in reality. Therefore, the contribution of surface charge to nanopore conductance should be considered. According to the literature, the conductance of nanopore is contributed by bulk conductance G_b and surface conductance G_s simultaneously [158], [159].

$$G = G_b + G_s \quad (2-9)$$

The bulk conductance expressions of various shaped nanopores are given in Section 2.1.2. The conductance from the surface is determined by the surface charge density, σ , and corresponding ion mobility, μ . For column nanopores, the expression is simple[159]:

$$G_s = \mu\sigma \frac{\pi d_p}{h} \text{ (cylinder pore)} \quad (2-10a)$$

$$G_s = \mu\sigma \frac{4a}{h} \text{ (square-column pore)} \quad (2-10b)$$

Truncated pyramid pores have an uneven cross-section area, so L_{eff} is used instead of h in Eq. 2-10b in the case $h > L_{eff}$. The same expression is kept for the $h < L_{eff}$ case.

$$G_s = \mu\sigma \frac{4a}{L_{eff}} (h > L_{eff}) \quad (2-11a)$$

$$G_s = \mu\sigma \frac{4a}{h} (h < L_{eff}) \quad (2-11b)$$

By fitting the conductance G of a nanopore in electrolytes with different conductivity $1/\rho$ based on the aforementioned model, the critical length of the nanopore (*i.e.* the diameter d_p or side length a) and σ can be extracted. As shown in Figure 2.7, the G vs. $1/\rho$ curves of SiO₂ TPPs are fitted by the model and the surface charge density is extracted to be -0.008 C/m², -0.014 C/m², and -0.028 C/m² at the pH of 4, 7.5, and 10, respectively. Since the point of zero charge (PZC) of SiO₂ surface is around 3 [160], the higher pH the higher the charge density, which agrees with the expectation.

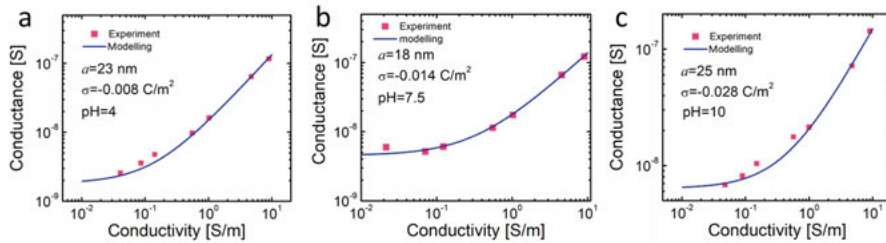


Figure 2.7. Conductance G vs. conductivity $1/\rho$ relationship for SiO₂ TPPs at (a) pH=4, (b) pH=7.5, and (c) pH=10. Dots: experimental results; Curves: model fitting.

2.2. Mechanism of rectification in nanopore ionic current

Ionic current rectification is a common phenomenon in nanopores with asymmetry in geometry and/or surface charge [161]–[163]. A large amount of studies have been done both experimentally and theoretically and researchers have tried to find the detailed mechanism of the rectification from its dependences on many factors, such as geometry of nanopore [164], [165], surface charge density [149] and polarity [166], charge distribution [167], electrolyte concentration [168] and gradient across the pore [169], pH of the electrolyte [170], *etc.* However, the understanding of physical process of rectification is still incomplete, even though numerical solutions based on Poisson-Nernst-Planck equations is widely adopted and the distributions of many physical quantities are well observed [171]–[174], such as ion concentration, electric field, potential, charge, and ion flux. Now, we will establish an analytical model to describe the ionic current rectification characteristics of nanopores by tracing the causal chain composed of related factors: surface charge on the pore wall, selectivity of ion flux through the pore, concentration redistribution around the pore, electric field adjustment in the pore, and the apparent ionic current.

2.2.1. Steady state at a given bias voltage

The origin of rectification is surface charge on the pore wall, which attracts and accumulates counterions to form an EDL. If the surface is negatively charged, cations will accumulate in the diffuse layer. This is the most commonly appeared scenario of nanopores in SiO₂, SiN_x, glass, polyimide, and poly (ethylene terephthalate) membranes. Therefore, in the nanopore, the larger population of cations than that of anions generates a preference in cation flux through the pore. In other words, the ionic current is contributed by cations more than anions, giving rise to the ion flux selectivity. Furthermore, the selectivity can be described by the transfer number of cations t_+ [175], measuring the fraction of total current carried by cations (equal to 0.5 for non-selective case and 1 for the ideal selective case). According to the Donnan equilibrium, t_+ can be expressed as [176]:

$$t_+ = \frac{\chi + 1}{\chi + 2} \quad (2-12)$$

with

$$\chi = \frac{2\sigma}{qN_A d_p c_0} \sqrt{1 - \left(\frac{\sigma}{qN_A d_p c_0}\right)^2} \quad (2-13)$$

where, q is the elementary charge, N_A the Avogadro constant, and c_0 the electrolyte concentration in the bulk region.

As illustrated in Figure 2.8 (a), for a negatively charged cone nanopore at a positive bias (the larger opening (LO) side has positive potential and the small opening (SO) side is grounded), the drift flux of cations, f_{el_c} , driven by the electric field downward is stronger than the anion drift flux, f_{el_a} , upward through the pore. However, the drift cation and anion fluxes in the region far away from the pore (region III) keep a ratio of their diffusion coefficients, *i.e.*, $\zeta=D_a/D_c$, or mobility according to the Einstein relation ($\zeta=\mu_a/\mu_c$), which confines a boundary condition for the ion fluxes at region I and II. Because of the continuity of the ion flux, the only way to compensate for the unbalanced cation and anion fluxes caused by the ion selective pore is to build a concentration gradient across the pore. Therefore, referring to c_0 , a relatively high concentration (c_H) region II and a low concentration (c_L) region I are established under a positive bias, which will induce upward diffusive fluxes for both cations and anions (f_{diff_c} and f_{diff_a}) resulting in suppression of f_{el_c} and enhancement of f_{el_a} , aligning to the boundary condition. Conversely, a negative bias will cause c_L in region II and c_H in region I. At steady state, the different fluxes in the nanopore region are related through:

$$f_{el_c} - f_{diff_c} = \zeta (f_{el_a} + f_{diff_a}) \quad (2-14)$$

According to the definition of t_+ , we have:

$$f_{el_c} = t_+ (f_{el_c} + f_{el_a}) \quad (2-15)$$

It is reasonable to assume that the built-in concentration difference $\Delta c=c_{H_p}-c_{L_v}$ between region I and II linearly spreads across the membrane thickness, h , with c_{H_p} to denote the peak value in the c_H region and c_{L_v} to denote the valley value in the c_L region. This assumption is justified by noting that at different bias polarities, the variation in Δc is the predominant factor responsible for determining the various fluxes, while the distance between c_{H_p} and c_{L_v} does not vary much, according to our numerical simulation. Thus, according to Fick's first law, the diffusive flux across the nanopore can be written as:

$$f_{diff_c} = -D_c \frac{\Delta c}{h} \quad (2-16)$$

Substitute Eq. 2-14 and 2-15 into Eq. 2-16 with relationship $f_{diff_c}=\zeta f_{diff_a}$ by the definition of ζ .

$$D_c \frac{\Delta c}{h} = \left(\frac{1+\zeta}{2} - \frac{\zeta}{2t_+} \right) f_{el_c} \quad (2-17)$$

Thus, the total current I is the integration of ion fluxes on the cross-section area of nanopore S_0 , and can be written by the following analytical form with an assumption of evenly distributed fluxes on the area.

$$I = qN_A S_0 (f_{el_c} + f_{el_a}) = \frac{2qN_A S_0 D_c}{t_+ + \zeta t_+ - \zeta} \frac{\Delta c}{h} \quad (2-18)$$

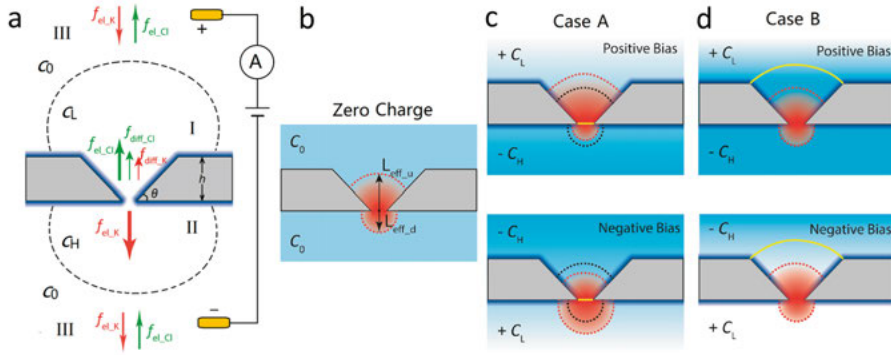


Figure 2.8. Schematics of the fundamental processes pertaining to the ionic current rectification in nanopores. (a) Ion fluxes and the built-up of concentration enrichment-depletion in a positively biased nanopore with negative surface charge. (b) L_{eff} measuring the length of high electric field region marked in red in a nanopore with zero surface charge as a reference is the sum of the upper part, $L_{eff,u}$, and lower part, $L_{eff,l}$. (c, d) L_{eff} in a nanopore with negative surface charge at positive and negative biases for case A and B, respectively. In case A, the border between region I and region II lies inside the nanopore. The black dash line marks where L_{eff} ends without surface charge as in (b), while the red dash line marks the actual L_{eff} . In case B, this border is significantly distanced from the high electric field region (marked as the light green line in corresponding figures) and lies far above the nanopore thickness.

2.2.2. Dependence of effective transport length on bias polarity

Only a surface charge caused concentration gradient is not enough to generate the current rectification, for example in a cylinder nanopore. Thus, an asymmetry in geometry is necessary for rectification if the surface is uniformly charged. As shown in Figure 2.9, the apparent total resistance of a nanopore is the sum of the resistance generated in the c_H and c_L regions near the pore (shown as the orange and blue colors), denoted as R_{CH} and R_{CL} , respectively. The subscripts, p and n , represent positive and negative biases condition, respectively. The same nomenclature is uniformly followed by other variables in this section. Two factors, resistivity and geometry, determine the resistance of certain region, and the former is prepotential to the electrolyte concentration. Both the geometry and ion concentration of the c_H and c_L regions at positive bias are different from those at the opposite bias polarity (*i.e.* $R_{CL,p} \neq R_{CL,n}$, $R_{CH,p} \neq R_{CH,n}$), resulting in different current levels. It is worth noting that the proportion of R_{CH} and R_{CL} is largely influenced by the nanopore geometry, which directly leads two extreme cases to be discussed later.

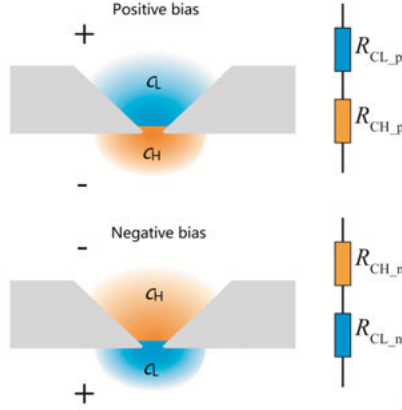


Figure 2.9. Schematics showing the resistance in the c_H and c_L regions at positive and negative biases in a geometrically asymmetrical nanopore.

Next, the connection between the geometry and current at different bias polarities should be addressed, which can be assisted by the well-established conductance model in Section 2.1. In order to calculate the nanopore conductance, L_{eff} should be carefully considered. We use a truncated-cone nanopore as a typical example shown in Figure 2.8, which can be easily extended to the majority of commonly fabricated asymmetrical nanopores, including truncated-pyramid [46], [177], hourglass [178], and nanopipette [77].

If the nanopore has a steep sidewall with a large θ referring to Figure 2.8 (a), such as a nanopipette, its L_{eff} is large and the border between region I and II is likely to fall inside L_{eff} , situated close to the smallest constriction of pore. Consequently, the contribution from both R_{CL} and R_{CH} to the total resistance is significant. The part of L_{eff} with c_H (c_L) in region II (I) will be shrunk (expanded) compared to the uniform concentration situation (Figure 2.8 (b)). This case is depicted in Figure 2.8 (c) and it is referred to as case A. On the contrary, if the nanopore has a small θ , L_{eff} becomes small and it is likely to fall entirely inside the ion enriched or depleted region. In other words, the border between region I and II is now located far from the smallest constriction of the nanopore and spans the entire L_{eff} , as shown in Figure 2.8 (d). Hence, R_{CH_p} dominates at positive bias (R_{CL_p} can be ignored), and R_{CL_n} dominates at negative bias (R_{CH_n} can be ignored). This case is denoted case B.

In case A, the amount of shrinkage and expansion in L_{eff} , in comparison to that under the uniform concentration condition, can be correlated to the corresponding Δc relative to c_0 . Thus, the final effective transport length can be expressed as:

$$L_{\text{eff}_n} = \frac{L_{\text{eff}_l}}{1 - \delta} + \frac{L_{\text{eff}_u}}{1 + \delta} \quad (2-19a)$$

$$L_{\text{eff}-p} = \frac{L_{\text{eff}-l}}{1+\delta} + \frac{L_{\text{eff}-u}}{1-\delta} \quad (2-19b)$$

with $\delta = \Delta c / 2c_0$, where, $L_{\text{eff}-l}$ and $L_{\text{eff}-u}$ are the effective transport length of the lower and upper part of the nanopore divided at the smallest constriction position. The expressions of L_{eff} as functions of geometrical parameters for various shapes of nanopore have been extensively discussed in Section 2.1 (see Table 2.1), and will not be repeated here.

In this way, the resistance R , as well as the ionic current I at bias voltage U , of nanopore is:

$$I_{p/n} = \frac{U}{R_{p/n}} = \frac{US_0}{\rho L_{\text{eff}-p/n}} \quad (2-20)$$

Combining Eq. 2-18 and 2-20, Δc can be solved as:

$$\Delta c_{p/n} = \frac{-\alpha\gamma + \sqrt{\alpha^2\gamma^2 + 16\beta c_0^2(\alpha\varepsilon_{p/n} + \beta)}}{2\alpha\varepsilon_{p/n} + 2\beta} \quad (2-21)$$

with, $\alpha = \frac{2qN_A D}{h(t_+ + \zeta t_+ - \zeta)}$, $\beta = \frac{U}{2c_0 \rho}$, $\gamma = 2c_0(L_{\text{eff}-l} + L_{\text{eff}-u})$, $\varepsilon_p = -\varepsilon_n = L_{\text{eff}-u} - L_{\text{eff}-l}$.

Substituting Eq. 2-21 into Eq. 2-18, the total current can be calculated.

In case B, L_{eff} does not differ much compared with that in the reference situation (*i.e.* the zero surface charge situation in Figure 2.8 (b)). However, the conductivity in L_{eff} is largely enhanced or lowered compared to that of c_0 , hence the following are obtained:

$$\rho_{p/n} = [qN_A(\mu_c + \mu_a)(c_0 \pm \frac{\Delta c_{p/n}}{2})]^{-1} \quad (2-22)$$

$$R_{p/n} = \frac{\rho_{p/n}(L_{\text{eff}-u} + L_{\text{eff}-l})}{S_0} \quad (2-23)$$

Finally, according to the commonly used definition, the current rectification factor RF is calculated to be.

$$RF(c_0, d_p, \theta, h, \sigma, U) = \frac{I_p}{I_n} = \frac{R_n}{R_p} \quad (2-24)$$

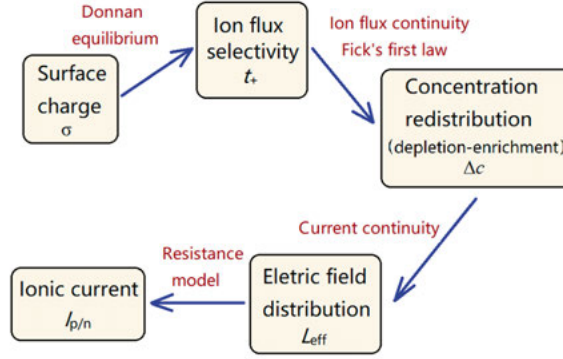


Figure 2.10. Block diagram for the physical process underlining the rectification behavior of ionic current in nanopores. The factors in the blocks are related physical quantities, while the items on the arrow lines present the relationship connecting adjacent factors.

Real-life situations can lie between case A and B. Therefore, a weighting factor ν (ranging from 0 to 1) is introduced to blend the components of case A and B through a weighted geometric means [179] of RF in both cases, since RF is a ratio variable.

$$RF = RF_A^\nu RF_B^{1-\nu} \quad (2-25)$$

where, RF_A and RF_B are the rectification factor of case A and B respectively.

By now, the analytical model of ionic current rectification is established and the vein of the causal chain connecting the key physical factors is clearly unveiled as summarized in Figure 2.10.

As expected, the major factor influencing ν is θ . Comparing the COMSOL simulation results with model predictions in Figure 2.11, it can be clearly seen that RF of small θ nanopores can be well predicted by case B of our model represented as the red line in the figure. Moreover, the green asymptotic line represents case A of our model and it coincides well with the simulation results for large θ . The transition from case B to A occurs between 45° and 80° .

In order to further verify the effectiveness of the model and strengthen the understanding of the physical process behind, RF of a series of cone nanopores from COMSOL simulation and TPP from experimental measurements are systematically compared with that predicted by the model, by changing diameter, electrolyte concentration, bias voltage, surface charge density, and membrane thickness. The results and related discussion can be found in Figure 4 and 5 in **Paper III**. It can be seen that, the model predicts the rectification behaviors very well, which offers a powerful tool to facilitate the insight into the physics behind, to guide the design of ion rectified devices, and to explore new mechanisms of ion transport in both natural and artificial systems.

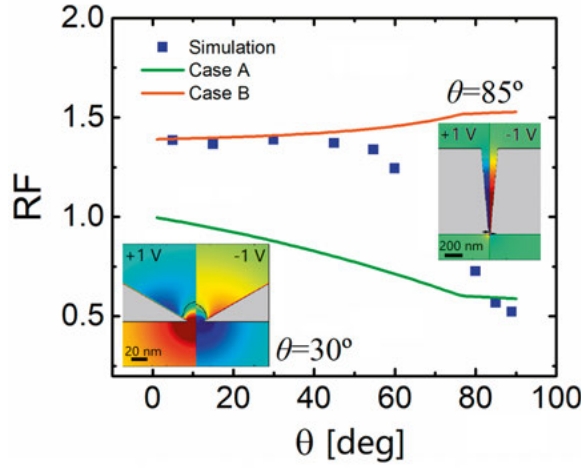


Figure 2.11. Variation of RF with the angle of the sloped sidewall θ at 1 V bias voltage. The green and red curves represent case A and B of our model, respectively. Inset: simulation results showing the distribution of ion concentration (sum of the cation and anion concentrations) in a truncated-cone nanopore with $\theta=85^\circ$ and $\theta=30^\circ$, respectively. For a clear comparison, the distribution at +1 and -1 V is, respectively, plotted at the left and right half of the figures. The warm colors mark the ion-enriched region (c_H region), while the cold colors the ion-depleted region (c_L region).

Specifically, surface charge is an important parameter to tune the current rectification property of nanopores, since it is the origin of the rectification. The current-voltage (I-V) characteristics of a 20 nm-side length TPP were measured in various concentrations of KCl electrolytes under different illumination conditions. The light condition was achieved by a white LED located above the nanopore chip, while the dark environment was realized by using a closed metal Faraday cage. According to the fitting results based on the model referring to Section 2.1.4, the surface charge density can be extracted in dark and light conditions (Figure 2.12 (a)). As expected, light can excite carriers in the silicon membrane and a higher surface charge density in nanopore is observed than that in dark. Therefore, a higher rectification factor is found in the light condition in both 10 mM and 50 mM KCl electrolytes, as shown in Figure 2.12 (b).

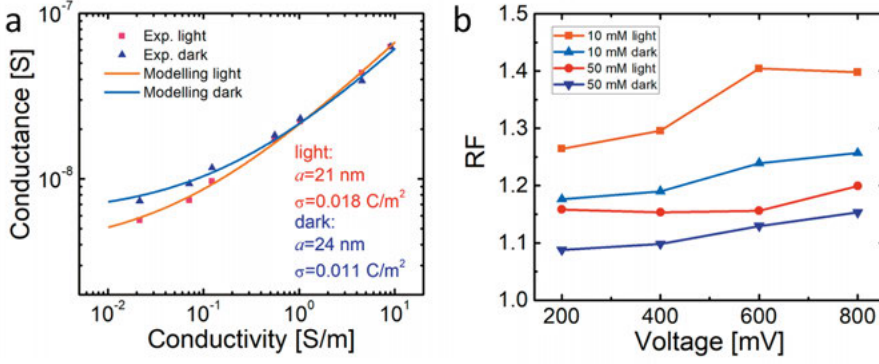


Figure 2.12. Surface charge density and current rectification factor at light and dark conditions. (a) Variation of conductance of a 20 nm side length TPP as a function of electrolyte conductivity under light and dark conditions. (b) Variation of RF with bias voltage in 10 mM and 50 mM KCl under light and dark conditions.

2.3. Origins of nanopore noise

Noise is another important aspect of nanopore, accompanying with signal. A lower background noise level offers more chances to restore weaker signal with a higher fidelity. For a nanopore sensor, the structural and biophysical information of analytes is embodied by the rhythm of the tiny current changes during the single molecule translocation. Apparently, controlling the background noise is crucial for extending the detection capability. To suppress the background noise, the origins of noise should be clarified. Below, we study the noise characteristics using SiN_x nanopores in KCl electrolytes as a representative example.

2.3.1. Identification of noise components

The power spectrum density (PSD) of current noise of a solid-state nanopore can be described phenomenologically by a polynomial [99], [180]:

$$S_I = a_1 \frac{1}{f^\beta} + a_2 + a_3 f + a_4 f^2 \quad (2-26)$$

where, f is frequency and a are coefficients. It is composed of low frequency flicker noise a_1/f^β ($\beta=1$ to 2) [181], [182], white thermal noise a_2 , dielectric noise $a_3 f$ [100], [183], and capacitive noise $a_4 f^2$ [101]. The white thermal noise is calculated from the nanopore resistance by:

$$S_{IT} = a_2 = \frac{4kT}{R} \quad (2-27)$$

where, k is the Boltzmann constant, T is absolute temperature in Kelvin, and R is the resistance of the nanopore. The dielectric noise is determined by the parasitic capacitance of the membrane C_{chip} , wherein the nanopore is located.

$$S_{ID} = a_3 f = 8\pi k T d C_{\text{chip}} f \quad (2-28)$$

where, d is the dielectric loss factor of the membrane material. The capacitive noise is coupled by the input noise of the current readout amplifier [100], [101], [183], which can be expressed as [184]:

$$S_{IC} = a_4 f^2 = (2\pi f C_{\text{total}})^2 e_n^2 \quad (2-29)$$

where, C_{total} is the total capacitance of the system, including the membrane capacitance C_{chip} , the stray capacitance of the feedback resistor, and other parasitic capacitance from amplifier input port and connecting wires. e_n is the equivalent voltage noise of the amplifier input port.

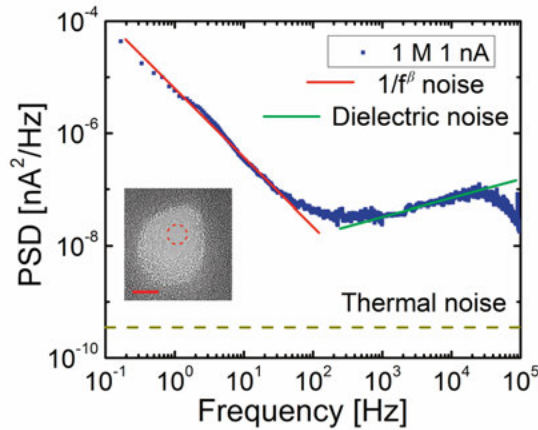


Figure 2.13. Typical current noise PSD of a 7.2 nm SiN_x nanopore in 1 M KCl electrolyte biased at a constant current of 1 nA. Inset: TEM image of the nanopore with the red dash line to indicate how a 7.2 nm pore would fit in. Scale bar: 10 nm. Adapted with permission from [185]. Copyright (2017) American Chemical Society.

Figure 2.13 shows a typical noise PSD of a 7.2 nm-diameter nanopore in a 20 nm thick SiN_x membrane in 1 M KCl electrolyte biased at a constant current of 1 nA. The size of the nanopore is extracted from its conductance measurement with the assistance of the model in Section 2.1.2. The transmission electron microscope (TEM) micrograph is included as inset. It can be divided into different frequency ranges according to the dominating noise component. In the low frequency range below ~ 100 Hz, PSD is proportional to the reciprocal of frequency, so it is dominated by flicker noise. In the frequency of 100 Hz-10 kHz, PSD is taken over by dielectric noise, which is proportional to frequency. At the frequency above 100 kHz (beyond the

measurement range), PSD should be controlled by the frequency-square behavior of capacitive noise. However, 100 kHz is still not high enough to observe it in our nanopore system. The thermal noise component is relatively small, calculated as the dash line in the figure.

2.3.2. Low-frequency noise properties

The high frequency noise, *i.e.* the dielectric noise and capacitive noise, mainly relies on the parasitic capacitance of nanopore chip and measurement equipment, which is simple and clear. However, the low frequency noise is strongly dependent on many key parameters related to the nanopore and electrolyte which can be easily designed and engineered, such as the pore size, electrolyte concentration, and pH. Therefore, the low frequency noise is focused and scrutinized next.

A systematic study on the characteristics of the low frequency noise of the SiN_x nanopores was performed by changing electrolyte concentration and nanopore size, at various of current biases. The detailed results can be found in Figure 2 and 3 in **Paper IV**. From the results we can see that by raising the current, the noise level increases. However, PSD does not obey the current square dependence as predicted by Hooge's theory for the flicker noise [133], [186].

$$S_{IF} = \frac{a_I}{f^\beta} = \frac{a_H I^2}{N_C f^\beta} \quad (2-30)$$

where, a_H is the Hooge parameter and N_C is the total number of conducting carriers. The deviation from the flicker noise model appears more obviously for higher concentrations of electrolyte in lower current region. The much weaker dependence of the noise PSD on current is observed in larger pores, contradictory to the square relationship.

In order to identify the cause responsible for such inconsistencies, possible additional noise sources than the nanopore itself in the system were scrutinized. To exam the noise from the Ag/AgCl electrodes, the nanopore chip was replaced with a resistor of 100 k Ω , 1 M Ω , and 10 M Ω , making the setup with two lids each with its own Ag/AgCl electrode sandwiching a KCl solution to complete the loop, as shown the inset of Figure 2.14 (a). Being outside the KCl solution, this resistor imitates the resistance generated by the nanopore. From the noise PSD of Ag/AgCl, the current dependence of noise was found to be negligible, which indicates that it is not flicker noise but rather a $1/f$ -shape PSD that is at work. Figure 2.14 (a-c) compares the noise PSD obtained for different KCl concentrations, and it also shows a weak dependence on KCl concentration. However, it gives a nearly square dependence on the resistance of the series resistor. A lower noise level is generated when a larger resistor was connected to the Ag/AgCl electrodes. According to the analysis and conclusions in [187], noise from the electrodes is

a modulated thermal noise by the non-flat band frequency response of the electrode-solution interface. Hence, the Ag/AgCl electrodes work as a voltage noise source and induce current fluctuations on the resistance of nanopore. As shown in the left panel of Figure 2.14 (d), S_v represents the voltage noise source from the Ag/AgCl electrodes and S_I is the flicker current noise generated by the nanopore itself. R is the total resistance of the system, mainly determined by the nanopore. In the current noise measurement shown in the right panel, the effect of S_v is equivalent to a current noise source S_I' with an intensity of S_v/R^2 that in its turn is connected in parallel with S_I . Thus, the total noise intensity is the sum of S_I and S_I' . Furthermore, the amplitude of this thermal voltage noise was measured to be around 10^{-12} V²/Hz@1Hz. Overall, the low frequency noise in solid-state nanopore is mainly contributed by two sources, *i.e.* the internal flicker noise from the nanopore and the external thermal noise from the Ag/AgCl electrodes, as shown with the equivalent circuits in Figure 2.14 (d).

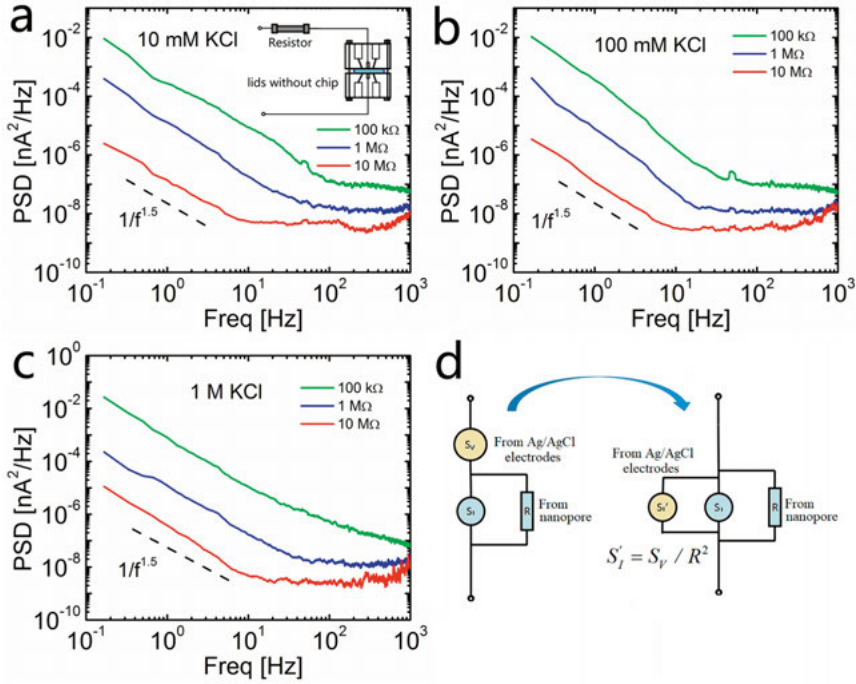


Figure 2.14. PSD of the $1/f$ -shape noise from the Ag/AgCl electrodes. (a-c) Noise PSD from the Ag/AgCl electrodes in series with a resistor of 100 k Ω , 1 M Ω , and 10 M Ω , in KCl electrolytes with concentration of 10 mM, 100 mM and 1 M. Bias current: 20 nA. (d) Equivalent circuits of the noise sources in nanopore.

2.3.3. Origin of the flicker noise

The flicker noise is attributed to the fluctuation of carrier number and mobility with distributed time constants [186]. In the nanopore system, the number of carriers (*i.e.* ions) in the high electric field region, which determines the conductance, bear the thermal fluctuation naturally. As discussed in Section 2.1.4, the total ionic current is contributed by the movement of ions in both the surface EDL and the bulk region beyond the EDL [157], [159]. As shown in Figure 2.15 (a), a 95 nm diameter nanopore has a higher noise level for higher concentrations of KCl with pH=5 at 100 mV bias voltage, which indicates that the bulk conductance surely contributes to the flicker noise, since the surface current in this series of measurements was kept constant at a constant pH. On the contrary, varying surface current with a constant bulk current can be achieved by changing pH but keeping a constant KCl concentration. As shown in Figure 2.15 (b), it also gives a pH-dependent noise PSD, reaching its maximum at pH=5. It proves that the surface conductance acts as an equally important role as the bulk conductance in contributing to flicker noise. Interestingly, SiN_x has a PZC at pH~5 [160], which coincides with the maximum noise level at this pH for the lowest ion amount (N_c) in EDL.

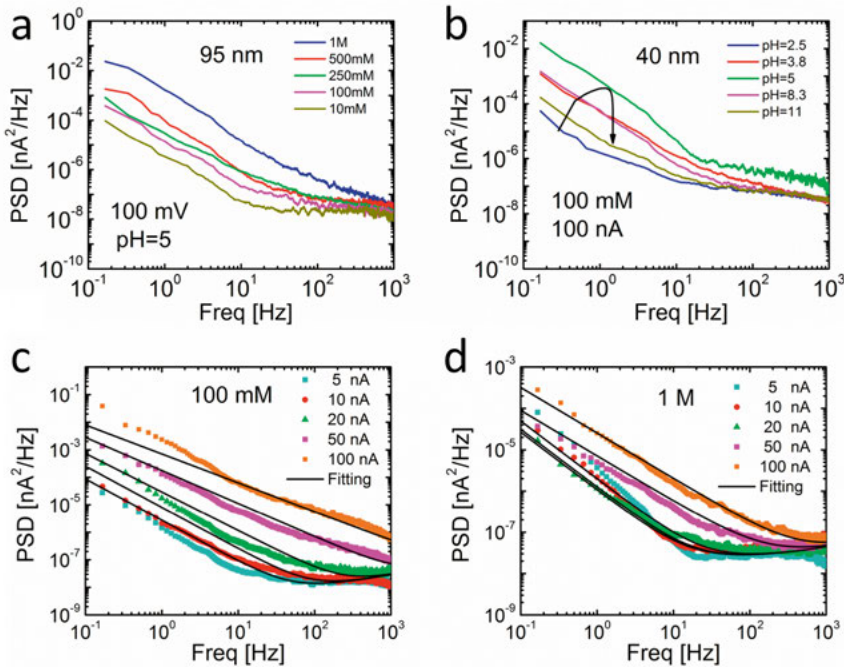


Figure 2.15. Noise PSD of nanopores in various conditions. (a) Noise PSD of a 95 nm nanopore in KCl solution of different concentrations under a constant bias voltage of 100 mV and with pH=5. (b) Noise PSD of a 40 nm nanopore in electrolyte of 100 mM KCl but different pHs, under a constant

current bias of 100 nA, with the curled arrow helping show how the noise level first increases and then decreases with increasing pH. (c, d) Model fitting to the noise PSD of a 65 nm nanopore under different biased current in electrolyte of 100 mM, and 1 M KCl concentrations, respectively. Adapted with permission from [185]. Copyright (2017) American Chemical Society.

2.3.4. Overall noise model

So far, all the possible noise sources in a solid-state nanopore have been identified and modeled, which are summarized in Figure 2.16. They include flicker noise from surface conductance and bulk conductance, S_{IS} and S_{IB} , $1/f$ -shape thermal noise from the Ag/AgCl electrodes, S_{IE} , thermal noise from nanopore, S_{IT} , dielectric noise from the parasitic capacitance of the nanopore membrane, S_{ID} , and capacitive noise from the amplifier, S_{IC} . Therefore, the total current noise PSD, S_I , can be expressed as:

$$S_I = S_{IS} + S_{IB} + S_{IE} + S_{IT} + S_{ID} + S_{IC}$$

$$= \frac{\alpha_H I_S^2}{N_{C,S} f^\beta} + \frac{\alpha_H I_B^2}{N_{C,B} f^\beta} + \frac{a_e}{f^\beta} + \frac{4kT}{R} + 8\pi kT d C_{chip} f + (2\pi C_{total} f)^2 e_n^2 \quad (2-31)$$

where, I_S and I_B are the surface and bulk current, respectively. $N_{C,S}$ and $N_{C,B}$ are the total number of ions inside the EDL and in the bulk region. a_e is the current noise parameter for the electrodes. The surface and bulk current can be calculated referring to Section 2.1.4. And the total carrier numbers in the surface and bulk regions are:

$$N_{C,S} = \sigma \pi d_p h \quad (2-32)$$

$$N_{C,B} = \frac{\pi}{2} d_p^2 h c_0 N_A \quad (2-33)$$

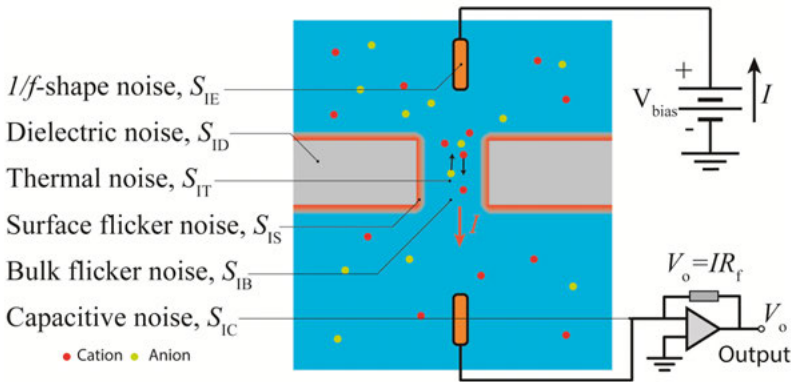


Figure 2.16. Noise sources in a solid-state nanopore system.

Experimental results of the noise PSD in different situations are fitted by this comprehensive model, as shown with two examples in Figure 2.15 (c, d). It is worth noting that only three parameters, α_H , a_e and β , are adjusted to give the most optimized match at all biased current for a given KCl concentration. The extracted values of α_H concentrate around its average value of 1.9×10^{-4} , which agrees well with the values reported by others [132], [180], [188]. Furthermore, a_e increases linearly with KCl concentration, validating the conclusion that a higher current fluctuation can be generated by the voltage noise source loading a lower resistance nanopore.

2.4. Characteristics of signal and noise

In above sections, we have unveiled the physical essences of the resistance and rectification in open-pore state, as well as scrutinized the various origins of nanopore noise in different frequency ranges. The next critical issue to consider is the translocation characteristics of analytes through nanopores. Let's shift our focus to a higher hierarchy, namely a system level, in the perspective of signal and noise properties based on a simple yet powerful model. The translocation of single-stranded DNA (ssDNA) through solid-state cylinder nanopores is selected as a representative example in the model. each nucleotide on the translocating DNA strand is treated as a well-defined nano-disk of infinite resistance, and only the steric blockage on ionic current is taken into account to estimate the signal level (*i.e.* current blockage). Though the model ignores many effects which may sculpt the blockage current, such as nucleotide morphology and deformation, charges on DNA strand, *etc.*, it outlines the coarse picture of the complex DNA translocation process unravelling the entanglement of so many factors, which could guide the design of nanopore sensors and systems. More importantly, it offers a general methodology to analyze the signal and noise characteristics in nanopore systems, and is flexible enough to fuse with different models about open-pore current, blockage event, and noise, in different scales from molecular dynamics to system architecture, with different accuracies.

2.4.1. Correlation of signal amplitude to nanopore geometry

In the model, nucleotides are represented as hard nano-disks with their sizes corresponding to the van der Waals area of all atoms in the nucleotides [189], [190] and their thickness as the distance between two adjacent nucleotides in ssDNA [191]. The equivalent diameter of the four nucleotides can be found in Table 2.2. They thread through the nanopore, during which extra resistance will be generated from the disk-strand by occupying a certain volume in both the pore and access regions.

Table 2.2 Equivalent diameter of the four nucleotides converted from their van der Waals area

Nucleotides	Adenine (A)	Thymine (T)	Guanine (G)	Cytosine (C)
Van der Waals area [nm ²]	1.966	1.931	1.993	1.798
Equivalent diameter [nm]	1.582	1.568	1.593	1.513
Reference	[190]	[190]	[190]	[190]

As shown in Figure 2.17 (a), the total blockage of the ionic current can be equivalent to a series of resistors with different resistances corresponding to the sequence of DNA in the nanopore. Applying the conventional resistance model for the cylinder nanopores, as is presented in Section 2.1.1, pore resistance, $R_{p,o}$, access resistance, $R_{a,o}$, and total resistance, $R_{t,o}$, can be calculated by [146], [147]:

$$R_{p,o} = \frac{4h\rho}{\pi d_p^2} \quad (2-34)$$

$$R_{a,o} = \frac{\rho}{2d_p} \quad (2-35)$$

$$R_{t,o} = R_{p,o} + 2R_{a,o} \quad (2-36)$$

The second subscript ‘o’ in the variables indicates that the resistances are the ‘open-pore’ ones. If just one nucleotide is in the pore region or access region, the caused resistance increase can be simply estimated by the steric blocking:

$$\Delta R_p = R_{p,b} - R_{p,o} = \frac{4\rho d_s d_D^2}{\pi(d_p^2 - d_D^2)d_p^2} \quad (2-37)$$

$$\Delta R_a = R_{a,p} - R_{a,o} = \frac{\pi\rho d_s d_D^2}{d_p^2(4d_p^2 - \pi d_D^2)} \quad (2-48)$$

where, d_s is the distance between adjacent nucleotides in ssDNA. d_D is the diameter of nucleotides. The second subscript ‘b’ represents the resistances with nucleotide(s) in the corresponding region, *i.e.* the ‘blockage’ state. Thus, the total resistance increase of the pore when a strand of nucleotides in it can be calculated by summing up the resistance increases generated by each one.

$$R_{t,b} = R_{t,o} + \sum \Delta R_p + \sum \Delta R_a \quad (2-39)$$

At a given bias voltage U , the open-pore current and the blockage (residual) current are $I_0 = U/R_{t,o}$, and $I_b = U/R_{t,b}$, respectively. For convenience, we used normalized I_b (to I_0) in the following discussion.

This model is implemented by a MATLAB program. As shown in Figure 2.17 (b), the blockage current waveform is generated by a test DNA sequencing, AAATTTGGGCCCCATGCATGCATGCAAATTTGGGCCCCATGCATGCATGC, in various situations, such as different pore diameters (the first row), membrane thicknesses (the second row), and translocation speed (the last row). The sampling rate for all the cases is set to be 10 kHz, which

is adequate for the typical translocation speed (1 nt/ms). It can be seen that the detailed features of the waveform (*i.e.* the small fluctuations at the bottom of the blockage valley) are sharper and clearer with a higher relative amplitude (normalized to the open-pore current) from a pore of smaller diameter and thickness, and with a slower translocation speed. If the translocation speed is too fast, for example 100 nt/ms (last panel in the last row), 10 sampling points per ms for 10 kHz sampling rate is not adequate to capture the current change details caused by different nucleotides, but only a translocation spike outline is recorded.

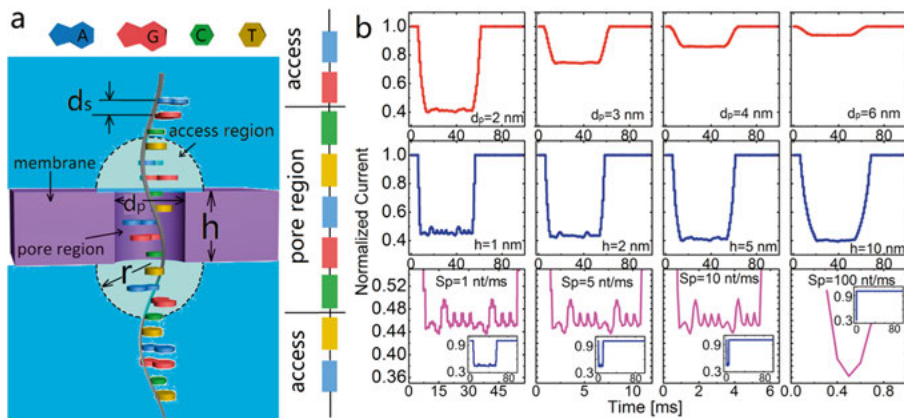


Figure 2.17. Nano-disk model and the calculated translocation waveforms. (a) Schematic translocation of an ssDNA strand in a nanopore, with the critical dimensions defined and the illustrations of the four nucleotides marked in different colors. (b) Waveform of the normalized ionic current (to I_0) with different setups: variation with pore diameter (upper row), pore thickness (middle row), and translocation speed (lower row), all without consideration of the access resistance. The insets of the lower row figures show the overview of the corresponding translocation waveform. In the calculation, the unchanged parameters are set to be their typical values: $d_p=2$ nm, $h=5$ nm, translocation speed: 1 nt/ms. Reprinted with permission from [192]. Copyright (2016) IOP Publishing Ltd.

In order to perceive the features of the translocation waveform and seek the connection to DNA sequence, a blockage waveform generated by a short ssDNA is scrutinized in Figure 2.18 (a). It can be found that the segment of the ssDNA in the nanopore determines the absolute level of current at certain time, and the step-like current changes are caused by the size difference of entering and exiting nucleotides carrying the sequence information. The maximum current step appears when the largest nucleotide, *i.e.* G, enters(exits) and the smallest one, *i.e.* C, exits(enters) the nanopore and the rest nucleotides in the pore are all C.

$$\Delta I_{\max} = |I_{C \dots C_{n-1}} - I_{C \dots C_{n-1}G}| \quad (2-40)$$

where, n is the number of nucleotides in the pore region. $I_{N \dots N}$ ($N=A, G, C, T$) represents the blockage ionic current when the section of an ssDNA with sequence $N \dots N$ is in the pore. Similarly, the minimum current step is found when A enters(exits) and G exits(enters) the pore with all the nucleotides in the pore region being G, since the size difference between A and G is the smallest among all the combinations. The minimum current step can be:

$$\Delta I_{\min} = |I_{A G \dots G_{n-1}} - I_{G \dots G_{n-1}G}| \quad (2-41)$$

The extremums of signal level defined by Eq. 2-40 and 2-41 can be calculated for different sizes of nanopores, as shown in Figure 2.18 (b). The upper and lower surfaces present the maximum and minimum amplitude of normalized signal, respectively.

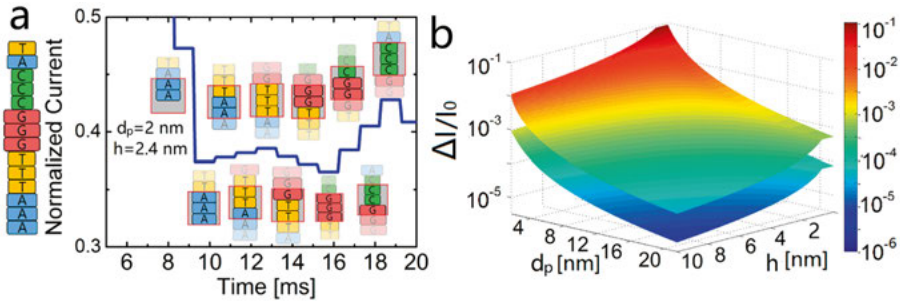


Figure 2.18. Blockage current details and normalized signal levels. (a) Details of the normalized blockage ionic current assisted by a series of cartoons to correlate the position of the nucleotides on a translocating ssNDA to the current level. (b) Normalized signal $\Delta I/I_0$ defining the upper bound ($\Delta I_{\max}/I_0$) and lower bound ($\Delta I_{\min}/I_0$) shown as two curved surfaces for various combinations of d_p and h . Adapted with permission from [192]. Copyright (2016) IOP Publishing Ltd.

2.4.2. Translocation manner

The manner of translocation plays an important role in affecting the step size, $\Delta I/I_0$. Usually, if a DNA strand is driven by electric field without extra control, it translocates a nanopore naturally in a continuous manner. However, special enzymes are likely to be introduced near the pore mouth to grab the DNA so as to slow down the speed of translocation. In this way, the DNA strand is fed to the nanopore nucleotide by nucleotide in a step-wise manner. From the viewpoint of waveform, the differences are obvious between that generated by a continuous manner and a stepwise manner, as shown in Figure 2.19 (a) and (b) respectively. The sequence used in this simulation is “AAAATTTTGGGGCCCCAAAATTTTGGGGCCCC” and the nanopore is

2 nm in diameter and 5 nm in thickness. The translocation speed is set to be 1 base/ms. It is clear that the continuous manner generates a smoother and more gradual change in current, from which the entry and exit of a nucleotide is difficult to be distinguished. Intuitively, it gives additional challenges for the decoding algorithm, compared with the waveform of the stepwise manner. Adapting the similar analysis of the signal margin by Eq. (2-40) and (2-41), referring to stepwise manner, the continuous manner lowers the minimum signal level, $\Delta I_{\min}/I_0$, of $d_p=2$ nm, $h=5$ nm nanopore from 10^{-3} to 10^{-5} . The detailed comparison of the signal level generated from these two translocation manners can be found in Figure 3 in **Paper V**. In reality, such an ideal stepwise feeding is hardly encountered without special arrangements. Such an arrangement will be discussed in Section 2.4.4.

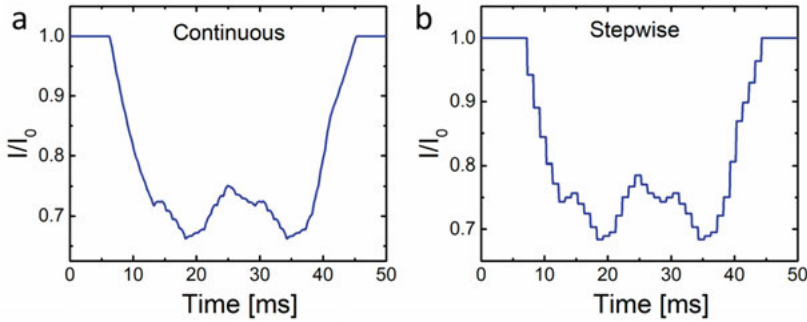


Figure 2.19. Translocation waveform of a ssDNA through a nanopore of $d_p=2$ nm and $h=5$ nm in (a) continuous and (b) stepwise manners. The sequence of the DNA is “AAAATTTTGGGGCCCCAAAATTTTGGGGCCCC”. The translocation speed is set to be 1 base/ms.

2.4.3. Noise properties

The noise characteristics of a solid-state nanopore is systematically discussed in section 2.3, and can be described by Eq. 2-26. To facilitate the discussion about the SNR property in nanopore, typical values of the parameters in Eq. 2-26 (a_i , $i=1-4$) are chosen from the literature [99]: $a_1=1$ pA², $a_2=2.2 \times 10^{-4}$ pA²Hz⁻¹, $a_3=8 \times 10^{-8}$ pA²Hz⁻², $a_4=5.7 \times 10^{-12}$ pA²Hz⁻³. The noise PSD is plotted in Figure 2.20 (a), and its RMS value for different bandwidths can be obtained by calculating the square root value of the integrated PSD (Figure 2.20 (b)). With the assistance of the signal extraction algorithm CUSUM [193], a SNR larger than 4 is needed for the undistorted restoration of signals. Following this criterion and referring to the minimum boundary of signal level in Figure 2.18 (b), the maximum normalized noise RMS is shown in Figure 2.20 (c) for different size of nanopores. Moreover, the requirements for the bandwidth of the system can be obtained by comparing Figure 2.20 (b) with Figure 2.20 (c), and are displayed in Figure 2.20 (d).

The frequency of nucleotide translocation should be kept far below the bandwidth for good resolution and acquisition of enough details (*c.f.* the last row of Figure 2.18 (b)). From the results expected from our analysis, the distinguishability of the four nucleotides brings up harsh requirements on the nanopore, which is not easy to be massively and controllably achieved by state-of-art fabrication technologies, as well as on a low-noise signal readout system. For example, the open-pore current is calculated to be about 3 nA for a nanopore of $d_p=4$ nm and $h=5$ nm in 1 M KCl electrolyte based on our conductance model, and the maximum signal level can only reach 0.2% of I_0 , *i.e.* 6 pA, according to Figure 2.18 (b). The requirement for the noise RMS should be, therefore, smaller than 0.3 pA. It sets a huge pressure on the electromagnetic compatibility design of the readout electronics for a perfect electromagnetic interference shielding and noise cancellation.

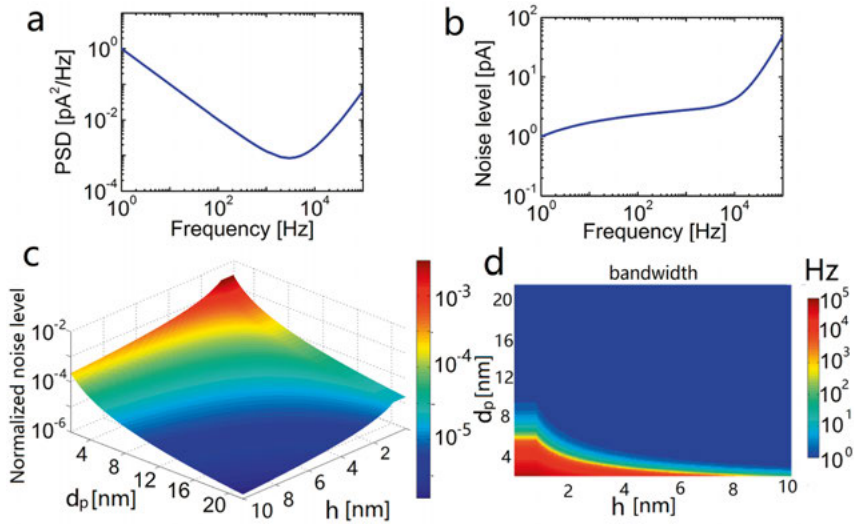


Figure 2.20. Noise characteristics of a typical solid state nanopore system. (a) Typical PSD of noise in a nanopore system adopted from the literature [99]. (b) Noise level at different bandwidth frequency obtained from (a). (c) Normalized noise level, to I_0 , for nanopores of different sizes, with reference to (b). (d) Maximum bandwidth of the measurement system for nanopores of different sizes. Reprinted with permission from [192]. Copyright (2016) IOP Publishing Ltd.

2.4.4. Signal to noise ratio of nanopores

In the previous sub-sections, the simple rigid nano-disk model for DNA translocating nanopore gives us many insights in the signal and noise properties of nanopore at a system level. It points out the way to improve the performance of the nanopore sensors, *e.g.* higher spatiotemporal resolution, that

is boosting the signal and suppressing the noise. It can be implemented from the following aspects:

1. Shrinking L_{eff} . If fewer nucleotides are confined within L_{eff} (pore and access regions) at certain time, a weaker average effect of the nucleotides in the pore is achieved, so that the apparent current changes (*i.e.* signal) can be more solely contributed by the nucleotides entering and exiting the pore. It boosts the relative signal level indicating a higher spatial resolution and is the strategy for the zero-depth interfacial nanopore discussed in Section 2.1.3.

2. Introducing signal amplification mechanisms. Surface functionalization offers chances to introduce certain specifically designed chemical groups/bio-active units, which could have strong interactions with analytes selectively. When the target analytes pass through the nanopore, the interaction may prolong the translocation time and enhance the signal level. This scheme is widely applied in biological nanopores, in which special mutations on amino acid monomer are involved at key positions, *e.g.* narrowest constriction, in the nanopores [54]. In this way, discrimination of the four nucleotides in ssNDA can be achieved.

3. Slowing down the translocation speed. As discussed in the previous sections, the sampling rate, as well as the bandwidth of the system, should be much higher than the number of nucleotides translocating in a unit time (*i.e.* translocation speed). Lowering the translocation speed can help meet requirement on bandwidth of the readout amplifier. More significantly, a largely limited bandwidth means a smaller background noise level (*c.f.* Figure 2.20 (b)), and a higher SNR.

4. Controlling the translocation manner. ssDNA will naturally translocate a solid-state nanopore in the continuous manner driven by an electric field. However, in a biological nanopore sequencing system, usually an enzyme is anchored near the nanopore, which can grab the ssDNA and feed it to the nanopore in the stepwise manner [52]. It has been proved by the model that the stepwise translocation manner generates the desired step-like changes in blockage current and therefrom significantly enhanced signals, compared with the continuous translocation manner.

5. Suppressing the background noise. According to the reported literature, the natural anti-adsorption property of protein and lipid bilayer surface are responsible for the biological nanopore an ultralow noise level, compared with that in solid-state nanopores [28], [98], [99]. The latter may easily adsorb ions, small molecules, *etc.* rendering fluctuations of the surface charge and ion distribution in the pore, which are reflected as a higher noise level, especially in the low frequency range [130], [194]. A promising solution to suppressing the noise is to cover the solid-state surface of nanopores with a layer of lipid molecules or organic polymers [85], [99], [195].

Overall, on the system level, all the parameters in the nanopore system are entangled with one another, such as the nanopore geometry, the translocation

speed and manner of analyte, the bandwidth and sampling rate of the readout circuit, and the background noise. A comprehensive consideration of all the influencing factors and the interplay among them are necessary for a good design of nanopore sensors.

2.5. Summary of this chapter

This chapter gives a theoretical foundation to the solid-state nanopore sensors, which builds up a frame for ionic current in the open-pore state, the noise origins, and the translocation blockage signal.

Introduction of the concept of effective transport length is instrumental to quantifying the electric field distribution, clarifying the physics essence of nanopore resistance, and determining the nanopore size based on conductance measurement. Furthermore, in the perspective of electric field distribution, the physical causality of ionic current rectification phenomenon is unveiled in nanopores with asymmetrical geometry

Low-frequency noise of solid-state nanopores is composed of $1/f$ -shape noise from electrodes and flicker noise from ionic current. Bulk ionic current dominates the flicker noise for large pores, while surface ionic current dominates it for small pores.

Signal amplification and noise suppression are essential to achieve high SNR for DNA sequencing using solid-state nanopores.

3. Sensor applications of solid-state nanopores

In Chapter 2, in-depth insights in the physical mechanisms of solid-state nanopore sensors have been extensively and comprehensively explored, from which the structural simplicity and physiochemical complexity of nanopores are adequately revealed. Up to now, you may feel that, like me, there is strong impulse to prove the concept in sensing by solid-state nanopores. This chapter intends to cover a significant part of the spectrum, from device to characterization platform, from translocation of DNA and proteins to standardization of signal processing procedure, and from single pore solo to multiple pore symphony. The tiny translocation spikes may echo with your pulse excitedly, while the unpredictable behaviors may quench your fervor ruthlessly. This is just the beauty of nanopores.

3.1. Device and measurement setup

3.1.1. Device fabrication

In my experiments, two kinds of nanopores are used, the cylinder nanopore in SiN_x membrane and the TPP in single-crystal Si membrane.

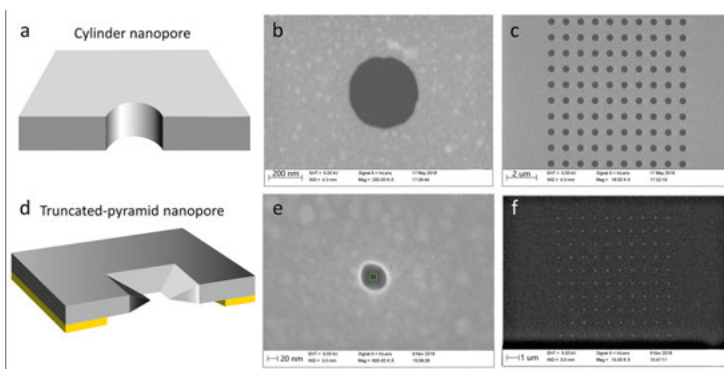


Figure 3.1. Structure of nanopores. (a, d) Schematics of 3D view of cylinder nanopore and TPP, respectively. (b, c) SEM top-view micrographs of a single SiN_x nanopore and an array of 10×10 SiN_x nanopores, all 400 nm in diameter. (e, f) SEM top-view micrographs of a single TPP and an array of 10×10 TPPs, all 10 nm in side length.

The fabrication process for both types of nanopores are adequately developed and optimized by my colleague Shuangshuang Zeng. The process flow of the former can be found in **Paper VIII**, and that of the latter is described in **Paper VI**. The scan electron microscope (SEM) images as well as the schematics of three-dimensional (3D) view are shown in Figure 3.1.

3.1.2. Sample preparation

Adequate cleaning of a nanopore sample prior to measurement is crucial to attain stability and repeatability of the results. Under the ambient conditions, a fresh hydrophilic surface of the nanopore chip bears a slow decay to become hydrophobic. As shown in Figure 3.2, the contact angle of a water droplet on the surface of HfO_2 , SiO_2 , and SiN_x films, which are all commonly used nanopore materials, is shown to gradually increase with time of exposure to air. The decay of the HfO_2 surface is the worst, while that of the SiO_2 surface the best among them. Many publications have been pointed out that a good hydrophilic surface is the prerequisite for a stable connection of the electrolyte at the two sides of the nanopore, which is the foundation to the translocation measurements [126], [196], [197].

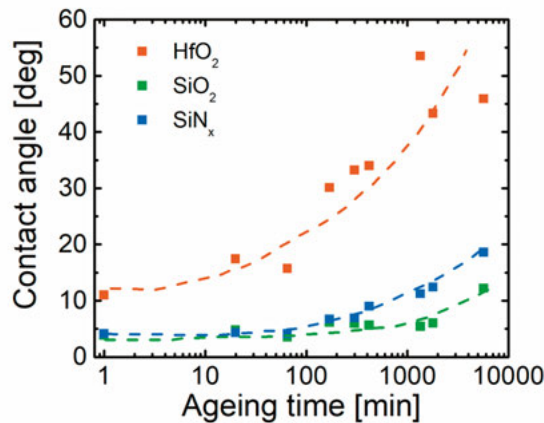


Figure 3.2. Evolution of contact angle with time for HfO_2 , SiO_2 , and SiN_x surfaces under the ambient conditions.

Therefore, before electrical measurement, the nanopore chip was carefully cleaned in oxygen plasma at 1000 W for 10 min, followed by immersion in a piranha solution with $\text{H}_2\text{SO}_4:\text{H}_2\text{O}=3:1$ (volume ratio) for 30 min, and finally rinsed in deionized water. The nanopore chip was then mounted on a custom-made polymethyl methacrylate (PMMA) flow cell and sealed using two polydimethylsiloxane O-rings (8 mm in inner diameter) on the two sides, as shown in Figure 3.3 (c). Two compartments both filled with electrolyte were separated by the chip and the only path of ionic current was through the na-

nanopore. The resistivity of the electrolyte was calibrated using a conductivity meter (Lab 945, Xylem Analytics Germany Sales GmbH & Co. KG). A pair of Ag/AgCl electrodes (2 mm in diameter, Warner Instruments, LLC.) was used to apply a bias voltage across the nanopore and to measure the ionic current (Figure 3.3 (b)).

3.1.3. Measurement setup

The typical design of a weak current signal readout system is, as shown in Figure 3.3 (a), composed of a current-to-voltage converter to change a current signal to a voltage signal, a low-pass filter (LPF) to define the bandwidth of the system, an analog-to-digital converter to sample and digitalize the analog signal, and a data recorder and processor, usually accomplished by software in a computer. Besides, a controllable DC voltage source is included to offer bias voltage across the nanopores.

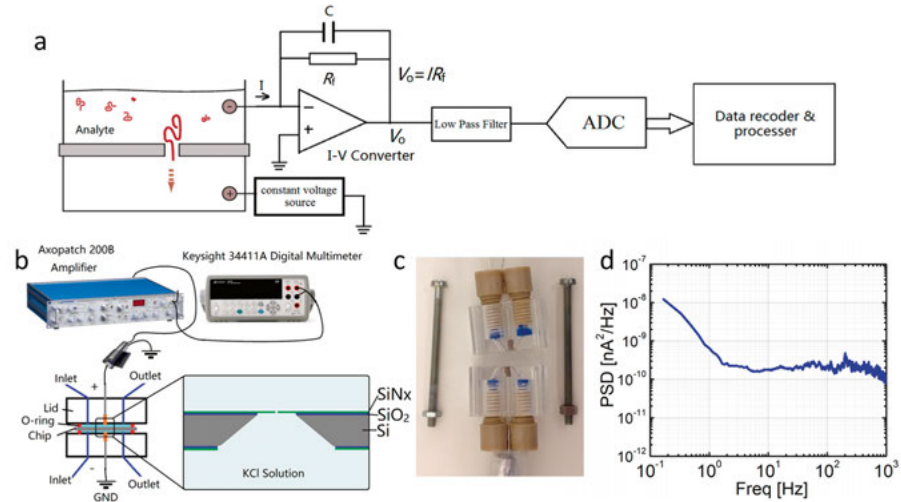


Figure 3.3. Measurement platform. (a) Structure of the readout circuit. (b) Nanopore characterization platform. (c) Photo of the homemade PMMA flow cell. (d) PSD of the background noise from the measurement setup.

The ionic current through a nanopore is usually very weak, varying from 10 pA to 100 nA dependent on pore size and electrolyte conductivity. Therefore, an ultralow background noise of the system is highly desired. For example, for SNR=10, a 1 pA RMS background noise is the minimum requisite, which means an average of 1×10^{-9} nA²/Hz in 1 kHz bandwidth or lower should be guaranteed. It sets a harsh demand on the readout electronics, especially the first stage of the signal chain, *i.e.*, the current-to-voltage converter, to protect the signal integrity. It can be realized by an operational amplifier in a negative feedback configuration as shown in Figure 3.3 (a).

The output voltage is proportional to the input current with a factor corresponding to the feedback resistance. In order to achieve a significant amplification of the weak current signal, a resistor in hundreds of $M\Omega$ to several $G\Omega$ is selected, considering the dynamic range of input current and output voltage. In addition, a small capacitor is parallelized with the feedback resistor to preliminarily limit the bandwidth and stabilize the zero-pole. Sometimes, the parasitic capacitance of the feedback resistor is enough to take the aforementioned functions. The amplification performance largely depends on the quality of the operational amplifier in the first stage, which should have a low input bias current, a low offset voltage and a small offset drift, a low noise level, a very high input impedance, and a small in-band ripple.

The readout system was achieved by using a patch clamp amplifier (Axopatch 200B, Molecular Device Inc.) in our experiments. At its optimized working condition, the background noise, including the internal noise from the amplifier and the external noise from the surrounding interference, can fulfill the measurement of nanopores. The PSD of the background noise is much lower than the noise from the nanopore itself (*c.f.* Figure 2.9 in Section 2.3) shown in Figure 3.3 (d). The entire experimental setup was placed inside Faraday cages on an antivibration table to shield electromagnetic interference, as shown in Figure 3.4.

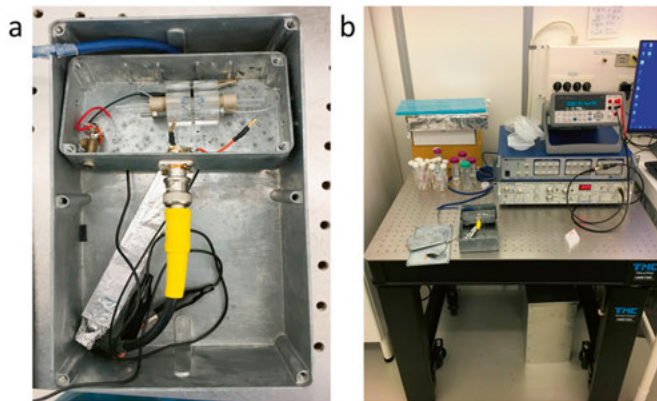


Figure 3.4. Photos of the nanopore measurement platform. (a) Faraday cages containing the nanopore device sandwiched by the PMMA flow cell. (b) Amplifier, digitalizer, and multimeter on an antivibration table.

3.1.4. Data acquisition

In the I-V characterization, current was digitalized and recorded by a Data Acquisition (U2300a, Keysight Technologies, Inc., USA) at each voltage level for 5 s after stabilization for 30 s. The applied voltage was varied from -1 V to 1 V with different step sizes. The voltage control and current record

were achieved with a homemade LABVIEW program. For analyte translocation studies, the ionic current was digitalized by Axon Digidata 1550A (Molecular Device LLC.) and recorded using the software Axon pCLAMP 10 (Molecular Device LLC.).

Selection of a suitable bandwidth of the amplifier is a prerequisite for an efficient measurement. As discussed in Section 2.4.2, a wider bandwidth can include more noise, while a narrower one may distort the signal. Prior to the analysis of bandwidth optimization, it is worth recalling the Nyquist sample theorem: *a band limited continuous-time signal can be sampled and perfectly reconstructed from its samples if the waveform is sampled over twice as fast as its highest frequency component.* In other words, the sampling rate should be at least twice the bandwidth. It also means that further increasing the sampling rate for a certain bandwidth is of no help to pick up more information when it is beyond twice the bandwidth. In some work, a very high bandwidth (e.g. 1 MHz) in a hardware signal acquisition is followed by a low cut-off frequency (e.g. 200 kHz-100 kHz) digital filtering [68], [85], [198], [199]. It should be clarified that results of this procedure are exactly the same as sampling data directly by a hardware acquisition with the same bandwidth as the cut-off frequency of the aforementioned digital filter. In order to guarantee undistorted signals (current pulses here), the bandwidth of the amplifier should be larger than the reciprocal of the pulse width. Otherwise, the pulse can be attenuated and dilated. As shown the simulation result from NI Multisim 12.0 in Figure 3.5 (a-c), the pulse amplitude decreases after passing through a 10 kHz bandwidth 4-pole Bessel LPF, and the width broadens if the fed-in pulse width is shorter than 100 μ s. In another perspective, we can define the upper limit of detectable pulses for a certain bandwidth as the amplitude attenuation reaching their half, then the minimum requisite of bandwidth for different pulse widths can be plotted in Figure 3.5 (d). However, attenuation and dilation of the pulses do not mean totally undetectable, if the attenuated pulse still does not disappear in the background noise. Extra attention should be paid in this situation that the amplitude and duration are not accurate any more.

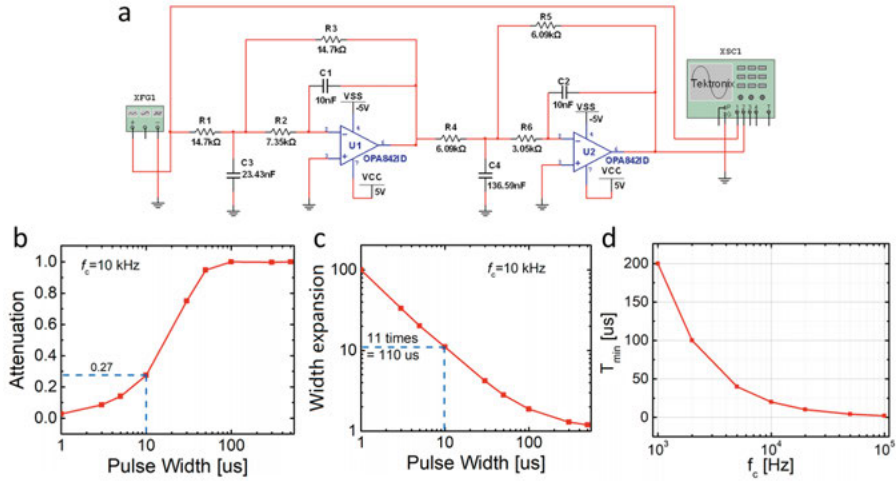


Figure 3.5. Simulation of filtered pulses by a 4-pole Bessel LPF. (a) Schematics of a 4-pole Bessel LPF with a cut-off frequency, f_c , of 1 kHz. (b, c) Attenuation and dilatation of pulses (normalized to the original input value) with different widths through an LPF of $f_c = 10$ kHz. (d) Minimum width of detectible pulses for readout circuits with different bandwidths.

Concerning the background noise level, in our experiment, a 1-5 kHz bandwidth accompanying with a 10 kHz sampling rate is selected for the translocation of λ -DNA and SiO₂ nanoparticles, since the translocation duration is longer than 1 ms. For protein translocation experiment, a 10 kHz bandwidth with 20-50 kHz sampling rate is chosen, which can capture 10 μ s translocation events with the attenuation of one third of its original amplitude.

3.2. DNA translocation in SiN_x nanopores

To demonstrate the nanopore sensing and develop the translocation data processing procedure, λ -DNA was chosen to evaluate a cylinder SiN_x nanopore. λ -DNA has 48502 base pairs in the double-stranded helix structure with the molecular weight of 3.2×10^7 Da. It is about 22 μ m in length and naturally roll up to a sphere with the gyration radius of 730 nm in electrolyte [200]. A 30 nm-diameter SiN_x pore was used and the sample DNA was dispersed in an ethylenediaminetetraacetic acid+tris (hydroxymethyl) amino-methane buffer solution with 2.5 μ g/ml (78 pM) in concentration. The dispersion was of pH=8 and resistivity $\rho = 17.39$ Ω m. The I-V curve of the nanopore before adding DNA sample is shown in Figure 3.6 (a). A slight difference nanopore resistance at positive and negative biases in open-pore state indicates a small asymmetry in geometry and/or surface charge. DNA molecules are heavily negatively charged, as a result of the ionization of hydrogen on phosphate backbone. Therefore, it can be driven by the electric

field and moved through the pore from the low potential side to the high potential side. The translocation experiment was implemented at various bias voltages, ranging from 200 mV to 600 mV. The bandwidth of the readout amplifier was set to 2 kHz with a sampling rate of 10 kHz. As shown in Figure 3.6 (b) at 300 mV bias voltage, the typical translocation signal is spike-like negative current pulse, caused by the blockage of DNA molecules during translocation.

For translocation spikes, three important features are directly connected to the analyte properties: amplitude, duration, and frequency of translocation events (FTE). As shown in Figure 3.6 (c), amplitude is the height of the spike that is larger for a bigger analyte at a higher bias voltage. Duration is the width of the spike measuring the time spent by the translocation, and the longer the analyte and stronger interaction between the analyte and nanopore, the larger the duration. FTE is the reciprocal of the time interval between two adjacent translocation events, and a higher concentration of analyte and a larger bias voltage induce a higher FTE.

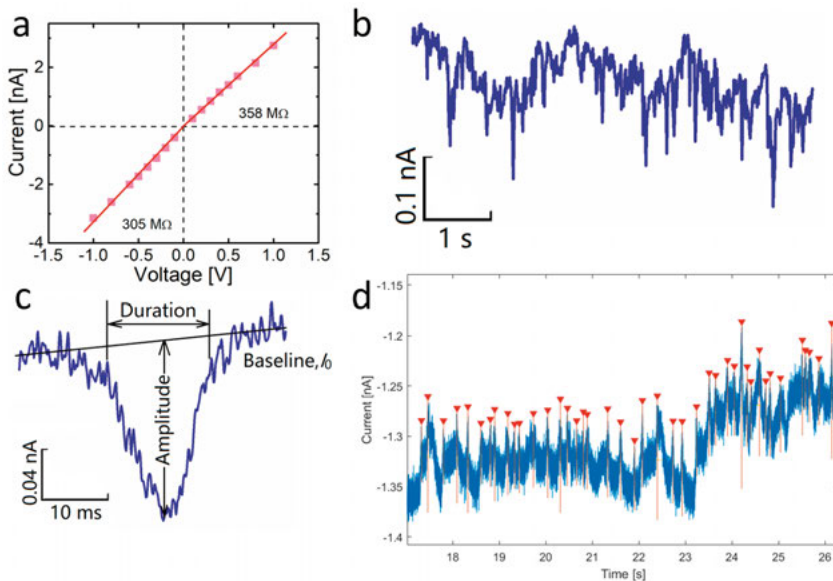


Figure 3.6. Translocation waveform for λ -DNA through a 30 nm diameter cylinder SiN_x nanopore. (a) I-V characteristics of the 30 nm SiN_x nanopore used in the experiment. (b) Current trace showing translocation spikes at 300 mV bias. (c) A typical translocation spike illustrating how duration and amplitude are defined. (d) Translocation spikes automatically extracted by the MATLAB program and marked by red triangles. The current trace is recorded at 200 mV bias voltage.

The translocation spikes are extracted by a homemade MATLAB program using the *findpeaks* function with *MinPeakProminence* method. This pro-

gram can find local peaks in a time sequential data by an assigned amplitude threshold, which is set to be 8 times the RMS average of the background noise. The threshold is optimized and selected by assessing the peak extraction results in a trial and error procedure. Moreover, it can automatically adapt to the slow fluctuation/drift of the baseline current and discriminate a potential peak locally. As shown in Figure 3.6 (d), the translocation spikes are picked up by this program and marked by red triangle dots. Furthermore, the amplitude and duration of every spike, as well as FTE are recorded and statistically displayed in the box chart in Figure 3.7. As expected, with the increase of bias voltage, the amplitude increases, the duration decreases, and FTE increases and levels off above 500 mV.

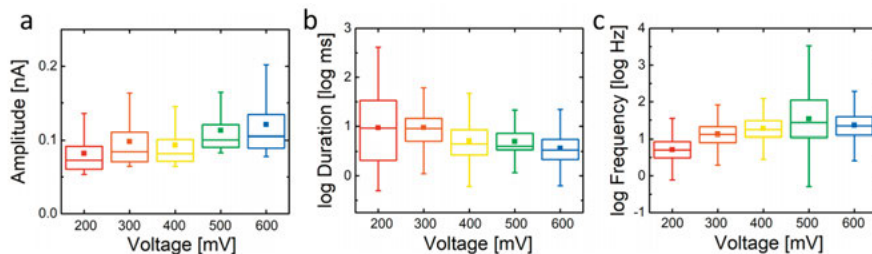


Figure 3.7. Box charts showing the (a) amplitude, (b) duration, and (c) FTE of translocation signals generated by λ -DNA through a 30 nm SiN_x nanopore at different bias voltages.

The translocation events are usually presented by scattering plots according to their amplitude and duration (Figure 3.8), from which distributions of amplitude and duration, as well as its convergence, can be visualized. Furthermore, the clustering pattern of these event points can be used as a classification basis to distinguish different kinds of translocations. For example, the analyte smoothly passing through the nanopore correlates to a relatively short duration and amplitude, while a strong interaction between analyte and nanopore leads to a long duration and a large amplitude.

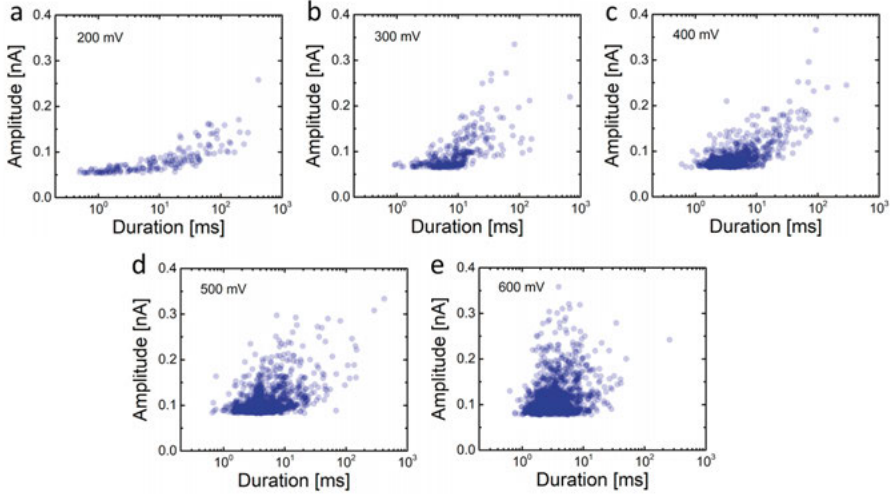


Figure 3.8. Scattering plots showing the distribution of translocation amplitude and duration at bias voltage ranging from 200 mV to 600 mV (a-e).

In order to find representative values for the three variables (*i.e.* amplitude, duration and FTE) to reveal their trends by varying measurement parameters, some statistical feature quantities are adopted, such as mean value and median number. More precisely, their counting frequency can be fitted based on a normal distribution (Figure 3.9). The peak position, x_0 , and standard deviation, w^2 , are two key values of the target function:

$$y = y_0 + Ae^{\left(-0.5\left(\frac{x-x_0}{w}\right)^2\right)} \quad (3-1)$$

The translocation duration and FTE usually do not obey the normal distribution; they generally follow a Poisson distribution [141], [201]. Hence, their logarithmic values are calculated to approach a normal distribution (Figure 3.9 (b, c)). If necessary, more than one normal distribution peak can be involved to represent different clusters of translocation manners [117].

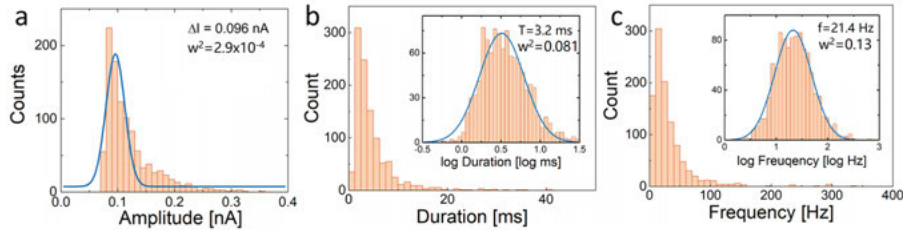


Figure 3.9. Distribution of (a) amplitude, (b) duration, and (c) FTE generated by λ -DNA through a 30 nm SiN_x nanopore at 600 mV bias voltage. Inset: distribution in logarithm scale. The blue lines show the fitting results following the normal distribution.

3.3. Protein translocation in truncated-pyramid nanopores

3.3.1. Formation of vortex in truncated-pyramid nanopores

According to COMSOL simulation, the electroosmotic flow driven by the movement of ions in the diffuse layer of EDL near the surface in the presence of an external electric field can form a vortex inside the nanopore in the asymmetrical TPP structure. The size of the vortex is highly influenced by the distribution of EDL on the pore wall since the net ions in the EDL region are the only driven force to form the electroosmotic flow. In agreement with the previous discussion, we define the positive bias as a positive potential at the LO side (upper side), while the SO side (lower side) is grounded, referring to Figure 3.10 (a). The fixed surface charge of SiO_2 in the $\text{pH} > 3$ solution is negative [160]. Therefore, at positive bias, the electric field drives the mobile net positive ions in the diffuse layer of EDL from the upper side towards the lower side, so do the water molecules (*i.e.* electroosmotic flow) that are dragged by the moving ions. Because of the steric confinement by the smallest constriction of the pore and the relative incompressibility of the electrolyte, part of the downward electroosmotic flow is bounced back to form a vortex. At negative bias, although no steric confinement affects the upward water flow, the flow has to push the bulk liquid forward when it goes out of the pore. This retardation effect turns back the flow and causes a vortex as well, but the size is smaller than that at the positive bias condition. The vortex is easily visualized by mapping the electroosmotic flow velocity in Figure 3.10 (b) for a positive bias at 200 mV and a negative bias at -200 mV, and the boundary of the vortex is defined by an iso-velocity surface of zero velocity.

It can be intuitively inferred that any factor influencing EDL affects the size of the vortex. Increasing KCl concentration causes a slight increase followed by a large decrease of vortex radius, as displayed in Figure 3.10 (c). At very low salt concentrations, EDL may occupy most of the pore volume and offers a large driving force on the water molecules. Thus, only the small part of water in the pore out of EDL will be bounced back resulting in a small vortex. On the other hand, in high concentration electrolytes, EDL is very thin, which indicates that the electric force only applies on a very small region off the pore wall. It appears that the water flow is not so crowded on the SO side of the nanopore thereby resulting in a relatively small vortex. Another crucial factor affecting EDL is surface charge density. As shown in Figure 3.10 (d), the radius of the vortex decreases as the surface charge polarity changes from negative to positive. The polarity of surface charge determines the direction of electroosmotic flow. Compared with the negatively charged surface situation, positive surface charge causes an upward flow and the induced vortex is relatively weak here. As summarized in Figure 3.10 (e-g), by increasing the (abso-

lute) bias voltage, decreasing the diameter of nanopore, raising the thickness of the membrane, and sharpening the angle between the membrane surface and the sloped sidewall, the radius of vortex increases.

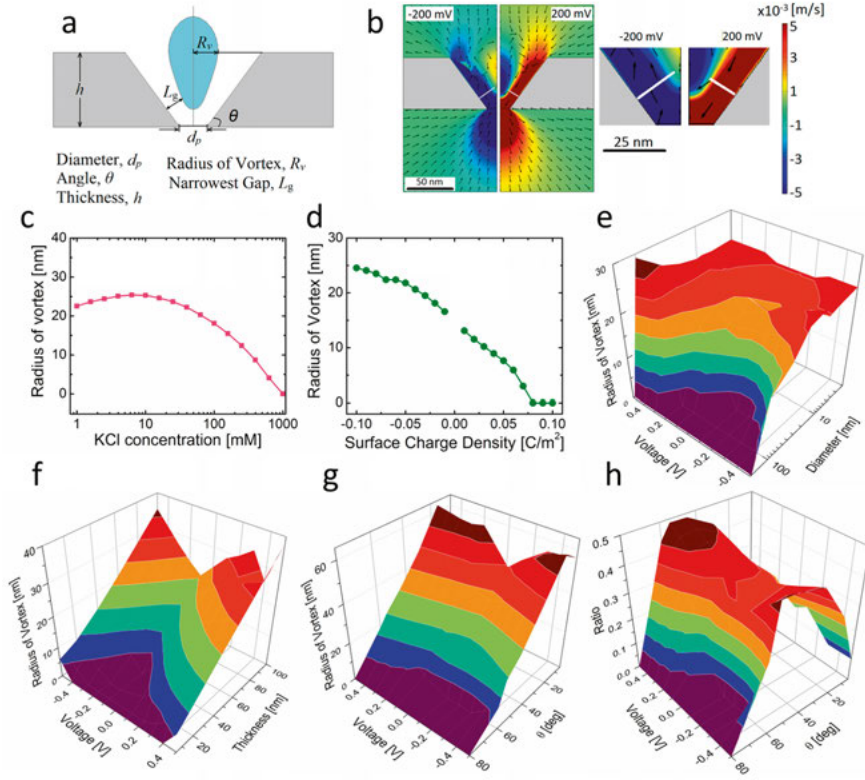


Figure 3.10. Formation of the electroosmotic vortex in TPP. (a) Schematics showing the key parameters of a vortex. (b) Electroosmotic flow velocity distribution at -200 mV (left half) and 200 mV (right half), left, and a close-up view of the narrowest gap region, right. Warm colors (red and yellow) indicate downward flows, while cold colors (blue and green) present upward flows. The small black arrows indicate the direction of the flow, from which a vortex is clearly visible in the center of the pore. The smallest gap between the vortex and the nanopore sidewall is indicated by the short white lines. (c) Dependence of the vortex radius on KCl concentration. (d) Dependence of the vortex radius on surface charge density. At $\sigma=0$ for no charge on the nanopore sidewall, no vortex is formed. (e-g) The radius of vortex changes with nanopore diameter, membrane thickness, and angle of sloped sidewall at different bias voltages. (h) The ratio of vortex radius to LO radius of the nanopore changing with the angle of the sloped sidewall at different bias voltages. In simulation (c-h), the unchanged parameters are set to their typical values, $d_p=20$ nm, $h=55$ nm, $\theta=54.7^\circ$, $U=200$ mV, $c_0=100$ mM, $\sigma=-0.02$ C/m².

The existence of the vortex provides a potential of reducing the effective size of nanopore by narrowing down the path of analyte translocation. The occupation ratio of vortex to the LO side of the nanopore is calculated by changing θ at different bias voltages (Figure 2.10 (h)). Interestingly, it shows a saddle shape surface indicating a maximum at θ around 45° . Furthermore, the narrowest gap between the vortex and nanopore sidewall is used to gauge the effective dimension of the translocation channel (see Figure 5 (c-e) in **Paper VI**). In general, it can reach around half of the nanopore diameter.

It is worth mentioning that the length scale relevant to our nanopores is not particularly small as it would appear and the existing classical models used in COMSOL simulations do apply, since the number of water molecules in the pore and the number of surface ions on the pore wall are still considerable values. For example, as shown in Figure 3.11, in an $a=20$ nm TPP in a 55 nm membrane with $\theta=54.7^\circ$ and surface charge density of -0.02 C/m², the volume of this truncated-pyramid is 2.2×10^{-22} m³. The density of water is 10^6 gm⁻³. The weight of one water molecule is 18 gmol⁻¹/ 6.02×10^{23} mol⁻¹ = 3×10^{-23} g. Thus, the total number of water molecules is 2.2×10^{-22} m³ $\times 10^6$ gm⁻³ / 3×10^{-23} g = 7.4×10^6 . The surface area of the TPP sidewall is 1.6×10^{-14} m². Thus, the total number of elementary charge is 1.6×10^{-14} m² $\times 0.02$ Cm⁻² / 1.6×10^{-19} C = 2000.

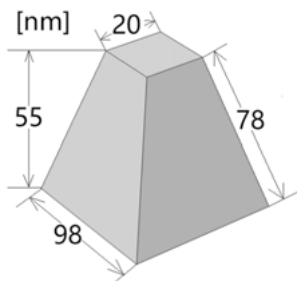


Figure 3.11. Schematic showing the dimension of a TPP nanopore.

3.3.2. Influence of vortex on protein translocation

The electroosmotic vortex may influence the translocation behavior of proteins, since many kinds of proteins are weakly charged. They are dragged by the electroosmotic flow through viscosity force, referred to as electroosmotic force, F_{EOF} , instead of electrophoresis force, F_{elec} . For example, for protein Streptavidin, the point of isoelectric (pI) is around 5. Hence, it is negatively charged at pH=7.4 and F_{EOF} and F_{elec} act on it at the opposite direction. As shown in Figure 3.12, by loading Streptavidin only on the LO side of the TPP, the translocation events only happen at a positive bias voltage. At the positive bias voltage, the Streptavidin translocation direction is identical to that of F_{EOF} . And at the negative bias voltage, F_{elec} is not strong enough to

overcome F_{EOF} to drive the streptavidin translocation. This observation directly proves that the Streptavidin translocation is dominated by F_{EOF} .

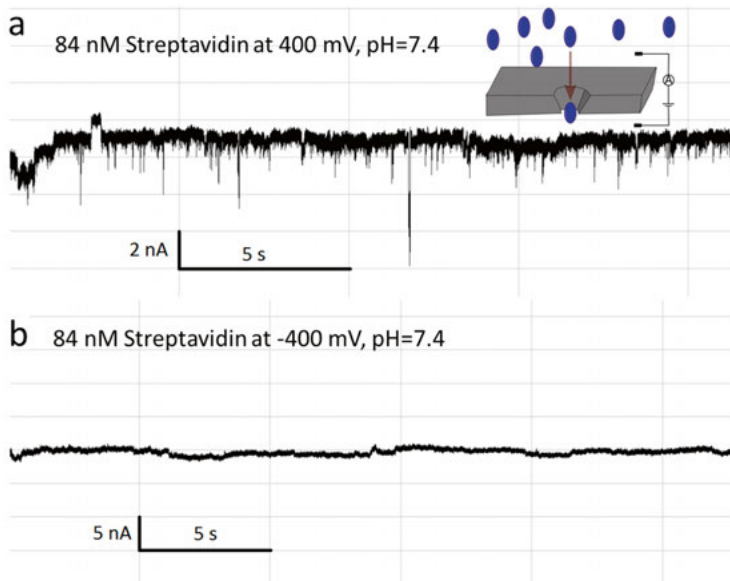


Figure 3.12. Current traces at 400 mV (a) and -400 mV (b) for Streptavidin in TPP of $a=18$ nm at $pH=7.4$. The inset shows the schematic of the setup and Streptavidin is only added to the LO side of the TPP.

It can be conceived that once proteins are captured by the vortex, they have less chance to translocate the nanopore. In order to embody the effect of the vortex experimentally, proteins with different shapes, including Streptavidin and IgG₁, are selected to translocate a TPP of $a=18$ nm in a $\times 5$ PBS buffer with $pH=7.4$. IgG₁ can be approximated as a disc with a diameter around 15 nm and thickness of 8 nm, and with $pI=8.6$, while Streptavidin can be approximated as a sphere with the diameter of 6 nm [85].

Translocation of IgG₁ is firstly detected and Figure 3.13 (a) shows several examples of typical translocation blockage events at different bias voltages. As reported in the literature [202], [203], larger peak amplitudes appears at higher bias voltage. Histograms of FTE are plotted in log format versus both positive and negative biases (+400 mV to -400 mV, 50 mV step) shown in Figure 3.13 (b). A normal distribution is performed to fit histograms. A black line is included to show the trend of the peak position change at different applied bias voltages. Figure 3.13 (c) shows the dependence of the average amplitude of the translocation blockage current on applied bias. The amplitude increases with the applied voltage at both positive and negative bias polarities. To better display and compare the trend of FTE change at positive and negative bias voltages, the data is plotted in Figure 3.13 (d). FTE almost keeps constant at positive bias voltages, while it shows an in-

creasing trend with increasing the absolute value of negative bias voltage. Comparing the size of IgG₁ with the volume of the vortex, IgG₁ is expected to have a strong interaction with the vortex during the translocation. At positive bias voltages, the protein passes the nanopore from the LO to the SO. With increasing voltage, due to the reverse electroosmotic flow in the vortex, intensification of the vortex can effectively suppress the increase of FTE, especially at high bias voltages. However, at negative bias voltages, the protein passes the nanopore in a reverse direction (*i.e.* from the SO to the LO of the nanopore) and the vortex resides in the upper part of the pore. Thus, the vortex has insignificant influence on capturing the protein and FTE increases as the absolute bias voltage increases. The different trends of FTE changing with voltage support of the existence of a vortex inside the nanopore.

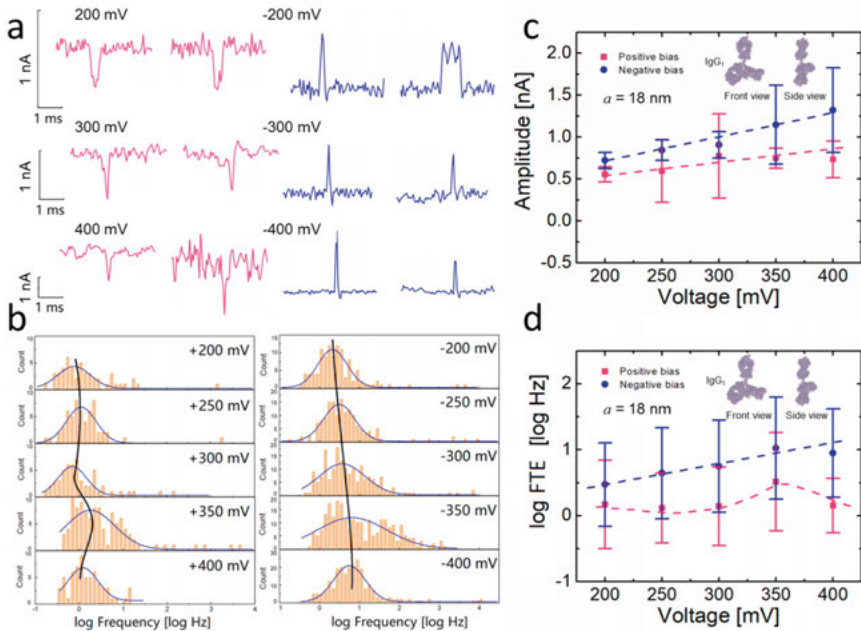


Figure 3.13. IgG₁ translocation through an 18 nm TPP. (a) Some typical translocation blockage events at ± 200 mV, ± 300 mV and ± 400 mV, respectively. (b) Histograms of FTE plotted in a semi-log format at different biases. The solid blue lines represent the fit of a Gaussian distribution to the experimental data and the solid black lines indicate the development of peak position with applied bias. Dependency of (c) average translocation blockage current amplitude and (d) mean FTE on applied voltage. The range intervals in (c) and (d) indicate the spreads of the distribution of corresponding statistic variables. Red: positive bias; Blue: negative bias.

In order to further verify our hypothesis, FTE of smaller-size proteins, Streptavidin, in the same $a=18$ nm TPP is compared with that of IgG₁. In the contrary, FTE of Streptavidin at positive bias is significantly larger than that at

negative bias with the same absolute value of voltage (Figure 3.14 (a)). It can be attributed to its smaller size (6 nm in diameter) compared with the narrowest gap between the vortex and the nanopore sidewall (~ 10 nm). The retardation effect of vortex on downward translocation is hence insignificant. Furthermore, similar to the case of Streptavidin translocating the 18 nm TPP, a larger FTE at positive bias than that at negative bias is also observed in the case of IgG₁ translocating a 73 nm TPP (Figure 3.14 (c)), in which the narrowest gap between the vortex and the nanopore sidewall is much larger than the size of IgG₁. In addition, the translocation experiment of Streptavidin is implemented with a smaller TPP of $a=10$ nm. As expected, FTE at positive bias is smaller than that at negative bias (Figure 3.14 (b)). For a clear comparison, the bias dependent ratio of FTE at negative bias to that at positive bias is plotted in Figure 3.14 (d) for the four groups of aforementioned experiments. The cross-validation further agrees the existence of the electroosmotic vortex. In summary, the presence of an electroosmotic vortex can effectively narrow down the translocation path of analyte to half of its physical diameter, which may enhance the interaction between the high electric field region and the analyte. Furthermore, the vortex has already shown facilitation of identifying different proteins.

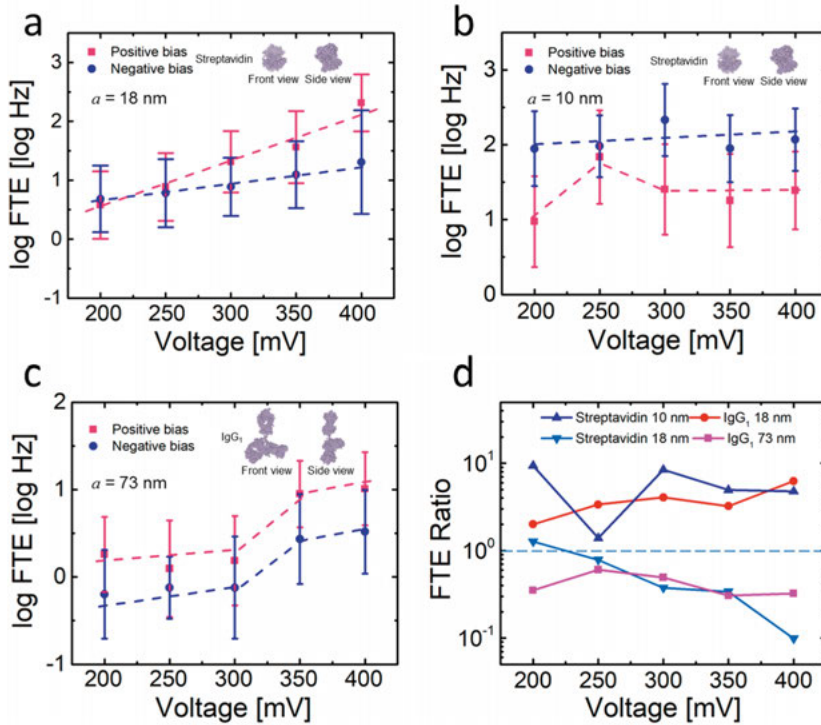


Figure 3.14. Mean FTE for Streptavidin and IgG₁ in TPPs of different a . (a) Streptavidin in the same TPP of $a=18$ nm as in Figure 3.13. The insets show the three-dimensional conformation of Streptavidin with atomic resolution

from the Protein Data Bank. (b) Streptavidin in a smaller TPP of $a=10$ nm. (c) IgG₁ in a larger TPP of $a=73$ nm. The insets show the three-dimensional conformation of IgG₁ with atomic resolution from the Protein Data Bank. The error bars in (a-c) indicate the spreads of the distribution of corresponding statistic variables. (d) Ratio of mean FTE at negative bias to that at positive bias versus applied voltage. Size match between protein and pore dimension appears to play a decisive role.

3.3.3. Translocation of IgG₁ at different pH

The translocation of IgG₁ was also investigated at pH=4 and 10 using an $a=25$ nm TPP. As shown in Figure 3.15, FTE displays different trends by changing the bias voltage compared with those obtained at pH=7.4 (Figure 3.13 (d)). The surface charge on the nanopore sidewall plays a crucial role in establishing the vital electroosmotic force. The PZC of silicon oxide is around 3 [160]. As expected, the (negative) surface charge density of the silicon oxide surface is found to increase when the pH of the solution increases from 4 to 7.4 and then to 10. In the framework of electroosmotic vortex formation, this increase in surface charge density can be translated to decreasing the narrowest gap for protein translocation although the decrease is not drastic. At pH=4, the surface charge density on the nanopore is relatively low, at -0.008 C/m² (Figure 2.7 (a)). As IgG₁ is positively charged, F_{elec} and F_{EOF} act on it along the same direction. The translocation behaves similarly at both negative and positive biases, as shown in Figure 3.15 (a, b). It can be inferred that IgG₁ translocation through the nanopore at pH=4 is mainly driven by F_{elec} instead of F_{EOF} and a schematic illustration is shown in the inset of Figure 3.15 (b). At pH=10, the sidewall of the nanopore is strongly negatively charged, at -0.028 C/m² (Figure 2.7 (c)) and IgG₁ is now negatively charged. Consequently, F_{elec} and F_{EOF} act on it in opposite directions, which can significantly weaken the overall force, as shown in the inset of Figure 3.15 (d). This can explain the observed translocation events of IgG₁ only occurring at very high voltages >850 mV, while the adopted bias voltages for the experiments at pH=4 and pH=7.4 range from 150 mV to 400 mV.

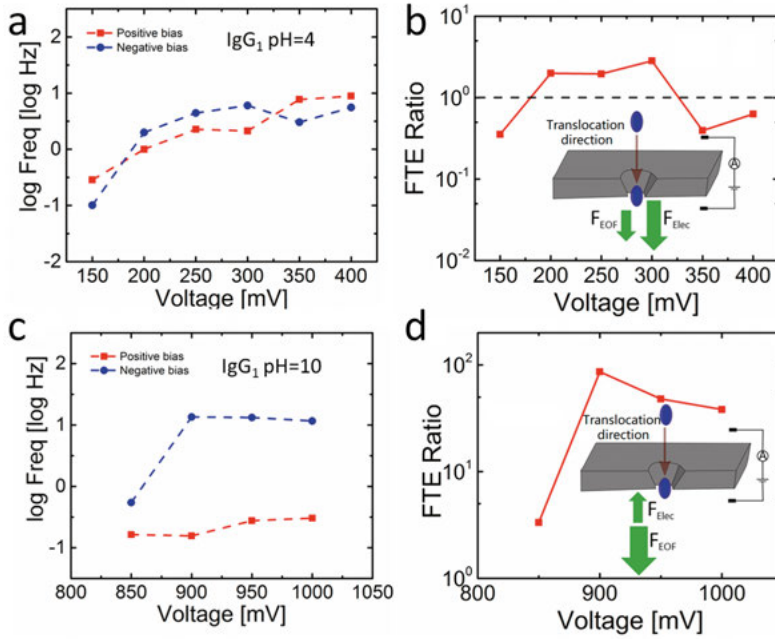


Figure 3.15. Mean FTE and ratio of mean FTE at negative bias to that at positive bias for IgG₁ in a TPPs of $a=25$ nm at pH=4 and 10. (a, c) Mean FTE for IgG₁ versus applied voltage at pH=4 and 10 respectively. (b, d) Ratio of mean FTE for IgG₁ at negative bias to that at positive bias versus applied voltage at pH=4 and 10 respectively. The inset shows the direction of the F_{elec} and F_{EOF} relative to the translocation direction. Larger arrow indicates higher strength.

Overall, the results of the experiments performed at pH=4 and pH=10 show additional features reflecting the complicated interplay among the different forces: electrophoretic force, electroosmotic force, interactive force with the nanopore sidewall, *etc.* All the experimental factors, such as pH, surface charge, viscosity, bias voltage, different forces, *etc.*, are highly coupled one another, and changing a single factor can largely modulate the other.

3.3.4. Merits of analyzing frequency of translocation events

Analyzing FTE, instead of duration and amplitude, requires a relatively narrow bandwidth of the readout electronics, which means a lower background noise (*c.f.* Section 2.4.3). As discussed in Section 3.1.4, an inadequate bandwidth of readout electronics renders distortion of the translocation waveform, namely attenuation in amplitude and dilation in width (Figure 3.5). Typically, the translocation duration of proteins is relatively short, at μ s level [195], [203], compared with that of DNA at ms level. For example, in most of our experimental conditions, the translocation time is dictated by the electroos-

motric flow velocity. As shown in Figure 3.10 (b), the average speed is around 5 nm/s at 200 mV in the passing channel between the nanopore sidewall and the vortex. The translocation length, which corresponds to the crucial length along which electrical signal is generated, is L_{eff} . It is 31.5 nm for an $a=18$ nm TPP. Therefore, the translocation time is estimated conservatively to be 6 μs at 200 mV. To capture a 6 μs -width current pulse, it corresponds to 160 kHz bandwidth for a undistorted duration and amplitude, while it only requires a 10 kHz bandwidth for a correct FTE, since the latter only needs to count the number of pulses instead of needing to restore the whole waveform. However, it is worth noting that in this low-bandwidth configuration, comparing with a pulse width, FTE should be low enough to guarantee a very rare probability of overlapping two neighboring pulses. In our experiment, the maximum of FTE is around 1 kHz, which dispels this concern.

3.4. Autogenic analyte translocation in nanopores

Utilizing ion flux selective channel caused by the surface charge, a nanopore can generate power by introducing a concentration gradient of electrolyte across the pore. However, the output current, as well as the output power, is very weak for a single-pore generator, because of its huge internal resistivity reaching $\text{G}\Omega$ level for sub-10 nm diameter nanopores. According to the published results [204]–[208], the output current of a single pore generator is only at the nA level, and consequently the output power is restricted to the pW-nW level, which is too low to drive commodity electronics such as cell-phones, though it shows a tempting power density at 10^4 W/m^2 level. Therefore, the nanopore generator is only suitable for low current applications. Nanopore-based sensing is one of them, and it ideally matches the power output properties of a nanopore generator.

3.4.1. Mechanism of nanopore generator

As shown schematically in Figure 3.16 (a), a high concentration of electrolyte (KCl for the following discussion) is loaded to the reservoir on the LO side of the nanopore (*i.e.* the upper reservoir), while a low concentration electrolyte is on the opposite side (*i.e.* the lower reservoir). Then a potential difference can be measured between the two pseudo Ag/AgCl electrodes in the two reservoirs. The generated electrical potential is contributed by two sources [205]: the redox potential difference from the two Ag/AgCl electrodes, V_{redox} , and the osmotic potential difference from the electrolyte concentration gradient through the nanopore, V_{osm} . Thus, the open circuit potential is:

$$V_{\text{oc}} = V_{\text{redox}} + V_{\text{osm}} \quad (3-2)$$

V_{redox} is determined by the electrolyte concentration difference and can be described by the Nernstian equation [207]:

$$V_{\text{redox}} = \frac{R_g T}{F} \ln \frac{\gamma_{c_H} c_H}{\gamma_{c_L} c_L} \quad (3-3)$$

where, R_g is the gas constant, F is the Faraday constant, and γ_{c_H} and γ_{c_L} are the activity coefficient for the electrolytes with high and low KCl concentration, respectively. Another source is from the elective diffusion of cations and anions through nanopore, V_{osm} , which can be described as [205]:

$$V_{\text{osm}} = S \frac{R_g T}{F} \ln \left(\frac{\gamma_{c_H} c_H}{\gamma_{c_L} c_L} \right) \quad (3-4)$$

where, S is the ion selectivity [209] (a similar function as t_+ in Section 2.2.1). It is equal to 0 for a pore with zero surface charge, and 1 for an ideal selective pore, which means only cations/anions can pass through. In general, similar to the analysis in rectification of nanopore, selectivity of ion flux will cause an unbalance of diffusive cation and anion fluxes. The accumulation of cations/anions generates a potential difference across the nanopore to compensate for the unbalanced fluxes. This built-in potential is V_{osm} . Analysis details can be found in **Paper VII**.

Figure 3.16 (b) shows the I-V curves of a nanopore generator based on a TPP with a side length $a=18$ nm, by changing the concentration of KCl at the SO side and keeping 1 M KCl at the LO side. As can be seen, by enlarging the concentration difference, the curves increasingly deviate from the origin and move toward the second quadrant. The intercepts of an I-V curve with the x- and y-axes represent the short circuit current, I_{sc} , and open circuit potential, V_{oc} , respectively. In order to explore the power generation characteristics of the nanopore itself, the osmotic potential and current, V_{osm} and I_{osm} , were extracted by, respectively, subtracting V_{redox} and $I_{\text{redox}}=V_{\text{redox}}/R_{\text{in}}$ from the total measured value of V_{oc} and I_{sc} , which are shown in Figure 3.16 (b) at different concentration ratios c_H/c_L . R_{in} represents the total internal resistance of the nanopore system. It can be seen that with the increase of c_H/c_L , both V_{osm} and I_{osm} show clear growth trends in the semi-log scale, in accordance to Eq. 3-4. The ion selectivity at different c_H/c_L is plotted as the inset of Figure 3.16 (c). Furthermore, the maximum output power, P_{out} , and R_{in} are displayed in Figure 3.16 (d).

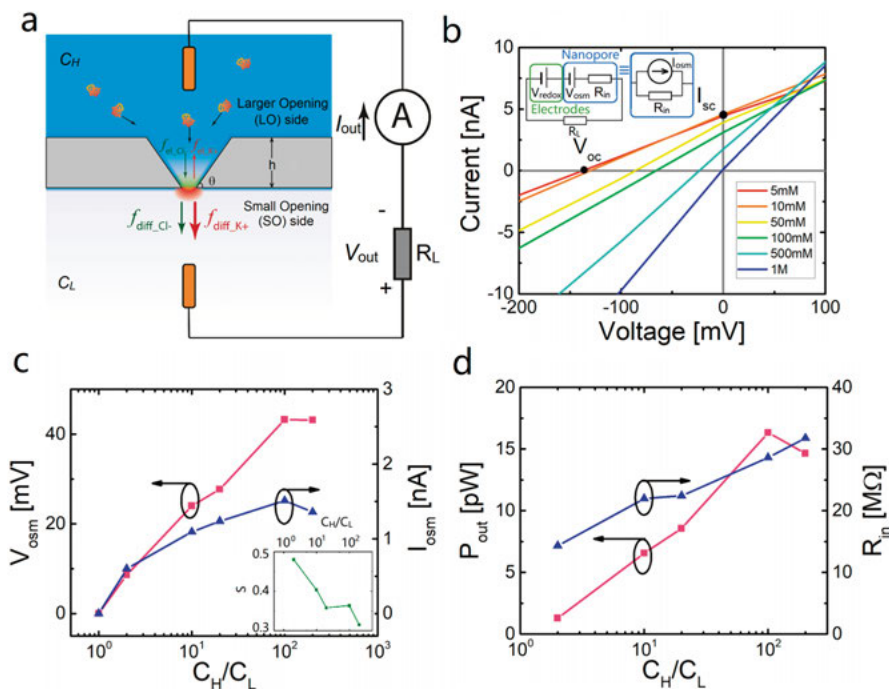


Figure 3.16. Electrical characteristics of the nanopore power generator. (a) Schematic of the nanopore generator. (b) I-V curves of the nanopore generator with several different KCl concentrations on the SO side, while the KCl concentration on the LO side is kept at 1 M. Inset: equivalent circuit of the nanopore generator. The redox potential difference generated from the Ag/AgCl electrodes works as a voltage source (green box) and is connected in series with the osmotic power source (blue box) physically behaving as a current source (Norton equivalent in the right blue box). (c) Variation of osmotic potential and current with C_H/C_L , i.e. KCl concentration ratio. Inset: selectivity of cations and anions at different C_H/C_L . (d) Variation of maximum output power and internal resistance of the nanopore generator with C_H/C_L . Reprinted with permission from [46]. Copyright (2019) Elsevier Ltd.

3.4.2. Electrical characterization of autogenic L-LDH translocation

Protein L-LDH was used to demonstrate the concentration-gradient powered translocation in the $\alpha=18$ nm nanopore. The KCl concentration difference between the SO and LO sides would drive a downward osmotic flow, as well as a downward current, indicated in Figure 3.17 (a). Furthermore, the current generates an electroosmotic flow in the same direction, thereby driving the protein molecules translocating in this direction. When the SO side was filled with electrolyte of the same KCl concentration (500 mM) as that on the LO side, where protein was dispersed, no translocation could be ob-

served as clearly shown in the current traces at different c_H/c_L in Figure 3.17 (a). By reducing the KCl concentration on the SO side, translocation events become both more frequent and with larger blockage amplitude. The statistical results of amplitude and FTE at different concentration ratios c_H/c_L are illustrated as the box charts in Figure 3.17 (b, c), respectively. As expected, the increase in c_H/c_L boosts the driving force for translocation, resulting in a higher FTE (Figure 3.17 (c)). In addition, increasing the concentration difference between c_H and c_L leads to an increase in I_{sc} , hence heightening the amplitude of translocation spikes (Figure 3.17 (b)).

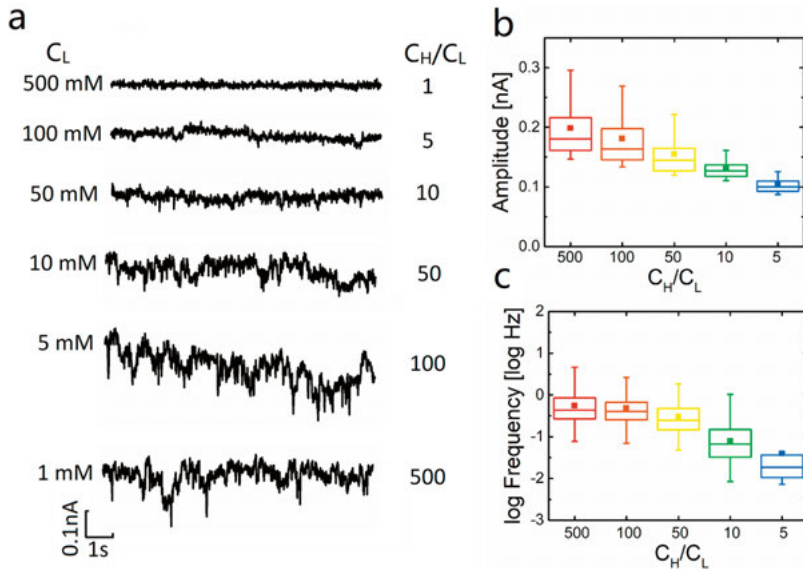


Figure 3.17. Autogenic translocation of L-LDH through a TPP of $a=18$ nm. (a) Ionic current traces of translocation at different KCl concentration on the SO side of the nanopore (left-column numbers). The L-LDH was dispersed in 500 mM KCl electrolyte and filled in the reservoir on the LO side of the nanopore. The resulting ratio c_H/c_L is given as the right-column numbers. (b, c) Box charts showing the statistical results of the variation of translocation amplitude and FTE with c_H/c_L , respectively. Reprinted with permission from [46]. Copyright (2019) Elsevier Ltd.

3.4.3. Optical characterization of autogenic λ -DNA translocation

The autogenic translocation is further demonstrated using λ -DNA. Different from L-LDH, λ -DNA carries a higher density of negative charge and the electrophoretic force appears to dominate the translocation. To facilitate optical detection through an 10×10 nanopore array, the λ -DNA was labeled with fluorescent molecule SyBr Gold and subsequently dispersed in 10 mM KCl electrolyte with 100 pM concentration. It was then added to the SO side

of the nanopore array, while the LO side was filled with 500 mM KCl electrolyte. As discussed above, when the circuit is closed, the ionic current flows from the LO side to the SO side. The strongly negatively charged DNA would, therefore, be driven to pass through the nanopore in the opposite direction. The microscope objective was placed at the LO side. Three sets of frames taken at different time spots of a continuous video clip clearly reveal the λ -DNA translation process in Figure 3.18. In the figure, the bright green dots indicate the λ -DNA molecules. Because of its large length ($\sim 17\ \mu\text{m}$), it took much longer time for the λ -DNA to translocate the nanopores, compared to that of L-LDH. The white arrows mark the newly appeared DNA molecules with reference to the previous frame, while the pink arrows indicate the disappearing DNA molecules in comparison with the next frame.

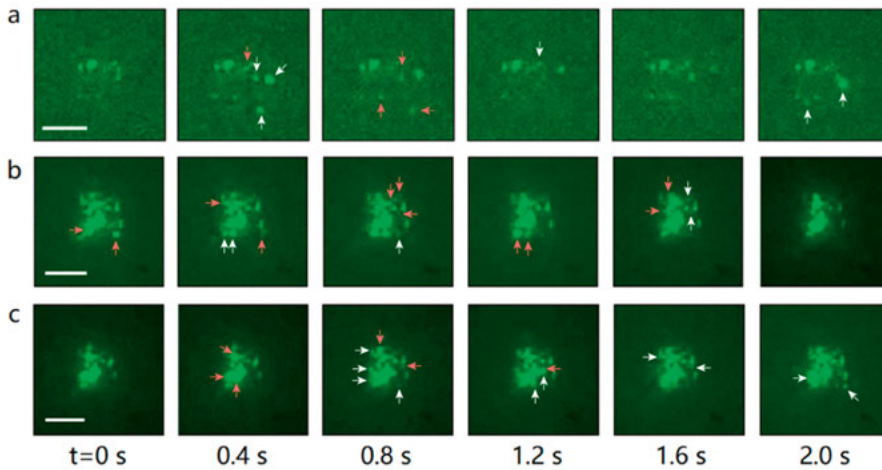


Figure 3.18. Three sets of frames taken at different time spots of a continuous video clip, each for 2 s with a 0.4 s interval showing the autogenic translocation of 100 pM λ -DNA through a 10×10 array of TPPs of $a=10\ \text{nm}$. Time-wise, set (a) precedes (b) and (b) precedes (c). In the frames, the green dots indicate the λ -DNA molecules. By comparing a frame with its adjacent two frames, the white arrows mark the newly appeared DNA compared with the previous frame, while the pink arrows mark the disappeared DNA compared with the next frame. The scale bars in the frames are $10\ \mu\text{m}$. Reprinted with permission from [46]. Copyright (2019) Elsevier Ltd.

L-LDH and λ -DNA represent two distinct categories of analytes: the former is ball-like with low density of charge, while the latter is a long strand and heavily charged. The successfully translocation of both promises that the autogenetic sensing configuration can be applied for most analytes. It does not need any voltage bias module/circuit, which can significantly simplify the readout electronics, hence advancing high-density integration, and even totally omit the module for optical characterization. The marriage of genera-

tor with sensor can, therefore, potentially promote the practicality of high-throughput single-molecule nanopore sensing by the distributed energy harvested by the nanopores themselves.

3.5. Group behavior of nanoparticles transiting multiple nanopores.

In the previous sections, analyte translocation in single nanopore devices is extensively investigated. In order to achieve high-throughput and low-cost parallelized sensing, multiple pore/channel arrays are proposed. However, an individually addressable readout strategy needs to employ separate electrodes, microfluidic cells, and readout electronics for each and every nanopore in the array, to realize capturing and analyzing the events at each and every nanopore independently. This approach poses engineering difficulty on integration density, particularly by the resource-demanding microfluidic cell. To offset this challenge, it is valuable to develop a method to excavate the analyte information from the measured ionic current that represents a superposition of the ionic currents from a multitude of nanopores. In other words, the output ionic current is contributed by all the pores in the array simultaneously, as shown in Figure 3.19.

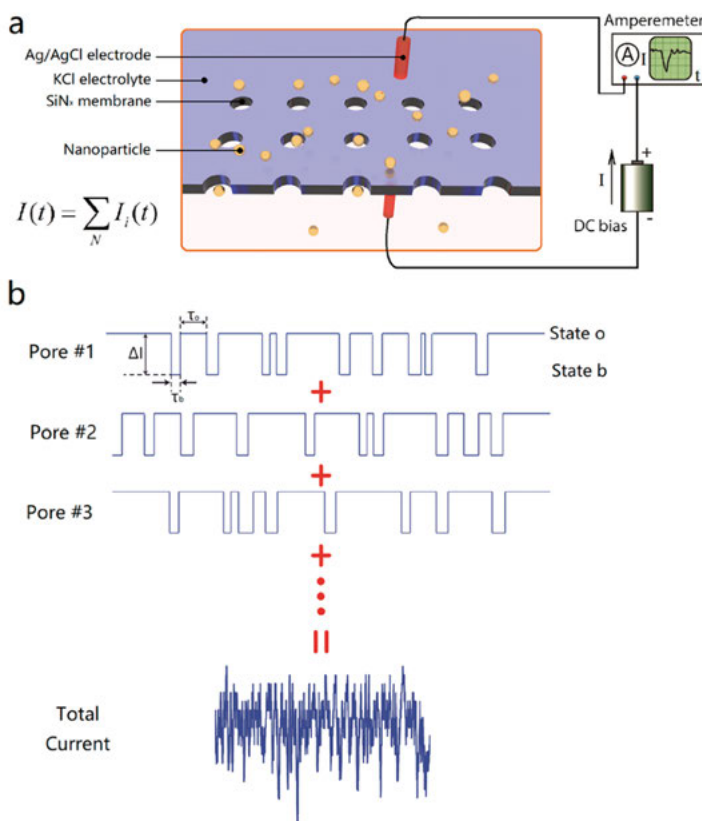


Figure 3.19. Device structure and signal of multiple-nanopore sensor. (a) Schematic device structure of a multiple-nanopore sensor. (b) Schematic illustrations of how sharp and clean ionic currents from three individual pores could evolve to the final output signal. Adapted with permission from [210]. Copyright (2018) American Chemical Society.

3.5.1. Simulation of a multiple pore system

A simulation platform is developed and implemented on MATLAB to explore features of the group translocation behavior. The simulation is based on stochastic process and applied by the following steps. 1) A time step Δt , *i.e.*, sampling rate, is first specified in the simulation. 2) A state of either “open-pore” (o) or “blockage” (b) is randomly generated for each pore at each Δt according to a two-point distribution based on the capture probability P . The capture probability is defined by the average FTE for every pore in the pore array. 3) I_o is assigned to pores in state “o” and $I_b = I_o - \Delta I$ to pores in state “b”, where, ΔI is the current difference between the two states (*i.e.*, the amplitude of blockage). 4) The total current is calculated by summing up the individual currents from all pores. It is worth mentioning that a pore can-

not change to state “o” until lasting for a translocation duration, τ_b , once it is in state “b”. 5) Steps 2-4 are repeated to acquire the total current for the next time point, wherein the current trace is simulated over the time span equal to the inverse of the lowest frequency of noise PSD. 6) Average ionic current, I_{ave} , and its standard deviation (STD), as well as PSD are calculated using the generated current traces in the time domain.

Current traces generated by the translocation of 13 nm-diameter nanoparticles through a nanopore array containing 100 of 20 nm-diameter pores with different capture rate are shown in Figure 3.20 (a). The PSD, I_{ave} , and STD of these current traces are summarized in Figure 3.20 (b, c). In the simulation, the capture rate is fixed at 10 Hz. It can be found that with increasing capture rate, which can be achieved by raising the bias voltage and/or particle concentration in reality, I_{ave} decrease, while the fluctuation of current becomes severe and then is quenched, reflected by the changes of STD and PSD. The mechanism will be discussed later in Section 3.5.3. Changing the number of nanopores, N , in the array impacts the current features obviously, as shown in Figure 3.20 (d-f). By increasing the number of nanopores, both I_{ave} and STD increase.

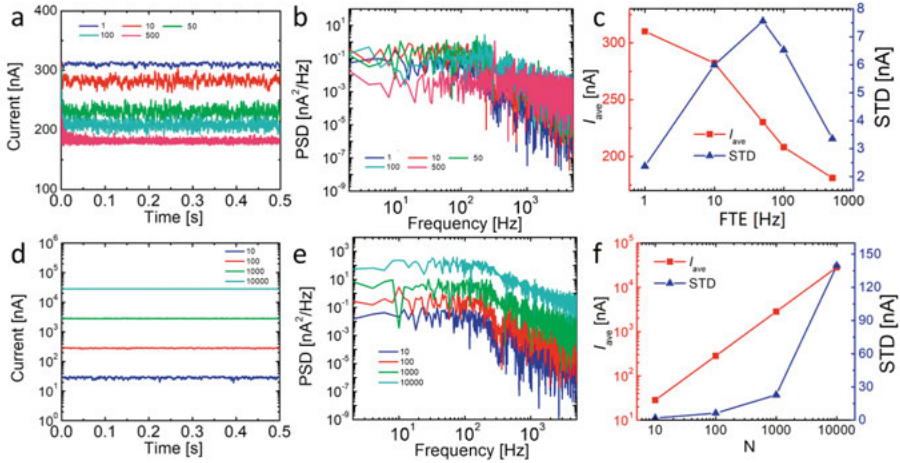


Figure 3.20. Simulation of multiple pore systems. (a) Current traces generated by the translocation of 13 nm-diameter nanoparticles through 100 of 20 nm-diameter nanopores at different capture rates ranging from 1 Hz to 500 Hz. (b) PSD of the current traces from (a), and (c) the corresponding I_{ave} and STD changing with the capture rate. (d) Current traces generated by the translocation of 13 nm-diameter nanoparticles through 20 nm-diameter nanopores for different number of pores ranging from 10 to 10000. The capture rate is set to be 10 Hz. (e) PSD of the current traces from (d), and (f) the corresponding I_{ave} and STD changing with the number of pores. In these simulations, the thickness of the nanopore array is 10 nm, the concentration of electrolyte is 100 mM, the translocation duration τ_b is 3ms, and the bias voltage is 100 mV.

Furthermore, current features of particle transiting multiple pores are compared with those generated from one single big pore of the area equal to the summed area of the multiple pores. Figure 3.21 (a) shows the current traces from one big pore with its area equal to that of N 20 nm-diameter small pores. The size of translocated particles is 13 nm in diameter and the capture rate is set to be $10 \times N$ Hz, for a comparison with N small pore situation (Figure 3.20 (d-f)). The corresponding PSD, I_{ave} and STD are shown in Figure 3.21 (b, c). With increasing pore area, achieved by increasing the number of small pores, I_{ave} increases as expected. However, different from the small pore array configuration, STD of one big pore shows much smaller values and less dependence on N . It directly renders a fast drop of the normalized fluctuation level (STD/I_{ave}) by increasing N , while the small pore array configuration can keep this level at a much higher level, as clearly displayed in Figure 3.21 (d). A higher fluctuation generated by translocation indicates a stronger signal. Besides, small pore arrays possess a larger area for capturing the target particles/molecules, compared with one big pore, which is discussed in detail in the supporting information of **Paper VIII** with the assistance of COMSOL simulation. Therefore, both aforementioned advantages promise a lower detection concentration within shorter detection time for small pore arrays.

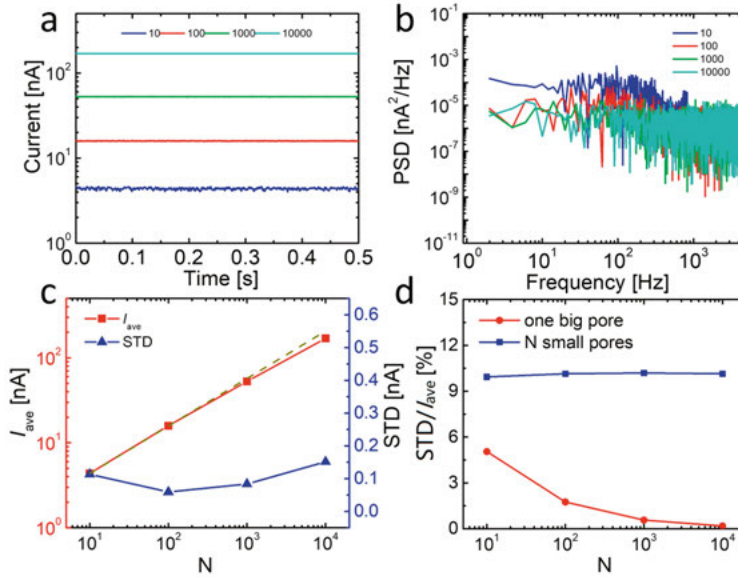


Figure 3.21. Current features for single big pore systems. (a) Current traces generated by the translocation of 13 nm diameter nanoparticles through a big pore with its area equal to the summed area of N small pores each 20 nm in diameter. The capture rate is set to be $10 \times N$ Hz. (b) PSD of the current traces in (a), and (c) the corresponding I_{ave} and STD changing with the big pore area, which is achieved by altering the number of small pores. (d)

Comparison of the normalized signal level between the one big pore case and the N small pore configuration. In these simulations, the thickness of the pore membrane is 10 nm, the concentration of electrolyte is 100 mM, the translocation duration τ_b is 3 ms, and the bias voltage is 100 mV.

3.5.2. Signal properties of group translocation

For the sake of extracting analyte information from the noise-like superimposed current from all the pores in the array, it is necessary to understand the characteristics of the current. As shown in Figure 3.19 (b), in a single pore, the randomly appeared current spikes in the current trace caused by the analyte translocation resemble those of random telegraph noise (RTN). Following the expression of the PSD of RTN, the PSD of the translocation waveform of ionic current can be written as [211]:

$$S_I(f) = \frac{4\Delta I^2}{(\tau_o + \tau_b) \left[\left(\frac{1}{\tau_o} + \frac{1}{\tau_b} \right)^2 + (2\pi f)^2 \right]} \quad (3-5)$$

Where, f is frequency and τ_o and τ_b are mean dwell time in open-pore state and blockage state, respectively. For the multiple pore case, the additivity for a linear system leads to the following relationship:

$$S_N(f) = \sum_{i=1}^N S_i(f) + \sum_{i=1, j=1, i \neq j}^{N, N} S_{i,j}(f) \quad (3-6)$$

where, N is the number of pores, $S_N(f)$ is the total PSD, $S_i(f)$ is PSD of the ionic current from the i^{th} pore, and $S_{i,j}(f)$ is the cross PSD of ionic current from i^{th} and j^{th} pores. $S_{i,j}(f)$ is zero when the translocation events at different pores are independent and there is no correlation among them. This assumption can be guaranteed by keeping large distances among the nanopores in the array with a relatively low concentration of analyte. Furthermore, the average ionic current and its STD can be calculated by:

$$I_{ave} = I_0 \tau_o + (I_0 - \Delta I) \tau_b \quad (3-7)$$

$$STD = \sqrt{\int_0^\infty S_N(f) df} = \frac{\Delta I \sqrt{N \tau_o \tau_b}}{(\tau_o + \tau_b)} \quad (3-8)$$

The open-pore current, I_0 , can be calculated by the resistance model established in Section 2.1 wherein electrolyte concentration, bias voltage, and geometry of nanopore are the only input parameters.

3.5.3. Group translocation behaviors under different conditions

Ionic currents for the translocation of 30 nM SiO₂ nanoparticles of 160 nm in diameter, with a spread of ± 22 nm determined by means of dynamic light scattering, through SiN_x pores of 400 nm in diameter were measured in a KCl solution with the resistivity of 2.8 Ωm and at 200 mV bias voltage. For

this set of experiment, the number of pores N on a device was successively increased from 1 to 10. The distance between adjacent pores in the array was larger than $2\ \mu\text{m}$ in all devices. By increasing the number of pores, current spikes generated by individual translocation events, shown as current traces in Figure 3.22 (a), become increasingly difficult to separate and distinguish. In order to show the details of the waveform, the traces are displayed in the figure after subtracting from their respective average value.

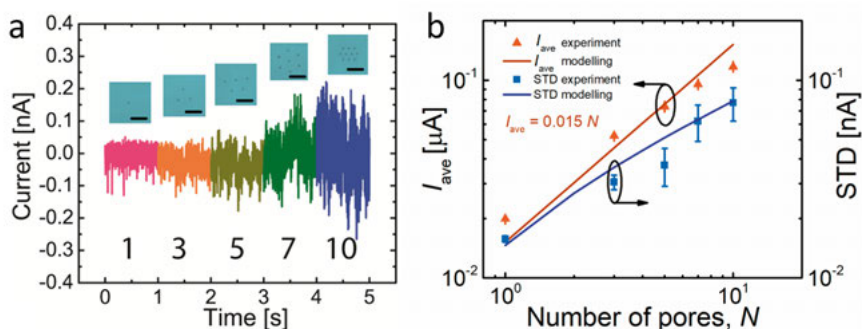


Figure 3.22. Experimental results of group behavior by varying the number of nanopores. (a) Experimentally measured ionic current traces of a single kind of nanoparticles translocating nanopores of increasing number from 1 to 10. Insets: optical microscope images of five multiple-nanopore devices. Scale bars: $5\ \mu\text{m}$. (b) Variation of I_{ave} and STD as a function of number of pores. Dots: experiment, line: model. Error bars: standard deviation of six 1-s-current segments. All the measurements in this figure were carried out with $30\ \text{nM}$ SiO_2 nanoparticles at $200\ \text{mV}$ bias in KCl electrolyte with the resistivity of $2.8\ \Omega\text{m}$. Adapted with permission from [210]. Copyright (2018) American Chemical Society.

The variations of I_{ave} and STD of the translocation ionic current as a function of number of pores are shown in Figure 3.22 (b). For each device with a definite number of pores, six 1-s-current segments are selected arbitrarily from the trace records for the calculation of I_{ave} and STD. As expected by the model (Eq.3-7 and 3-8), an increasing trend for both I_{ave} and STD is observed, which is in agreement with the simulation results (Figure 3.20 (f)).

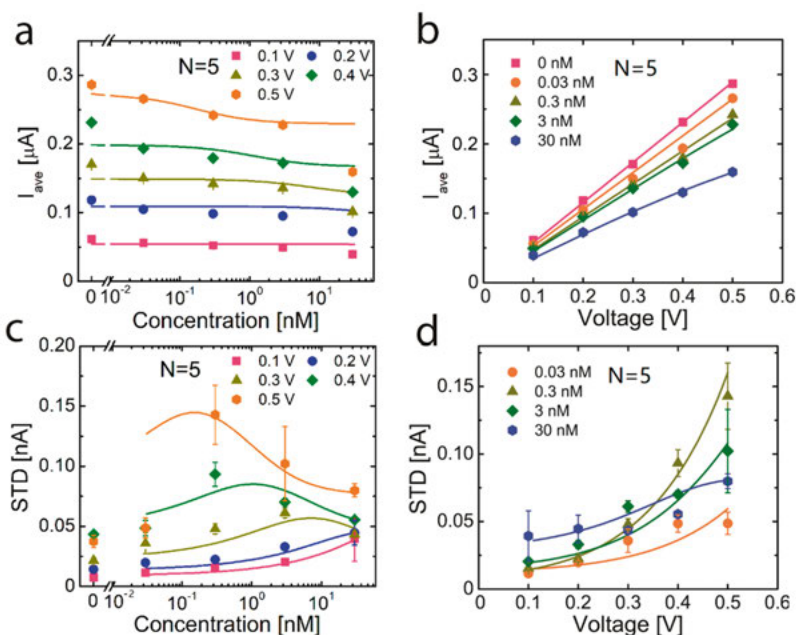


Figure 3.23. Comparison between experiment and model of a five-pore device. (a, c) Variation of I_{ave} and STD with concentration of nanoparticles at different bias voltages. (b, d) Variation of I_{ave} and STD with bias voltage at different concentration of nanoparticles. Dots: experiment, lines: model. Error bars: standard deviation of six 1-s-current segments. Reprinted with permission from [210]. Copyright (2018) American Chemical Society.

In a five-pore device, the translocation currents were recorded for different concentration of SiO₂ nanopore (0.03 nM to 30 nM, i.e., 1.8×10^{10} to 1.8×10^{13} nanoparticles/ml) at various bias voltages (100 mV-500 mV). The changes of I_{ave} and STD by varying the nanoparticle concentration and bias voltage are summarized in Figure 3.23 (a) and (c). It is clear that increasing the concentration of nanoparticles leads to a decrease in I_{ave} . However, STD shows a more complex trend in Figure 3.23 (c), first with an increase with increasing the concentration until it reaches a maximum. It then falls off at higher concentrations. This maximum appears at lower concentrations for higher bias voltages, moving from >30 nM at 100 mV to 0.1 nM at 500 mV. This behavior indicates synergistic effects of voltage and concentration on STD, because both can enhance the capture probability of nanoparticles. When the same group of data is plotted with bias voltage as the x-axis in Figure 3.23 (b, d), both I_{ave} and STD increase monotonously with voltage within the studied interval. The increases coincide well with the trends predicted by the model.

As is known, both bias voltage and concentration of nanoparticles can affect the capture rate. At low concentration, the capture rate increases with

increasing concentration, appearing as a decreasing τ_0 . Yet, τ_0 is still kept longer than τ_b (*c.f.* Figure 3.19 (b)). The relatively shorter τ_0 pushes up the fluctuation level (*i.e.* STD). However, the capture rate can reach a very large value by further increasing the concentration, to the extent that τ_0 becomes shorter than τ_b . In this case, the shorter τ_0 , the lower fluctuation level of the ionic current (*c.f.* Eq. 3-5). Similarly, by increasing the bias voltage, a peak of STD may also appear, which is also observed in the simulation results shown in Figure 3.20 (c) as well as in Figure 4 of **Paper VIII**. In the experiment results (Figure 3.23 (d)), the peak of STD may appear at higher voltage out of our measurement range.

3.5.4. Potential applications

The potential of utilizing the group behavior of multiple nanopores to decipher the translocation properties is further explored for several application scenarios. Table 3.1 summarizes qualitatively the influence of conceivable experimental parameters, which can be controlled and tuned in real measurement, on the output information of translocation. It demonstrates the capability of multiple-nanopore devices to gauge the translocation by numerous nanoparticles of distinct properties.

Table 3.1. Influence of experimental conditions on translocation parameters; Electric field E , translocation speed v , event frequency FTE , open-pore current I_0 , amplitude of current blockage ΔI , pore resistance R , average ionic current I_{ave} , and standard deviation of ionic current STD . (Y: “yes”; N: “no”)

	E	v	FTE	I_0	ΔI	R	I_{ave}	STD
Bias voltage	Y	Y	Y	Y	Y	Y	Y	Y
Pore diameter	Y	Y	Y	Y	Y	Y	Y	Y
Pore thickness	Y	Y	Y	Y	Y	Y	Y	Y
Salt concentration	N	N	N	Y	Y	Y	Y	Y
Electrolyte viscosity	N	Y	Y	N	N	N	Y	Y
Particle diameter	N	Y	Y	N	Y	N	Y	Y
Particle concentration	N	N	Y	N	N	N	Y	Y
pH	N	Y	Y	Y	Y	Y	Y	Y

In dispersions or mixtures of two kinds of nanoparticles of distinct diameters with the total concentration kept constant, I_{ave} and STD will also change uniquely according to the amount ratio of the two nanoparticles. The experimental results of I_{ave} and STD are shown in Figure 3.24 (a) for various mixtures of SiO_2 nanoparticles of 20 ± 2 nm and 160 ± 22 nm in diameter translocating a five-pore device. The continuous lines in the figure display the corresponding simulation results, which coincide with the experimental data very well. An almost linear increase in I_{ave} is observed when varying the

ratio of these two kinds of nanoparticles from 100% 160 nm diameter ($C_{NP1}/(C_{NP1}+C_{NP2})=0$) to 100% 20 nm diameter ($C_{NP1}/(C_{NP1}+C_{NP2})=1$). In contrast, STD displays a bell shape with a maximum around the 50-50 mixture corresponding to the maximum chaos or current fluctuation.

By analyzing the details of I_{ave} and STD, the concentration of nanoparticles can be inferred. Another important parameter for nanoparticles is their diameter. Theoretically, two variables can be uniquely determined by two independent input equations. Similarly, if the experimental conditions, such as diameter and thickness of nanopore, number of nanopores, salt concentration, bias voltage, *etc.*, are well controlled, the diameter and concentration of nanoparticles can be uniquely determined by scrutinizing I_{ave} and STD of ionic current during translocation. As shown in Figure 3.24 (b), a set of calibration curves can be acquired from the model and simulation, as well as from experiment, and the measured I_{ave} and STD can be pinpointed in these calibration curves thereby yielding the diameter and concentration of the nanoparticles.

More information about the nanoparticle samples can be extracted from a series of measurements to yield I_{ave} and STD at, *e.g.*, various bias voltages, diameters of nanopores, numbers of nanopores, *etc.* However, the output is often not a single point but a curve that one can use to assess the nanoparticle samples. For example, I_{ave} and STD show opposite trends in Figure 3.24 (c) by varying the number ratio of two distinct sizes of nanopores. A deeper excavation of group behavior may give us more advanced information and need to be further developed.

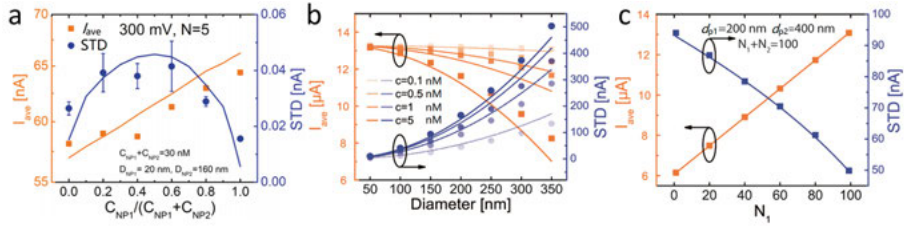


Figure 3.24. Potential applications of multiple nanopore devices. (a) Experiment and simulation of I_{ave} and STD for translocation of mixture nanoparticles. Comparisons between experiment (dots) and simulation (lines) for the changes of I_{ave} and STD of a five-pore device, by varying the mixing ratio of type 1 SiO₂ nanoparticles (NP1, 20 nm in diameter) and type 2 SiO₂ nanoparticles (NP2, 160 nm in diameter). The total concentration of the mixture is fixed to 30 nM. The simulation and measurement were implemented at 300 mV bias and in KCl buffer with the resistivity of 6.2 Ωm. Error bars: standard deviation of six I-s-current segments. A normalization factor was necessary to bring the simulation results to the same range of the experimental data. (b) Variation of I_{ave} and STD as a function of pore diameter for several concentrations of nanoparticles from 0.1 to 5 nM. Dots: simulation, lines:

model. (c) Variation of I_{ave} and STD as a function of the fraction of type 1 nanopores (N_1 with $d_{p1}=200$ nm) along with type 2 nanopores (N_2 with $d_{p2}=400$ nm), with the total number kept at 100. In (c), 0.5 nM of nanoparticles of 160 nm in diameter, 100 mM KCl and 300 mV bias voltage. Adapted with permission from [210]. Copyright (2018) American Chemical Society.

3.6. Summary of this chapter

This chapter presents several key applications of nanopore sensing based on solid-state nanopores. Through successful demonstrations of analyte translocation, including DNA, proteins, and nanoparticles, a low noise electrical characterization platform for nanopore devices is well established. The ionic current signal acquisition guideline and data processing flow have been standardized. The modulation of the electroosmotic vortex in TPP and its effects on protein translocation dynamics are extensively excavated. The autogenic translocation of DNA and proteins driven by the power generated by the electrolyte concentration gradient is preliminary attempted. Furthermore, extending to the multiple pore system, the group translocation behavior of nanoparticles has been comprehensively studied. Various application scenarios, different analyte categories, and divergent device structures accompanying with flexible configurations sufficiently embody the huge potential of the nanopore to be a versatile sensor.

4. Summary and outlook

Grasping the physical picture of nanopore mechanisms, various kinds of sensing by solid-state nanopores have been implemented. The fascinating journey of exploring solid-state nanopore has to be paused here. In this journey, in-depth insights of nanopore mechanisms have been excavated with the assistance of a large amount of numerical simulations and condensed into models. Many systematic experiments on nanopore sensing have been implemented and corresponding applications have been demonstrated. Overall, the theoretical and experimental studies support each other and present a comprehensive picture of solid-state nanopore sensors synergistically. In detail, the major findings of this thesis can be wrapped up as follows:

1. The effective transport length L_{eff} of nanopores, is defined to gauge the extent of high-field-region, *i.e.*, electrical sensitive region, by considering the electric field distribution in a nanopore. It is a feature parameter not only to estimate the open-pore resistance, but also to quantify the spatial resolution of sensing. Based on L_{eff} , a resistance model is established to accurately extract size information of nanopores with arbitrary shape from simple resistance measurements. Furthermore, it acts as a guidance to novel nanopore structure design, stimulating the birth of zero-depth interfacial nanopore.

2. An analytical model is built to describe the ionic current rectification properties of geometrically asymmetrical nanopores, by following the logical causality of key physical factors: charge present on the pore sidewalls causing selectivity of ion fluxes through the pore, the selectivity inducing enrichment-depletion of ions around the pore, the established ion concentration gradient rendering electric field redistribution in the pore, and consequently different conductance appearing at positive and negative biases.

3. Noise origins in solid-state nanopores are systematically clarified. It contains the flicker noise from both surface conductance and bulk conductance of nanopore, $1/f$ -shape noise from Ag/AgCl electrodes, thermal noise from nanopore, dielectric noise from the parasitic capacitance of nanopore membrane, and capacitive noise from readout electronics. At low frequency range, flicker noise from surface conductance in EDL dominates in small size nanopores and low concentration of electrolytes.

4. A simple nano-disk model is developed to analyze the signal generated by the translocation of ssDNA. The signal margin can be predicted for various sizes of nanopores. Combining with its noise characteristics, the re-

quirements on background noise, as well as on the bandwidth of readout electronics are conclusively discussed.

5. A stable nanopore characterization platform is successfully constructed, mainly concerning noise shielding, bandwidth selection, and data sampling issues. With this platform, various configurations of measurements can be implemented, including the open-pore characteristics, noise properties, and translocation behaviors of DNA, proteins, and nanoparticles. In addition, a follow-up data processing procedure is developed and standardized.

6. Electroosmotic vortex in TPP is firstly discovered in simulation results and its existence is further supported by the results of a series of protein translocation experiments. The size and intensity of the vortex can be modulated by many experimentally controllable parameters, such as bias voltage, electrolyte concentration, pH, nanopore shape, *etc.* Involving vortex-analyte interaction offers extra chances to capture features of analytes, which could be hidden in the conventional measurement configurations. These features can be potentially used to recognize various analytes.

7. The autogenic translocation of proteins and DNA is demonstrated by utilizing the power generated by the concentration gradient of electrolyte across a nanopore. This demonstration gives a chance to simplify the readout electronics pursuing a high integration density, since the voltage biasing module can be omitted. It especially benefits optical characterization, in which the electronics can be totally avoided.

8. The properties of the ionic current generated by the random translocation of nanoparticles through an array of nanopores simultaneously are extensively studied by model, simulation, and experiment. The group translocation configuration is a new approach of nanopore sensing. With the assistance of a phenomenological model based on the PSD of RTN, the features of current signal, *i.e.*, average of current, standard deviation, and PSD, are connected to analyte properties, such as size and concentration. Group behavior based nanopore array devices have, furthermore, shown their ability to discriminate two kinds of nanoparticles with distinct sizes in mixture.

In this firmly constructed framework of solid-state nanopore sensing, more bricks can be and will be laid in the next phase of the nanopore project:

1. The first priority issue is to stabilize measurement and enhance repeatability, which could be achieved by appropriate surface functionalization. We have, as an example, recently initiated studies on coating lipid bilayer on the surface of SiN_x cylinder nanopores and silicon TPPs. From the preliminary optical observations, the lipid bilayer can efficiently prohibit the non-specific adsorption of analytes and other contaminations, and smoothen the translocation of DNA. More efforts are needed to optimize the functionalization process for a stable, continuous, and uniform lipid bilayer.

2. Background noise is an unavoidable topic in all kinds of sensing processes. Pursuing higher spatiotemporal resolutions sets more strict demands on the noise level. Therefore, suppressing noise is equally significant to am-

plifying signals. Since the final apparent noise is the superposition of all the noise sources in the system, including device, readout electronics, and environmental interference, noise mitigation should be considered from all aspects through an organic and collective approach.

3. Signal processing algorithm needs substantially improving, especially for the recognition and extraction of translocation events. Translocation events are identified according to their amplitude referring to a threshold in nowadays commonly used methods. However, the determination of this threshold does not have a unified objective principle. Besides, other complicated practical factors may also challenge the robustness of the algorithm, such as drift and fluctuation of current baseline, modulation of translocation waveform by the frequency response characteristics of the amplifier, nonstationary noise behavior, interference of adjacent translocation events, *etc.* Therefore, a standard robust signal processing method is still desired.

4. Novel advanced translocation data analysis methods have shown many promising applications in nanopore sensing, such as neural network-based machine learning algorithms. Prior to the wide use of these powerful methods, a prerequisite should be well addressed that is a stable translocation behavior as well as repeatable results. Otherwise, these analysis methods are always futile. In addition, special development of these methods is necessary to adapt to the properties of nanopore translocation signals.

5. As a phenomenological approach, electrical method to monitor the translocation has its limitations. For example, it cannot accurately correlate the current changes to the translocation morphology in microscale. Therefore, combination of multiple detection methods is a possible way to break the limitations, since different methods provide their own perspectives. The whole picture is to be restored by connecting the snapshots from different detection methods. Combination of electrical readout with optical fluorescent observation has been developed by others and it seems to be a feasible scheme [212], [213].

Sammanfattning på Svenska

Nanoporbaserad detektering har allmänt studerats för ett stort antal tillämpningar, inklusive DNA-sekvensering, proteinprofilering, metabolitmolekyler och jon-detektion. Nanoportekniken erbjuder en teknisk lösning utan motstycke för att tillgodose kraven på precisionsmedicin vid snabb och billig biomolekylanalys ute på fältet. I allmänhet kategoriseras nanoporer i två familjer: nanopor i fast material och biologisk nanopor. Den förstnämnda skapas i ett membran av SiN_x , SiO_2 , kisel, grafen, MoS_2 , *etc.*, medan den senare består av naturliga proteinjonkanaler i cellmembran. De biologiska porerna har oersättliga fördelar, såsom stabila geometriska och fysikalisk-kemiska egenskaper och möjlighet att funktionaliseras på atomär nivå. Däremot är nanoporerna i fasta material mekaniskt robusta och tillverkningen är kompatibel med processerna som används vid traditionel halvledartillverkning vilket kan bana väg för deras storskaliga tillverkning och syntes i små dimensioner med hjälp av standardmässig styrelektronik. Utmaningar som emellertid kvarstår för nanoporerna i fasta material, inkluderar dålig stabilitet, låg repeterbarhet och relativt högt bakgrundsbrus. Denna avhandling undersöker nanoporer i fasta material från grundläggande fysiska mekanismer till mångsidiga applikationer genom en balans mellan teori och experiment. Fördjupade insikter för mekanismer hos nanoporer har tagits fram och använts för att utforma modeller med hjälp av stora mängder numeriska simuleringar. Många systematiska experiment på nanopordetektering har utförts och motsvarande tillämpningar har påvisats. Sammantaget stöder de teoretiska och experimentella studierna varandra och presenterar synergistiskt en övergripande bild av sensorer baserade på nanoporer i fasta material. De viktigaste resultaten i denna avhandling kan sammanfattas enligt följande:

Avhandlingen börjar med teoretiska modeller av nanoporer och etablerar ett omfattande ramverk för att strukturera huvudsakliga fysiska processer involverade i nanopordetektering.

1. Resistensen hos den öppna porens tillstånd studeras baserat på fördelningen för det elektriska fältet. Den effektiva transportlängden L_{eff} hos nanoporer definieras för att mäta omfattningen av högfältsområdet, d.v.s. det elektriskt känsliga området. Det är en funktionsparameter, inte bara för att uppskatta resistensen hos den öppna poren, utan också för att kvantifiera den rumsliga upplösningen för detektering. Baserat på L_{eff} etableras en modell för resistensen för att noggrant extrahera nanoporstorleken på olika geomet-

riska former utifrån enkla resistensmätningar. Dessutom fungerar det som vägledning till ny design av nanoporstrukturer, vilket stimulerar tillkomsten av nanoporen med noll djup.

2. En analytisk modell är konstruerad för att beskriva jonströmmens likriktande egenskaper hos geometriskt asymmetriska nanoporerna genom att följa de logiska orsakssambanden hos de centrala fysiska faktorerna: laddning närvarande på porens sidoväggar, vilket medför selektivitet av jonflöden genom poren, selektivitetsinducerande anrikningen-utarmningen av joner runt poren, den etablerade jonkoncentrationsgradienten som ger upphov till ny elektrisk fältfördelning i poren, och följaktligen en annan konduktans som uppstår vid positiva och negativa förspänningar.

3. Brusets ursprung hos nanoporer i fasta material identifieras systematiskt. Det innehåller flimmerbruset från både ytkonduktans och bulkkonduktans hos nanoporen, $1/f$ -formbruset från Ag/AgCl-elektrodena, det termiska bruset från nanoporen, det dielektriska bruset från den parasitiska kapacitansen hos nanopormembranet och det kapacitiva bruset från avläsningselektroniken. Vid låga frekvenser dominerar flimmerbruset från ytkonduktansen i elektriska dubbelskikt hos småskaliga nanoporer och vid låg koncentration av elektrolyter.

4. En enkel nanodiskmodell är utvecklad för att analysera signalen som genereras av translokationen av enkelsträngat DNA. Signalnivån kan förutsägas för olika storlekar av nanoporer. Tillsammans med deras brusegenskaper, diskuteras kraven på bakgrundsbrus, liksom på bandbredden för avläsningselektroniken.

Därefter implementeras experiment med nanopordetektion på cylindriska SiN_x -nanoporer och trunkerade pyramidnanoporer i kisel (TPP).

5. En stabil nanoporkarakteriseringsplattform har framgångsrikt konstruerats, huvudsakligen avseende brusavskärmning, bandbreddselektion och datasamlingsproblem. Med denna plattform kan olika konfigurationer för mätningar implementeras, inklusive egenskaperna för de öppna porerna, brusegenskaperna och translokationsbeteenden hos DNA, proteiner och nanopartiklar. Dessutom utvecklas och standardiseras ett förfarande för uppföljande behandling av data.

6. Elektroosmotisk vortex i TPP upptäckes först i simuleringsresultat och dess existens stöds ytterligare av resultaten i en serie experiment med proteintranslokation. Vortexens storlek och intensitet kan moduleras av många experimentellt kontrollerbara parametrar, såsom förspänning, elektrolytkoncentration, pH, nanoporform, *etc.* Beaktande av interaktion mellan vortex-analyt ger en extra möjlighet att tillvarata egenheter hos analyter som kan döljas i konventionella mätkonfigurationer. Dessa egenheter kan potentiellt användas för att känna igen olika analyter.

7. Den autogena translokationen av proteiner och DNA påvisas genom nyttjande av kraften alstrad av koncentrationsgradienten hos elektrolyt över en laddad nanopor. Denna demonstration ger en möjlighet att förenkla avläs-

ningselektroniken genom småskalig tillverkning, eftersom förspänningsmodulen kan utelämnas. Det gynnar särskilt optisk karakterisering, där elektroniken helt kan undvikas.

8. Egenskaperna hos jonströmmen som genereras av den samtidiga slumpmässiga translokationen av nanopartiklar genom en uppsättning nanoporer studeras omfattande med hjälp av en modell, simuleringar och experiment. Konfigurationen med grupptranslokation är en ny metod för nanopor-detektering. Med hjälp av en fenomenologisk modell baserad på effektspektrumdensiteten (PSD) för slumpmässigt telegrafbrus korreleras egenskaperna hos strömsignalen, dvs medelvärdet på strömmen, standardavvikelsen och PSD, till analytegenskaperna, såsom storlek och koncentration. Nanoporuپpsättningar baserade på gruppbeteende har vidare visat sig dugliga att diskriminera mellan två typer av nanopartiklar med olika storleksblandningar.

Olika tillämpningsscenarier, olika analyt och divergerande anordningsstrukturer tillsammans med flexibla konfigurationer pekar tydligt på den enorma potentialen i nanoporer i fasta material som en mångsidig sensor. I detta fast konstruerade ramverk kan, och kommer, fler tegelstenar att läggas i nästa fas av nanoporprojektet:

1. Den första prioritetsfrågan är att stabilisera mätningen och förbättra reproduktibiliteten, vilket kan uppnås genom lämplig ytfunktionalisering. Vi har, som ett exempel, nyligen inlett studier på beläggning av ett lipid-dubbelskikt på ytan av SiN_x -nanoporer och TPP. Från de preliminära optiska observationerna kan lipid-dubbelskiktet effektivt förhindra icke-specifik adsorption av analyt och andra föroreningar och förenkla translokationen av DNA. Ytterligare ansträngningar behövs för att optimera funktionaliseringsprocessen för ett stabilt, kontinuerligt och enhetligt lipid-dubbelskikt.

2. Bakgrundsbrus är ett oundvikligt ämne i alla typer av detekteringsprocesser. Att sträva efter högre spatiotemporala upplösningar ställer striktare krav på brusnivån. Därför är undertryckande av brus lika viktigt som förstärkning av signaler. Eftersom det slutliga bruset är överlagringen av alla brus-källor i systemet, inklusive det från enhet, avläsningselektronik och miljöinterferens, bör brusreducering övervägas ur alla aspekter genom ett organiskt och kollektivt tillvägagångssätt.

3. Signalbehandlingsalgoritmen behöver avsevärd förbättring, speciellt för detektering och extraktion av translokationshändelser. Translokationshändelser identifieras i enlighet med deras amplitud med hänvisning till ett tröskelvärde i allmänt tillgängliga metoder. Fastställandet av detta tröskelvärde har emellertid inte en enhetlig målprincip. Dessutom kan andra komplicerade praktiska faktorer utmana robustheten hos algoritmen, såsom drift och fluktuation av strömmens baslinje, modulering av translokationens vågform av frekvensresponsegenskaperna hos förstärkaren, icke-stationärt brus-beteende, störningar av intilliggande translokationshändelser *etc*. Därför är en standardmässig robust signalbehandlingsmetod fortfarande önskvärd.

4. Nya avancerade analysmetoder för translokationsdata har uppvisat många lovande tillämpningar inom nanopordetektering, såsom neurala nätverksbaserade maskininlärningsalgoritmer. Innan den allmänt utbredda användningen av dessa kraftfulla metoder måste en nödvändig förutsättning beaktas, nämligen ett stabilt translokationsbeteende samt repeterbara resultat. Annars blir dessa analysmetoder alltid fruktlösa. Dessutom är en särskild modifiering av dessa metoder nödvändig för anpassning till egenskaperna hos nanopor-translokationssignalerna.

5. Som ett fenomenologiskt tillvägagångssätt har den elektroniska metoden för övervakning av translokationen sin begränsning. Den kan till exempel inte korrelera små strömförändringar till translokationsmorfologin i mikroskalan. Därför är kombination av flera detekteringsmetoder ett möjligt sätt att gå förbi begränsningarna, eftersom olika metoder tillhandahåller olika perspektiv. Hela bilden återställs genom att koppla ihop ögonblicksbilder från de olika detekteringsmetoderna. Kombination av elektrisk avläsning med optisk fluorescerande observation har utvecklats av andra och det verkar vara en framkomlig väg.

Acknowledgement

*Nun heisse ich euch, mich verlieren und euch finden.
Und erst, wenn ihr mich alle verleugnet habt, will ich euch wiederkehren.*

Friedrich Nietzsche

Von der schenkenden Tugend 3, Also sprach Zarathustra

Since September 2015, four years will have passed, quietly like a dream. Too many things have happened and deposited deeply in my mind. Usually triggered by surroundings, the corresponding clips jump out clearly and vividly. A sound may come from the coffee machine at the Ångström café when a stream of the black liquid hits the bottom of a paper cup. A smell may come from the smoked salmon, when I forked a piece at the Christmas table. A color may come from pinky cloud at the horizon of Uppsala just after the sunset approaching a short summer night. A touch may come from the rough surface of a piece of bark, when I stepped into a forest and put my hand on a huge pine. Sweden gives me too many memories, happiness and sorrows, inspiration and frustration, hopes and disappointments, laughs and tears. I want to firstly thank Sweden, a lovely place that fully fills my memory, enriches my experiences, and holds up my dream. *Amicus Plato, sed magis amica veritas*. In Sweden, the equality is adequately embodied in academia. In front of science, every related opinion is discussible and the judgement is not based on authority but truth. More importantly, Sweden gives me a new angle toward this world, a totally fresh view to see entirely different possibilities, which lifts me from the established opinions up to a higher altitude. Just as Bertrand Russell said, diversity is essential to happiness. Here, diversified attitudes, life styles, values, and cultures stretch my view and broaden my mind. In general, these offer me a deeper introspection, which ignites me to know myself better.

I would like to thank my main supervisor Shi-Li Zhang, who has given me professional supervision on my research and wise orientation on my career planning. Thank you for giving me this opportunity to study in Uppsala University. You are a beacon of my academic life since we met at the first time in 2012. You dispel the darkness on my future road and guide the direction of my future career. When I was in the gloomy moments, you always inspired me which fueled my passions and kept me moving. Thank you so much!

I would like to thank my co-supervisor Zhen Zhang. You have given me tremendous help during my four-year study. I really admire your wisdom, resolute, helpfulness, and geniality. You are my role model and thank you so much for all of these.

I would like to thank Ralph Scheicher for the great support for the theoretical part of my work. You are so erudite and I can always learn a lot from our fruitful discussions. I want to thank Paul Solomon for his assistance with not only the development of physical models but also the construction of characterization platform. I still remember the scenario that we debugged the per-amplifier for the noise characterization equipment. Your rich experiences and deep understanding of signal feedback really impressed me.

Next, I would like to thank my skillful colleagues, friends, and comrades in the nanopore project. Thank you, Shuangshuang Zeng, for offering me various nanopore devices and helping me on measurement platform construction. Without your continuous and silent efforts on development and optimization of the nanopore fabrication process, I even don't have the suitable devices to accomplish the study. Thank you, Shiyu Li, for assisting me with the optical fluorescent characterization. Besides, thank you both for spending wonderful time with me on chat, drinks, and laughs.

Thank Robin Augustine for screening my thesis and giving me useful comments. Thank Tomas Nyberg for translating the summary of my thesis into Swedish.

Thank Jörgen Olsson, Dragos Dancila, and Uwe Zimmermann for involving me into the teaching of two courses: Electronics I and Analog electronics. I feel very happy to work with you during the four years teaching, and I have learnt a lot from you not only about the knowledge in these courses, but also the skills of pedagogy. Thank you, Long Hoang Duc, for fighting alongside with me as the lab assistants of these courses. In addition, Thank you for the beer and chat at many nights in pubs.

I would like to thank my friends and colleagues in this division. It is you who give me hands when I need, in both research work and daily life. Thank you also for spending such fun time with me. Thank you Jie Zhao, Xingxing Xu, Xi Chen, Si Chen, Qitao Hu, Chiao-Wei Tseng, Ngan Pham, Libo Chen, Da Zhang, Man Song, Zhibin Zhang, Lukas Jablonka, Asta Makaraviciute, Quentin Palomar, Malkolm Hinnemo, Renbin Tong, Yingtao Yu, Yifei Liu, Umut Cindemir, Apurba Dev, Imran Aziz, Syaiful Redzwan, Wei-Chao Chen, Michelle Marie Villamayor, Sven Englund, Carl Häggglund, Tomas Kubart, Tobias Törndahl, *etc.*

I want to thank my friends in Sweden for the great time we spent together and the great moments we witnessed together. Thank you Feiyan Liang, Ruijun Pan, Meiyuan Guo, Yi Ren, Liyang Shi, Mingzhi Jiao, Kai Song, Rui Sun, Lei Tian, Huan Wang, Lu Wu, Shengyang Zhou, Ye Zou, Ishtiaq Hassan Wani, Yuanyuan Han *etc.*

In addition, I want to thank my close friends abroad. Without your selfless support and endless encouragement, I barely can stand the difficulties in my life. Thank you Guoli He, Qiqi Huang, Lu Wang, Geng Zhang, Zhiqiang Sun, Tuo Tie, Peng Huo, Xin Chai, Ruixue Zeng, Youwei Zhang, *etc.* Accompanied by you, I am not fighting lonely.

I want to thank Jie Ren for all of her giving and efforts during these years. Specially, I want to thank Qian Liu for her supporting in my study and caring in my daily life.

At last, I would like to thank my parents, Jun Wen and Lanping Chen, who give me cosmic love, unlimited support, unconditional understanding, and unreserved dedication, as always and lasting for eternity.

Chenyu Wen

文宸宇

2019-06-18, Uppsala

References

- [1] R. W. Barker, 'Is precision medicine the future of healthcare?', *Pers. Med.*, vol. 14, no. 6, pp. 459–461, Nov. 2017.
- [2] C. A. Blau and E. Liakopoulou, 'Can we deconstruct cancer, one patient at a time?', *Trends Genet.*, vol. 29, no. 1, pp. 6–10, Jan. 2013.
- [3] Y.-F. Lu, D. B. Goldstein, M. Angrist, and G. Cavalleri, 'Personalized Medicine and Human Genetic Diversity', *Cold Spring Harb. Perspect. Med.*, vol. 4, no. 9, pp. a008581–a008581, Sep. 2014.
- [4] M. Twilt, 'Precision Medicine: The new era in medicine', *EBioMedicine*, vol. 4, pp. 24–25, Feb. 2016.
- [5] S. H. Katsanis and N. Katsanis, 'Molecular genetic testing and the future of clinical genomics', *Nat. Rev. Genet.*, vol. 14, no. 6, pp. 415–426, Jun. 2013.
- [6] N. Harbeck, K. Sotlar, R. Wuerstlein, and S. Doisneau-Sixou, 'Molecular and protein markers for clinical decision making in breast cancer: Today and tomorrow', *Cancer Treat. Rev.*, vol. 40, no. 3, pp. 434–444, Apr. 2014.
- [7] I. I. Arzimanoglou and F. Gilbert, 'Genetics and DNA technology', *Curr. Opin. Obstet. Gynecol.*, vol. 6, pp. 445–452, 1994.
- [8] 'Technology Assessment No. 11: Genetics and Molecular Diagnostic Testing', *Obstet. Gynecol.*, vol. 123, no. 2, PART 1, pp. 394–413, Feb. 2014.
- [9] W. Rogowski, 'Current impact of gene technology on healthcare', *Health Policy*, vol. 80, no. 2, pp. 340–357, Feb. 2007.
- [10] K. V. Voelkerding, S. A. Dames, and J. D. Durtschi, 'Next-Generation Sequencing: From Basic Research to Diagnostics', *Clin. Chem.*, vol. 55, no. 4, pp. 641–658, Apr. 2009.
- [11] E. Y. Chan, 'Advances in sequencing technology', *Mutat. Res. Mol. Mech. Mutagen.*, vol. 573, no. 1–2, pp. 13–40, Jun. 2005.
- [12] L. Restrepo-Pérez, C. Joo, and C. Dekker, 'Paving the way to single-molecule protein sequencing', *Nat. Nanotechnol.*, vol. 13, no. 9, pp. 786–796, Sep. 2018.
- [13] B. Iqbal and A. Buch, 'Hormone receptor (ER, PR, HER2/neu) status and proliferation index marker (Ki-67) in breast cancers: Their onco-pathological correlation, shortcomings and future trends', *Med. J. Dr Patil Univ.*, vol. 9, no. 6, p. 674, 2016.
- [14] T. K. Chaudhuri and S. Paul, 'Protein-misfolding diseases and chaperone-based therapeutic approaches', *FEBS J.*, vol. 273, no. 7, pp. 1331–1349, Apr. 2006.
- [15] E. M. Phizicky and S. Fields, 'Protein-protein interactions: methods for detection and analysis', *Microbiol. Rev.*, vol. 59, no. 1, pp. 94–123, Mar. 1995.
- [16] H. Zhu and M. Snyder, 'Protein chip technology', *Curr. Opin. Chem. Biol.*, vol. 7, no. 1, pp. 55–63, Feb. 2003.
- [17] D. A. Triplett, 'Antiphospholipid-protein antibodies: laboratory detection and clinical relevance', *Thromb. Res.*, vol. 78, no. 1, pp. 1–31, Apr. 1995.

- [18] D. M. Bollag, M. D. Rozycki, and S. J. Edelstein, *Protein methods*, 2nd ed. New York: Wiley-Liss, 1996.
- [19] S. Song, Y. Qin, Y. He, Q. Huang, C. Fan, and H.-Y. Chen, 'Functional nanoprobe for ultrasensitive detection of biomolecules', *Chem. Soc. Rev.*, vol. 39, no. 11, p. 4234, 2010.
- [20] W. Gao *et al.*, 'Fully integrated wearable sensor arrays for multiplexed in situ perspiration analysis', *Nature*, vol. 529, no. 7587, pp. 509–514, Jan. 2016.
- [21] J. Kim, A. S. Campbell, and J. Wang, 'Wearable non-invasive epidermal glucose sensors: A review', *Talanta*, vol. 177, pp. 163–170, Jan. 2018.
- [22] P. A. Raymundo-Pereira *et al.*, 'Sensitive detection of estriol hormone in creek water using a sensor platform based on carbon black and silver nanoparticles', *Talanta*, vol. 174, pp. 652–659, Nov. 2017.
- [23] *Electrochemical Sensors, Biosensors and their Biomedical Applications*. Elsevier, 2008.
- [24] M. Strianese, M. Staiano, G. Ruggiero, T. Labella, C. Pellecchia, and S. D'Auria, 'Fluorescence-Based Biosensors', in *Spectroscopic Methods of Analysis*, vol. 875, W. M. Bujalowski, Ed. Totowa, NJ: Humana Press, 2012, pp. 193–216.
- [25] P. Bergveld, 'Thirty years of ISFETOLOGY', *Sens. Actuators B Chem.*, vol. 88, no. 1, pp. 1–20, Jan. 2003.
- [26] R. B. M. Aggio *et al.*, 'The use of a gas chromatography-sensor system combined with advanced statistical methods, towards the diagnosis of urological malignancies', *J. Breath Res.*, vol. 10, no. 1, p. 017106, Feb. 2016.
- [27] M. Rhee and M. A. Burns, 'Nanopore sequencing technology: research trends and applications', *Trends Biotechnol.*, vol. 24, no. 12, pp. 580–586, Dec. 2006.
- [28] M. Muthukumar, C. Plesa, and C. Dekker, 'Single-molecule sensing with nanopores', *Phys. Today*, vol. 68, no. 8, pp. 40–46, Aug. 2015.
- [29] W. Shi, A. K. Friedman, and L. A. Baker, 'Nanopore Sensing', *Anal. Chem.*, vol. 89, no. 1, pp. 157–188, Jan. 2017.
- [30] J. J. Kasianowicz, E. Brandin, D. Branton, and D. W. Deamer, 'Characterization of individual polynucleotide molecules using a membrane channel', *Proc. Natl. Acad. Sci.*, vol. 93, no. 24, pp. 13770–13773, Nov. 1996.
- [31] I. M. Derrington *et al.*, 'Nanopore DNA sequencing with MspA', *Proc. Natl. Acad. Sci.*, vol. 107, no. 37, pp. 16060–16065, Sep. 2010.
- [32] S. Wang, F. Haque, P. G. Rychahou, B. M. Evers, and P. Guo, 'Engineered Nanopore of Phi29 DNA-Packaging Motor for Real-Time Detection of Single Colon Cancer Specific Antibody in Serum', *ACS Nano*, vol. 7, no. 11, pp. 9814–9822, Nov. 2013.
- [33] C. Cao, Y.-L. Ying, Z.-L. Hu, D.-F. Liao, H. Tian, and Y.-T. Long, 'Discrimination of oligonucleotides of different lengths with a wild-type aerolysin nanopore', *Nat. Nanotechnol.*, vol. 11, no. 8, pp. 713–718, Aug. 2016.
- [34] A. Biesemans, M. Soskine, and G. Maglia, 'A Protein Rotaxane Controls the Translocation of Proteins Across a ClyA Nanopore', *Nano Lett.*, vol. 15, no. 9, pp. 6076–6081, Sep. 2015.
- [35] M. Fahie, C. Chisholm, and M. Chen, 'Resolved Single-Molecule Detection of Individual Species within a Mixture of anti-Biotin Antibodies Using an Engineered Monomeric Nanopore', *ACS Nano*, vol. 9, no. 2, pp. 1089–1098, Feb. 2015.
- [36] J. Li, M. Gershow, D. Stein, E. Brandin, and J. A. Golovchenko, 'DNA molecules and configurations in a solid-state nanopore microscope', *Nat. Mater.*, vol. 2, no. 9, pp. 611–615, Sep. 2003.

- [37] H. Chang, F. Kosari, G. Andreadakis, M. A. Alam, G. Vasmatazis, and R. Bashir, 'DNA-Mediated Fluctuations in Ionic Current through Silicon Oxide Nanopore Channels', *Nano Lett.*, vol. 4, no. 8, pp. 1551–1556, Aug. 2004.
- [38] T. Deng, Y. Wang, Q. Chen, H. Chen, and Z. Liu, 'Massive fabrication of silicon nanopore arrays with tunable shapes', *Appl. Surf. Sci.*, vol. 390, pp. 681–688, Dec. 2016.
- [39] G. F. Schneider *et al.*, 'DNA Translocation through Graphene Nanopores', *Nano Lett.*, vol. 10, no. 8, pp. 3163–3167, Aug. 2010.
- [40] J. Feng *et al.*, 'Identification of single nucleotides in MoS₂ nanopores', *Nat. Nanotechnol.*, vol. 10, no. 12, pp. 1070–1076, Dec. 2015.
- [41] J. Choi, C. C. Lee, and S. Park, 'Scalable fabrication of sub-10 nm polymer nanopores for DNA analysis', *Microsyst. Nanoeng.*, vol. 5, no. 1, p. 12, Dec. 2019.
- [42] J. Li, D. Stein, C. McMullan, D. Branton, M. J. Aziz, and J. A. Golovchenko, 'Ion-beam sculpting at nanometre length scales', *Nature*, vol. 412, no. 6843, pp. 166–169, Jul. 2001.
- [43] A. J. Storm, J. H. Chen, X. S. Ling, H. W. Zandbergen, and C. Dekker, 'Fabrication of solid-state nanopores with single-nanometre precision', *Nat. Mater.*, vol. 2, no. 8, pp. 537–540, Aug. 2003.
- [44] Y. Goto, I. Yanagi, K. Matsui, T. Yokoi, and K. Takeda, 'Integrated solid-state nanopore platform for nanopore fabrication via dielectric breakdown, DNA-speed deceleration and noise reduction', *Sci. Rep.*, vol. 6, no. 1, p. 31324, Nov. 2016.
- [45] J. Feng *et al.*, 'Electrochemical Reaction in Single Layer MoS₂: Nanopores Opened Atom by Atom', *Nano Lett.*, vol. 15, no. 5, pp. 3431–3438, May 2015.
- [46] C. Wen, S. Li, S. Zeng, Z. Zhang, and S.-L. Zhang, 'Autogenic analyte translocation in nanopores', *Nano Energy*, vol. 60, pp. 503–509, Jun. 2019.
- [47] A. R. Hall, A. Scott, D. Rotem, K. K. Mehta, H. Bayley, and C. Dekker, 'Hybrid pore formation by directed insertion of α -haemolysin into solid-state nanopores', *Nat. Nanotechnol.*, vol. 5, no. 12, pp. 874–877, Dec. 2010.
- [48] N. A. W. Bell *et al.*, 'DNA Origami Nanopores', *Nano Lett.*, vol. 12, no. 1, pp. 512–517, Jan. 2012.
- [49] D. Deamer, M. Akeson, and D. Branton, 'Three decades of nanopore sequencing', *Nat. Biotechnol.*, vol. 34, no. 5, pp. 518–524, May 2016.
- [50] M. Jain, I. T. Fiddes, K. H. Miga, H. E. Olsen, B. Paten, and M. Akeson, 'Improved data analysis for the MinION nanopore sequencer', *Nat. Methods*, vol. 12, no. 4, pp. 351–356, Apr. 2015.
- [51] A. H. Laszlo *et al.*, 'Decoding long nanopore sequencing reads of natural DNA', *Nat. Biotechnol.*, vol. 32, no. 8, pp. 829–833, Aug. 2014.
- [52] E. A. Manrao *et al.*, 'Reading DNA at single-nucleotide resolution with a mutant MspA nanopore and phi29 DNA polymerase', *Nat. Biotechnol.*, vol. 30, no. 4, pp. 349–353, Apr. 2012.
- [53] P. B. Stranges *et al.*, 'Design and characterization of a nanopore-coupled polymerase for single-molecule DNA sequencing by synthesis on an electrode array', *Proc. Natl. Acad. Sci.*, vol. 113, no. 44, pp. E6749–E6756, Nov. 2016.
- [54] J. Clarke, H.-C. Wu, L. Jayasinghe, A. Patel, S. Reid, and H. Bayley, 'Continuous base identification for single-molecule nanopore DNA sequencing', *Nat. Nanotechnol.*, vol. 4, no. 4, pp. 265–270, Apr. 2009.

- [55] S. Kumar *et al.*, ‘PEG-Labeled Nucleotides and Nanopore Detection for Single Molecule DNA Sequencing by Synthesis’, *Sci. Rep.*, vol. 2, no. 1, p. 684, Dec. 2012.
- [56] ‘Oxford Nanopore Technology Official website’. [Online]. Available: <https://nanoporetech.com/>.
- [57] E. E. Schadt, S. Turner, and A. Kasarskis, ‘A window into third-generation sequencing’, *Hum. Mol. Genet.*, vol. 19, no. R2, pp. R227–R240, Oct. 2010.
- [58] S. Shokralla, J. L. Spall, J. F. Gibson, and M. Hajibabaei, ‘Next-generation sequencing technologies for environmental DNA research: NEXT-GENERATION SEQUENCING FOR ENVIRONMENTAL DNA’, *Mol. Ecol.*, vol. 21, no. 8, pp. 1794–1805, Apr. 2012.
- [59] H. Bayley, ‘Sequencing single molecules of DNA’, *Curr. Opin. Chem. Biol.*, vol. 10, no. 6, pp. 628–637, Dec. 2006.
- [60] M. O. Pollard, D. Gurdasani, A. J. Mentzer, T. Porter, and M. S. Sandhu, ‘Long reads: their purpose and place’, *Hum. Mol. Genet.*, vol. 27, no. R2, pp. R234–R241, Aug. 2018.
- [61] P. Karau and V. Tabard-Cossa, ‘Capture and Translocation Characteristics of Short Branched DNA Labels in Solid-State Nanopores’, *ACS Sens.*, vol. 3, no. 7, pp. 1308–1315, Jul. 2018.
- [62] H. Yamazaki *et al.*, ‘Label-Free Single-Molecule Thermoscopy Using a Laser-Heated Nanopore’, *Nano Lett.*, vol. 17, no. 11, pp. 7067–7074, Nov. 2017.
- [63] M. Ayub, S. W. Hardwick, B. F. Luisi, and H. Bayley, ‘Nanopore-Based Identification of Individual Nucleotides for Direct RNA Sequencing’, *Nano Lett.*, vol. 13, no. 12, pp. 6144–6150, Dec. 2013.
- [64] J. Riedl, Y. Ding, A. M. Fleming, and C. J. Burrows, ‘Identification of DNA lesions using a third base pair for amplification and nanopore sequencing’, *Nat. Commun.*, vol. 6, no. 1, p. 8807, Dec. 2015.
- [65] J. Shang, Z. Li, L. Liu, D. Xi, and H. Wang, ‘Label-Free Sensing of Human 8-Oxoguanine DNA Glycosylase Activity with a Nanopore’, *ACS Sens.*, vol. 3, no. 2, pp. 512–518, Feb. 2018.
- [66] Y. Wang *et al.*, ‘Nanolock–Nanopore Facilitated Digital Diagnostics of Cancer Driver Mutation in Tumor Tissue’, *ACS Sens.*, vol. 2, no. 7, pp. 975–981, Jul. 2017.
- [67] Q. Li, Y.-L. Ying, S.-C. Liu, Y. Lin, and Y.-T. Long, ‘Detection of Single Proteins with a General Nanopore Sensor’, *ACS Sens.*, p. accsensors.9b00228, Mar. 2019.
- [68] P. Waduge *et al.*, ‘Nanopore-Based Measurements of Protein Size, Fluctuations, and Conformational Changes’, *ACS Nano*, vol. 11, no. 6, pp. 5706–5716, Jun. 2017.
- [69] D. Xi, J. Shang, E. Fan, J. You, S. Zhang, and H. Wang, ‘Nanopore-Based Selective Discrimination of MicroRNAs with Single-Nucleotide Difference Using Locked Nucleic Acid-Modified Probes’, *Anal. Chem.*, vol. 88, no. 21, pp. 10540–10546, Nov. 2016.
- [70] O. K. Zahid, F. Wang, J. A. Ruzicka, E. W. Taylor, and A. R. Hall, ‘Sequence-Specific Recognition of MicroRNAs and Other Short Nucleic Acids with Solid-State Nanopores’, *Nano Lett.*, vol. 16, no. 3, pp. 2033–2039, Mar. 2016.
- [71] M. Wanunu, T. Dadosh, V. Ray, J. Jin, L. McReynolds, and M. Drndić, ‘Rapid electronic detection of probe-specific microRNAs using thin nanopore sensors’, *Nat. Nanotechnol.*, vol. 5, no. 11, pp. 807–814, Nov. 2010.

- [72] A. E. Chavis *et al.*, ‘Single Molecule Nanopore Spectrometry for Peptide Detection’, *ACS Sens.*, vol. 2, no. 9, pp. 1319–1328, Sep. 2017.
- [73] H.-C. Wu, Y. Astier, G. Maglia, E. Mikhailova, and H. Bayley, ‘Protein Nanopores with Covalently Attached Molecular Adapters’, *J. Am. Chem. Soc.*, vol. 129, no. 51, pp. 16142–16148, Dec. 2007.
- [74] S. Borsley and S. L. Cockcroft, ‘In Situ Synthetic Functionalization of a Transmembrane Protein Nanopore’, *ACS Nano*, vol. 12, no. 1, pp. 786–794, Jan. 2018.
- [75] H.-Y. Wang, Z.-Y. Song, H.-S. Zhang, and S.-P. Chen, ‘Single-molecule analysis of lead(II)-binding aptamer conformational changes in an α -hemolysin nanopore, and sensitive detection of lead(II)’, *Microchim. Acta*, vol. 183, no. 3, pp. 1003–1010, Mar. 2016.
- [76] G. M. Roozbahani *et al.*, ‘Peptide-Mediated Nanopore Detection of Uranyl Ions in Aqueous Media’, *ACS Sens.*, vol. 2, no. 5, pp. 703–709, May 2017.
- [77] R. Ren *et al.*, ‘Nanopore extended field-effect transistor for selective single-molecule biosensing’, *Nat. Commun.*, vol. 8, no. 1, p. 586, Dec. 2017.
- [78] R. Wei, V. Gatterdam, R. Wieneke, R. Tampé, and U. Rant, ‘Stochastic sensing of proteins with receptor-modified solid-state nanopores’, *Nat. Nanotechnol.*, vol. 7, no. 4, pp. 257–263, Apr. 2012.
- [79] D. Rotem, L. Jayasinghe, M. Salichou, and H. Bayley, ‘Protein Detection by Nanopores Equipped with Aptamers’, *J. Am. Chem. Soc.*, vol. 134, no. 5, pp. 2781–2787, Feb. 2012.
- [80] T. Z. Butler, M. Pavlenok, I. M. Derrington, M. Niederweis, and J. H. Gundlach, ‘Single-molecule DNA detection with an engineered MspA protein nanopore’, *Proc. Natl. Acad. Sci.*, vol. 105, no. 52, pp. 20647–20652, Dec. 2008.
- [81] G. Maglia, M. R. Restrepo, E. Mikhailova, and H. Bayley, ‘Enhanced translocation of single DNA molecules through α -hemolysin nanopores by manipulation of internal charge’, *Proc. Natl. Acad. Sci.*, vol. 105, no. 50, pp. 19720–19725, Dec. 2008.
- [82] H. Kaur, S. Nandivada, M. C. Acharjee, D. S. McNabb, and J. Li, ‘Estimating RNA Polymerase Protein Binding Sites on λ DNA Using Solid-State Nanopores’, *ACS Sens.*, vol. 4, no. 1, pp. 100–109, Jan. 2019.
- [83] G. Celaya, J. Perales-Calvo, A. Muga, F. Moro, and D. Rodriguez-Larrea, ‘Label-Free, Multiplexed, Single-Molecule Analysis of Protein–DNA Complexes with Nanopores’, *ACS Nano*, vol. 11, no. 6, pp. 5815–5825, Jun. 2017.
- [84] Y. You *et al.*, ‘Measuring Binding Constants of Cucurbituril-Based Host–Guest Interactions at the Single-Molecule Level with Nanopores’, *ACS Sens.*, vol. 4, no. 3, pp. 774–779, Mar. 2019.
- [85] E. C. Yusko *et al.*, ‘Real-time shape approximation and fingerprinting of single proteins using a nanopore’, *Nat. Nanotechnol.*, vol. 12, no. 4, pp. 360–367, May 2017.
- [86] W. Yang *et al.*, ‘Detection of CRISPR-dCas9 on DNA with Solid-State Nanopores’, *Nano Lett.*, vol. 18, no. 10, pp. 6469–6474, Oct. 2018.
- [87] N. A. W. Bell and U. F. Keyser, ‘Digitally encoded DNA nanostructures for multiplexed, single-molecule protein sensing with nanopores’, *Nat. Nanotechnol.*, vol. 11, no. 7, pp. 645–651, Jul. 2016.
- [88] M. Tsutsui *et al.*, ‘Identifying Single Particles in Air Using a 3D-Integrated Solid-State Pore’, *ACS Sens.*, vol. 4, no. 3, pp. 748–755, Mar. 2019.
- [89] G. Goyal, R. Mulero, J. Ali, A. Darvish, and M. J. Kim, ‘Low aspect ratio micropores for single-particle and single-cell analysis: Nanoanalysis’, *ELECTROPHORESIS*, vol. 36, no. 9–10, pp. 1164–1171, May 2015.

- [90] M. Tsutsui, S. Hongo, Y. He, M. Taniguchi, N. Gemma, and T. Kawai, 'Single-Nanoparticle Detection Using a Low-Aspect-Ratio Pore', *ACS Nano*, vol. 6, no. 4, pp. 3499–3505, Apr. 2012.
- [91] Z. Gu, Y.-L. Ying, C. Cao, P. He, and Y.-T. Long, 'Accurate Data Process for Nanopore Analysis', *Anal. Chem.*, vol. 87, no. 2, pp. 907–913, Jan. 2015.
- [92] W. B. Dunbar, 'Comment on Accurate Data Process for Nanopore Analysis', *Anal. Chem.*, vol. 87, no. 20, pp. 10650–10652, Oct. 2015.
- [93] Z. Gu, Y.-L. Ying, C. Cao, P. He, and Y.-T. Long, 'Reply to Comment on Accurate Data Process for Nanopore Analysis', *Anal. Chem.*, vol. 87, no. 20, pp. 10653–10656, Oct. 2015.
- [94] K. Misiunas, N. Ermann, and U. F. Keyser, 'QuipuNet: Convolutional Neural Network for Single-Molecule Nanopore Sensing', *Nano Lett.*, vol. 18, no. 6, pp. 4040–4045, Jun. 2018.
- [95] S. Shekar *et al.*, 'Wavelet Denoising of High-Bandwidth Nanopore and Ion-Channel Signals', *Nano Lett.*, vol. 19, no. 2, pp. 1090–1097, Feb. 2019.
- [96] 'Web of Science'. [Online]. Available: <https://apps.webofknowledge.com>.
- [97] S. Magierowski, Y. Huang, C. Wang, and E. Ghafar-Zadeh, 'Nanopore-CMOS Interfaces for DNA Sequencing', *Biosensors*, vol. 6, no. 3, p. 42, Aug. 2016.
- [98] F. Persson, J. Fritzsche, K. U. Mir, M. Modesti, F. Westerlund, and J. O. Tegenfeldt, 'Lipid-Based Passivation in Nanofluidics', *Nano Lett.*, vol. 12, no. 5, pp. 2260–2265, May 2012.
- [99] V. Tabard-Cossa, D. Trivedi, M. Wiggin, N. N. Jetha, and A. Marziali, 'Noise analysis and reduction in solid-state nanopores', *Nanotechnology*, vol. 18, no. 30, p. 305505, Aug. 2007.
- [100] J. D. Uram, K. Ke, and M. Mayer, 'Noise and Bandwidth of Current Recordings from Submicrometer Pores and Nanopores', *ACS Nano*, vol. 2, no. 5, pp. 857–872, May 2008.
- [101] A. Balan *et al.*, 'Improving Signal-to-Noise Performance for DNA Translocation in Solid-State Nanopores at MHz Bandwidths', *Nano Lett.*, vol. 14, no. 12, pp. 7215–7220, Dec. 2014.
- [102] M. R. Powell, C. Martens, and Z. S. Siwy, 'Asymmetric properties of ion current 1/f noise in conically shaped nanopores', *Chem. Phys.*, vol. 375, no. 2–3, pp. 529–535, Oct. 2010.
- [103] M. Akeson, D. Branton, J. J. Kasianowicz, E. Brandin, and D. W. Deamer, 'Microsecond Time-Scale Discrimination Among Polycytidylic Acid, Polyadenylic Acid, and Polyuridylic Acid as Homopolymers or as Segments Within Single RNA Molecules', *Biophys. J.*, vol. 77, no. 6, pp. 3227–3233, Dec. 1999.
- [104] A. Meller, L. Nivon, E. Brandin, J. Golovchenko, and D. Branton, 'Rapid nanopore discrimination between single polynucleotide molecules', *Proc. Natl. Acad. Sci. U. S. A.*, vol. 97, no. 3, pp. 1079–1084, Feb. 2000.
- [105] G. Menestrina, 'Ionic channels formed by *Staphylococcus aureus* alpha-toxin: Voltage-dependent inhibition by divalent and trivalent cations', *J. Membr. Biol.*, vol. 90, no. 2, pp. 177–190, Jun. 1986.
- [106] S. M. Bezrukov, I. Vodyanoy, R. A. Brutyan, and J. J. Kasianowicz, 'Dynamics and Free Energy of Polymers Partitioning into a Nanoscale Pore', *Macromolecules*, vol. 29, no. 26, pp. 8517–8522, Jan. 1996.
- [107] D. Fologea, M. Gershow, B. Ledden, D. S. McNabb, J. A. Golovchenko, and J. Li, 'Detecting Single Stranded DNA with a Solid State Nanopore', *Nano Lett.*, vol. 5, no. 10, pp. 1905–1909, Oct. 2005.

- [108] M. Gershow and J. A. Golovchenko, ‘Recapturing and trapping single molecules with a solid-state nanopore’, *Nat. Nanotechnol.*, vol. 2, no. 12, pp. 775–779, Dec. 2007.
- [109] L. Liang, J.-W. Shen, Z. Zhang, and Q. Wang, ‘DNA sequencing by two-dimensional materials: As theoretical modeling meets experiments’, *Biosens. Bioelectron.*, vol. 89, pp. 280–292, Mar. 2017.
- [110] B. Luan, ‘Radial dependence of DNA translocation velocity in a solid-state nanopore’, *Microchim. Acta*, vol. 183, no. 3, pp. 995–1002, Mar. 2016.
- [111] Z. Kong *et al.*, ‘Charge-tunable absorption behavior of DNA on graphene’, *J. Mater. Chem. B*, vol. 3, no. 24, pp. 4814–4820, 2015.
- [112] D. B. Wells, M. Belkin, J. Comer, and A. Aksimentiev, ‘Assessing Graphene Nanopores for Sequencing DNA’, *Nano Lett.*, vol. 12, no. 8, pp. 4117–4123, Aug. 2012.
- [113] B. N. Anderson, M. Muthukumar, and A. Meller, ‘pH Tuning of DNA Translocation Time through Organically Functionalized Nanopores’, *ACS Nano*, vol. 7, no. 2, pp. 1408–1414, Feb. 2013.
- [114] D. Fologea, J. Uplinger, B. Thomas, D. S. McNabb, and J. Li, ‘Slowing DNA Translocation in a Solid-State Nanopore’, *Nano Lett.*, vol. 5, no. 9, pp. 1734–1737, Sep. 2005.
- [115] H. Zhang *et al.*, ‘Slowing Down DNA Translocation Through Solid-State Nanopores by Pressure’, *Small*, vol. 9, no. 24, pp. 4112–4117, Dec. 2013.
- [116] N. Giambianco, D. Coglitore, J.-M. Janot, P. E. Coulon, B. Charlot, and S. Balme, ‘Detection of protein aggregate morphology through single antifouling nanopore’, *Sens. Actuators B Chem.*, vol. 260, pp. 736–745, May 2018.
- [117] J. Sha *et al.*, ‘Identification of Spherical and Nonspherical Proteins by a Solid-State Nanopore’, *Anal. Chem.*, vol. 90, no. 23, pp. 13826–13831, Dec. 2018.
- [118] D. S. Talaga and J. Li, ‘Single-Molecule Protein Unfolding in Solid State Nanopores’, *J. Am. Chem. Soc.*, vol. 131, no. 26, pp. 9287–9297, Jul. 2009.
- [119] S. Biswas, W. Song, C. Borges, S. Lindsay, and P. Zhang, ‘Click Addition of a DNA Thread to the N-Termini of Peptides for Their Translocation through Solid-State Nanopores’, *ACS Nano*, vol. 9, no. 10, pp. 9652–9664, Oct. 2015.
- [120] M. Ali, S. Nasir, and W. Ensinger, ‘Bioconjugation-induced ionic current rectification in aptamer-modified single cylindrical nanopores’, *Chem. Commun.*, vol. 51, no. 16, pp. 3454–3457, 2015.
- [121] M. Ali, B. Schiedt, R. Neumann, and W. Ensinger, ‘Biosensing with Functionalized Single Asymmetric Polymer Nanochannels’, *Macromol. Biosci.*, vol. 10, no. 1, pp. 28–32, Jan. 2010.
- [122] C. Wloka *et al.*, ‘Label-Free and Real-Time Detection of Protein Ubiquitination with a Biological Nanopore’, *ACS Nano*, vol. 11, no. 5, pp. 4387–4394, May 2017.
- [123] T. Gilboa *et al.*, ‘Single-Molecule DNA Methylation Quantification Using Electro-optical Sensing in Solid-State Nanopores’, *ACS Nano*, vol. 10, no. 9, pp. 8861–8870, Sep. 2016.
- [124] M. Zhang, C. Ngampeerapong, D. Redin, A. Ahmadian, I. Sychugov, and J. Linnros, ‘Thermophoresis-Controlled Size-Dependent DNA Translocation through an Array of Nanopores’, *ACS Nano*, vol. 12, no. 5, pp. 4574–4582, May 2018.
- [125] C. E. Arcadia, C. C. Reyes, and J. K. Rosenstein, ‘In Situ Nanopore Fabrication and Single-Molecule Sensing with Microscale Liquid Contacts’, *ACS Nano*, vol. 11, no. 5, pp. 4907–4915, May 2017.

- [126] P. Zhou, J. Hou, Y. Yan, and J. Wang, ‘The effect of surfactant adsorption on surface wettability and flow resistance in slit nanopore: A molecular dynamics study’, *J. Colloid Interface Sci.*, vol. 513, pp. 379–388, Mar. 2018.
- [127] S. Balme *et al.*, ‘Influence of Adsorption on Proteins and Amyloid Detection by Silicon Nitride Nanopore’, *Langmuir*, vol. 32, no. 35, pp. 8916–8925, Sep. 2016.
- [128] E. Beamish, H. Kwok, V. Tabard-Cossa, and M. Godin, ‘Fine-tuning the Size and Minimizing the Noise of Solid-state Nanopores’, *J. Vis. Exp.*, no. 80, p. 51081, Oct. 2013.
- [129] D. J. Niedzwiecki and L. Movileanu, ‘Monitoring Protein Adsorption with Solid-state Nanopores’, *J. Vis. Exp.*, no. 58, p. 3560, Dec. 2011.
- [130] D. P. Hoogerheide, S. Garaj, and J. A. Golovchenko, ‘Probing Surface Charge Fluctuations with Solid-State Nanopores’, *Phys. Rev. Lett.*, vol. 102, no. 25, p. 256804, Jun. 2009.
- [131] C. A. Merchant *et al.*, ‘DNA Translocation through Graphene Nanopores’, *Nano Lett.*, vol. 10, no. 8, pp. 2915–2921, Aug. 2010.
- [132] R. M. M. Smeets, N. H. Dekker, and C. Dekker, ‘Low-frequency noise in solid-state nanopores’, *Nanotechnology*, vol. 20, no. 9, p. 095501, Mar. 2009.
- [133] S. J. Heerema, G. F. Schneider, M. Rozemuller, L. Vicarelli, H. W. Zandbergen, and C. Dekker, ‘1/f noise in graphene nanopores’, *Nanotechnology*, vol. 26, no. 7, p. 074001, Feb. 2015.
- [134] A. J. McMullen, J. X. Tang, and D. Stein, ‘Nanopore Measurements of Filamentous Viruses Reveal a Sub-nanometer-Scale Stagnant Fluid Layer’, *ACS Nano*, vol. 11, no. 11, pp. 11669–11677, Nov. 2017.
- [135] J. H. Chaudhry, J. Comer, A. Aksimentiev, and L. N. Olson, ‘A Stabilized Finite Element Method for Modified Poisson-Nernst-Planck Equations to Determine Ion Flow Through a Nanopore’, *Commun. Comput. Phys.*, vol. 15, no. 01, pp. 93–125, Jan. 2014.
- [136] C.-Y. Lin, L.-H. Yeh, J.-P. Hsu, and S. Tseng, ‘Regulating Current Rectification and Nanoparticle Transport Through a Salt Gradient in Bipolar Nanopores’, *Small*, vol. 11, no. 35, pp. 4594–4602, Sep. 2015.
- [137] M. Mao, J. D. Sherwood, and S. Ghosal, ‘Electro-osmotic flow through a nanopore’, *J. Fluid Mech.*, vol. 749, pp. 167–183, Jun. 2014.
- [138] W.-L. Hsu and H. Daiguji, ‘Manipulation of Protein Translocation through Nanopores by Flow Field Control and Application to Nanopore Sensors’, *Anal. Chem.*, vol. 88, no. 18, pp. 9251–9258, Sep. 2016.
- [139] T. Mouterde *et al.*, ‘Molecular streaming and its voltage control in ångström-scale channels’, *Nature*, vol. 567, no. 7746, pp. 87–90, Mar. 2019.
- [140] J. Ma *et al.*, ‘Drastically Reduced Ion Mobility in a Nanopore Due to Enhanced Pairing and Collisions between Dehydrated Ions’, *J. Am. Chem. Soc.*, vol. 141, no. 10, pp. 4264–4272, Mar. 2019.
- [141] A. Meller, ‘Dynamics of polynucleotide transport through nanometre-scale pores’, *J. Phys. Condens. Matter*, vol. 15, no. 17, pp. R581–R607, May 2003.
- [142] V. L. Nosik and E. B. Rudakova, ‘Multilevel description of the DNA molecule translocation in solid-state synthetic nanopores’, *Crystallogr. Rep.*, vol. 61, no. 4, pp. 653–665, Jul. 2016.
- [143] C. Forrey and M. Muthukumar, ‘Langevin dynamics simulations of ds-DNA translocation through synthetic nanopores’, *J. Chem. Phys.*, vol. 127, no. 1, p. 015102, Jul. 2007.
- [144] E. J. Campos and J. Yates, ‘Single molecule characterisation of metal nanoparticles using nanopore-based stochastic detection methods’, *Sens. Actuators B Chem.*, vol. 255, pp. 2032–2049, Feb. 2018.

- [145] J. Wilson, K. Sarthak, W. Si, L. Gao, and A. Aksimentiev, ‘Rapid and Accurate Determination of Nanopore Ionic Current Using a Steric Exclusion Model’, *ACS Sens.*, vol. 4, no. 3, pp. 634–644, Mar. 2019.
- [146] A. T. Carlsen, O. K. Zahid, J. Ruzicka, E. W. Taylor, and A. R. Hall, ‘Interpreting the Conductance Blockades of DNA Translocations through Solid-State Nanopores’, *ACS Nano*, vol. 8, no. 5, pp. 4754–4760, May 2014.
- [147] S. W. Kowalczyk, A. Y. Grosberg, Y. Rabin, and C. Dekker, ‘Modeling the conductance and DNA blockade of solid-state nanopores’, *Nanotechnology*, vol. 22, no. 31, p. 315101, Aug. 2011.
- [148] J. E. Hall, ‘Access resistance of a small circular pore’, *J. Gen. Physiol.*, vol. 66, no. 4, pp. 531–532, Oct. 1975.
- [149] J. Liu *et al.*, ‘Surface Charge Density Determination of Single Conical Nanopores Based on Normalized Ion Current Rectification’, *Langmuir*, vol. 28, no. 2, pp. 1588–1595, Jan. 2012.
- [150] M. J. Kim, M. Wanunu, D. C. Bell, and A. Meller, ‘Rapid Fabrication of Uniformly Sized Nanopores and Nanopore Arrays for Parallel DNA Analysis’, *Adv. Mater.*, vol. 18, no. 23, pp. 3149–3153, Dec. 2006.
- [151] R. Kox, S. Deheryan, C. Chen, N. Arjmandi, L. Lagae, and G. Borghs, ‘Local solid-state modification of nanopore surface charges’, *Nanotechnology*, vol. 21, no. 33, p. 335703, Aug. 2010.
- [152] K. Liu *et al.*, ‘Geometrical Effect in 2D Nanopores’, *Nano Lett.*, vol. 17, no. 7, pp. 4223–4230, Jul. 2017.
- [153] C. M. Frament and J. R. Dwyer, ‘Conductance-Based Determination of Solid-State Nanopore Size and Shape: An Exploration of Performance Limits’, *J. Phys. Chem. C*, vol. 116, no. 44, pp. 23315–23321, Nov. 2012.
- [154] C. Wen, Z. Zhang, and S.-L. Zhang, ‘Physical Model for Rapid and Accurate Determination of Nanopore Size via Conductance Measurement’, *ACS Sens.*, vol. 2, no. 10, pp. 1523–1530, Oct. 2017.
- [155] Y. He, M. Tsutsui, C. Fan, M. Taniguchi, and T. Kawai, ‘Controlling DNA Translocation through Gate Modulation of Nanopore Wall Surface Charges’, *ACS Nano*, vol. 5, no. 7, pp. 5509–5518, Jul. 2011.
- [156] C. Lee, L. Joly, A. Siria, A.-L. Biance, R. Fulcrand, and L. Bocquet, ‘Large Apparent Electric Size of Solid-State Nanopores Due to Spatially Extended Surface Conduction’, *Nano Lett.*, vol. 12, no. 8, pp. 4037–4044, Aug. 2012.
- [157] N. Di Fiori, A. Squires, D. Bar, T. Gilboa, T. D. Moustakas, and A. Meller, ‘Optoelectronic control of surface charge and translocation dynamics in solid-state nanopores’, *Nat. Nanotechnol.*, vol. 8, no. 12, pp. 946–951, Dec. 2013.
- [158] A. P. Ivanov *et al.*, ‘DNA Tunneling Detector Embedded in a Nanopore’, *Nano Lett.*, vol. 11, no. 1, pp. 279–285, Jan. 2011.
- [159] R. M. M. Smeets, U. F. Keyser, D. Krapf, M.-Y. Wu, N. H. Dekker, and C. Dekker, ‘Salt Dependence of Ion Transport and DNA Translocation through Solid-State Nanopores’, *Nano Lett.*, vol. 6, no. 1, pp. 89–95, Jan. 2006.
- [160] M. Kosmulski, ‘The pH dependent surface charging and points of zero charge. VII. Update’, *Adv. Colloid Interface Sci.*, vol. 251, pp. 115–138, Jan. 2018.
- [161] G. Yellen, ‘The voltage-gated potassium channels and their relatives’, *Nature*, vol. 419, no. 6902, pp. 35–42, Sep. 2002.
- [162] E. B. Gonzales, T. Kawate, and E. Gouaux, ‘Pore architecture and ion sites in acid-sensing ion channels and P2X receptors’, *Nature*, vol. 460, no. 7255, pp. 599–604, Jul. 2009.

- [163] W. Guo, Y. Tian, and L. Jiang, ‘Asymmetric Ion Transport through Ion-Channel-Mimetic Solid-State Nanopores’, *Acc. Chem. Res.*, vol. 46, no. 12, pp. 2834–2846, Dec. 2013.
- [164] M. L. Kovarik, K. Zhou, and S. C. Jacobson, ‘Effect of Conical Nanopore Diameter on Ion Current Rectification’, *J. Phys. Chem. B*, vol. 113, no. 49, pp. 15960–15966, Dec. 2009.
- [165] P. Y. Apel, I. V. Blonskaya, O. L. Orelovitch, P. Ramirez, and B. A. Sartowska, ‘Effect of nanopore geometry on ion current rectification’, *Nanotechnology*, vol. 22, no. 17, p. 175302, Apr. 2011.
- [166] Y. He, D. Gillespie, D. Boda, I. Vlassiouk, R. S. Eisenberg, and Z. S. Siwy, ‘Tuning Transport Properties of Nanofluidic Devices with Local Charge Inversion’, *J. Am. Chem. Soc.*, vol. 131, no. 14, pp. 5194–5202, Apr. 2009.
- [167] M. Ali *et al.*, ‘Single Cigar-Shaped Nanopores Functionalized with Amphoteric Amino Acid Chains: Experimental and Theoretical Characterization’, *ACS Nano*, vol. 6, no. 4, pp. 3631–3640, Apr. 2012.
- [168] J. M. Perry, K. Zhou, Z. D. Harms, and S. C. Jacobson, ‘Ion Transport in Nanofluidic Funnel’, *ACS Nano*, vol. 4, no. 7, pp. 3897–3902, Jul. 2010.
- [169] L. Cao, W. Guo, Y. Wang, and L. Jiang, ‘Concentration-Gradient-Dependent Ion Current Rectification in Charged Conical Nanopores’, *Langmuir*, vol. 28, no. 4, pp. 2194–2199, Jan. 2012.
- [170] M. Ali, P. Ramirez, S. Mafé, R. Neumann, and W. Ensinger, ‘A pH-Tunable Nanofluidic Diode with a Broad Range of Rectifying Properties’, *ACS Nano*, vol. 3, no. 3, pp. 603–608, Mar. 2009.
- [171] D. Constantin and Z. S. Siwy, ‘Poisson-Nernst-Planck model of ion current rectification through a nanofluidic diode’, *Phys. Rev. E*, vol. 76, no. 4, p. 041202, Oct. 2007.
- [172] K. Pal Singh and M. Kumar, ‘Effect of surface charge density and electroosmotic flow on ionic current in a bipolar nanopore fluidic diode’, *J. Appl. Phys.*, vol. 110, no. 8, p. 084322, Oct. 2011.
- [173] Y. Ma, J. Guo, L. Jia, and Y. Xie, ‘Entrance Effects Induced Rectified Ionic Transport in a Nanopore/Channel’, *ACS Sens.*, vol. 3, no. 1, pp. 167–173, Jan. 2018.
- [174] K. P. Singh, ‘Ion current rectification influenced by length and location of surface charge in fluidic unipolar conical nanopores’, *Sens. Actuators B Chem.*, vol. 230, pp. 493–500, Jul. 2016.
- [175] J. Cervera, A. Alcaraz, B. Schiedt, R. Neumann, and P. Ramírez, ‘Asymmetric Selectivity of Synthetic Conical Nanopores Probed by Reversal Potential Measurements’, *J. Phys. Chem. C*, vol. 111, no. 33, pp. 12265–12273, Aug. 2007.
- [176] L.-J. Cheng and L. J. Guo, ‘Rectified Ion Transport through Concentration Gradient in Homogeneous Silica Nanochannels’, *Nano Lett.*, vol. 7, no. 10, pp. 3165–3171, Oct. 2007.
- [177] Q. Chen, Y. Wang, T. Deng, and Z. Liu, ‘Fabrication of nanopores and nanoslits with feature sizes down to 5 nm by wet etching method’, *Nanotechnology*, vol. 29, no. 8, p. 085301, Feb. 2018.
- [178] K. J. Freedman, C. W. Ahn, and M. J. Kim, ‘Detection of Long and Short DNA Using Nanopores with Graphitic Polyhedral Edges’, *ACS Nano*, vol. 7, no. 6, pp. 5008–5016, Jun. 2013.
- [179] P. J. Fleming and J. J. Wallace, ‘How not to lie with statistics: the correct way to summarize benchmark results’, *Commun. ACM*, vol. 29, no. 3, pp. 218–221, Mar. 1986.

- [180] A. Kumar, K.-B. Park, H.-M. Kim, and K.-B. Kim, 'Noise and its reduction in graphene based nanopore devices', *Nanotechnology*, vol. 24, no. 49, p. 495503, Dec. 2013.
- [181] Z. Siwy and A. Fulinski, 'Origin of $1/f$ Noise in Membrane Channel Currents', *Phys. Rev. Lett.*, vol. 89, no. 15, p. 158101, Sep. 2002.
- [182] R. M. M. Smeets, U. F. Keyser, M. Y. Wu, N. H. Dekker, and C. Dekker, 'Nanobubbles in Solid-State Nanopores', *Phys. Rev. Lett.*, vol. 97, no. 8, p. 088101, Aug. 2006.
- [183] R. A. Levis and J. L. Rae, 'The use of quartz patch pipettes for low noise single channel recording', *Biophys. J.*, vol. 65, no. 4, pp. 1666–1677, Oct. 1993.
- [184] V. Tabard-Cossa, 'Instrumentation for Low-Noise High-Bandwidth Nanopore Recording', in *Engineered Nanopores for Bioanalytical Applications*, Elsevier, 2013, pp. 59–93.
- [185] C. Wen *et al.*, 'Generalized Noise Study of Solid-State Nanopores at Low Frequencies', *ACS Sens.*, vol. 2, no. 2, pp. 300–307, Feb. 2017.
- [186] K. K. Hung, P. K. Ko, C. Hu, and Y. C. Cheng, 'A unified model for the flicker noise in metal-oxide-semiconductor field-effect transistors', *IEEE Trans. Electron Devices*, vol. 37, no. 3, pp. 654–665, Mar. 1990.
- [187] D. Zhang *et al.*, 'Direct assessment of solid–liquid interface noise in ion sensing using a differential method', *Appl. Phys. Lett.*, vol. 108, no. 15, p. 151603, Apr. 2016.
- [188] R. M. M. Smeets, U. F. Keyser, N. H. Dekker, and C. Dekker, 'Noise in solid-state nanopores', *Proc. Natl. Acad. Sci.*, vol. 105, no. 2, pp. 417–421, Jan. 2008.
- [189] M. Zwolak and M. Di Ventra, 'Electronic Signature of DNA Nucleotides via Transverse Transport', *Nano Lett.*, vol. 5, no. 3, pp. 421–424, Mar. 2005.
- [190] M. Zwolak and M. Di Ventra, 'Colloquium: Physical approaches to DNA sequencing and detection', *Rev. Mod. Phys.*, vol. 80, no. 1, pp. 141–165, Jan. 2008.
- [191] C. Hamai, H. Tanaka, and T. Kawai, 'Extended Structure of DNA Oligomer and Nucleotide Imaging Studied by Scanning Tunneling Microscopy', *J. Phys. Chem. B*, vol. 104, no. 42, pp. 9894–9897, Oct. 2000.
- [192] C. Wen, S. Zeng, Z. Zhang, K. Hjort, R. Scheicher, and S.-L. Zhang, 'On nanopore DNA sequencing by signal and noise analysis of ionic current', *Nanotechnology*, vol. 27, no. 21, p. 215502, May 2016.
- [193] C. Raillon, P. Granjon, M. Graf, L. J. Steinbock, and A. Radenovic, 'Fast and automatic processing of multi-level events in nanopore translocation experiments', *Nanoscale*, vol. 4, no. 16, p. 4916, 2012.
- [194] C. Tasserit, A. Koutsoubas, D. Lairez, G. Zalczer, and M.-C. Clochard, 'Pink Noise of Ionic Conductance through Single Artificial Nanopores Revisited', *Phys. Rev. Lett.*, vol. 105, no. 26, p. 260602, Dec. 2010.
- [195] E. C. Yusko *et al.*, 'Controlling protein translocation through nanopores with bio-inspired fluid walls', *Nat. Nanotechnol.*, vol. 6, no. 4, pp. 253–260, Apr. 2011.
- [196] M. R. Powell, L. Cleary, M. Davenport, K. J. Shea, and Z. S. Siwy, 'Electric-field-induced wetting and dewetting in single hydrophobic nanopores', *Nat. Nanotechnol.*, vol. 6, no. 12, pp. 798–802, Dec. 2011.
- [197] J. L. Trick, C. Song, E. J. Wallace, and M. S. P. Sansom, 'Voltage Gating of a Biomimetic Nanopore: Electrowetting of a Hydrophobic Barrier', *ACS Nano*, vol. 11, no. 2, pp. 1840–1847, Feb. 2017.

- [198] R. Hu *et al.*, ‘Differential Enzyme Flexibility Probed Using Solid-State Nanopores’, *ACS Nano*, vol. 12, no. 5, pp. 4494–4502, May 2018.
- [199] J. Houghtaling *et al.*, ‘Estimation of Shape, Volume, and Dipole Moment of Individual Proteins Freely Transiting a Synthetic Nanopore’, *ACS Nano*, p. acsnano.8b09555, Apr. 2019.
- [200] D. E. Smith, T. T. Perkins, and S. Chu, ‘Dynamical Scaling of DNA Diffusion Coefficients’, *Macromolecules*, vol. 29, no. 4, pp. 1372–1373, Jan. 1996.
- [201] M. Wanunu, ‘Nanopores: A journey towards DNA sequencing’, *Phys. Life Rev.*, vol. 9, no. 2, pp. 125–158, Jun. 2012.
- [202] H. Yamazaki, R. Hu, Q. Zhao, and M. Wanunu, ‘Photothermally Assisted Thinning of Silicon Nitride Membranes for Ultrathin Asymmetric Nanopores’, *ACS Nano*, vol. 12, no. 12, pp. 12472–12481, Dec. 2018.
- [203] J. Larkin, R. Y. Henley, M. Muthukumar, J. K. Rosenstein, and M. Wanunu, ‘High-Bandwidth Protein Analysis Using Solid-State Nanopores’, *Biophys. J.*, vol. 106, no. 3, pp. 696–704, Feb. 2014.
- [204] S. Balme, T. Ma, E. Balanzat, and J.-M. Janot, ‘Large osmotic energy harvesting from functionalized conical nanopore suitable for membrane applications’, *J. Membr. Sci.*, vol. 544, pp. 18–24, Dec. 2017.
- [205] J. Feng *et al.*, ‘Single-layer MoS₂ nanopores as nanopower generators’, *Nature*, vol. 536, no. 7615, pp. 197–200, Aug. 2016.
- [206] A. Siria *et al.*, ‘Giant osmotic energy conversion measured in a single transmembrane boron nitride nanotube’, *Nature*, vol. 494, no. 7438, pp. 455–458, Feb. 2013.
- [207] D.-K. Kim, C. Duan, Y.-F. Chen, and A. Majumdar, ‘Power generation from concentration gradient by reverse electrodialysis in ion-selective nanochannels’, *Microfluid. Nanofluidics*, vol. 9, no. 6, pp. 1215–1224, Dec. 2010.
- [208] W. Guo *et al.*, ‘Energy Harvesting with Single-Ion-Selective Nanopores: A Concentration-Gradient-Driven Nanofluidic Power Source’, *Adv. Funct. Mater.*, vol. 20, no. 8, pp. 1339–1344, Apr. 2010.
- [209] I. Vlassiouk, S. Smirnov, and Z. Siwy, ‘Ionic Selectivity of Single Nanochannels’, *Nano Lett.*, vol. 8, no. 7, pp. 1978–1985, Jul. 2008.
- [210] C. Wen, S. Zeng, Z. Zhang, and S.-L. Zhang, ‘Group Behavior of Nanoparticles Translocating Multiple Nanopores’, *Anal. Chem.*, vol. 90, no. 22, pp. 13483–13490, Nov. 2018.
- [211] E. Simoen, B. Kaczer, M. Toledano-Luque, and C. Claeys, ‘Random Telegraph Noise: From a Device Physicist’s Dream to a Designer’s Nightmare’, presented at the 26th Symposium on Microelectronics Technology and Devices (SBMicro 2011), Joao Pessoa, Brazil, 2011, pp. 3–15.
- [212] B. N. Anderson, O. N. Assad, T. Gilboa, A. H. Squires, D. Bar, and A. Meller, ‘Probing Solid-State Nanopores with Light for the Detection of Unlabeled Analytes’, *ACS Nano*, vol. 8, no. 11, pp. 11836–11845, Nov. 2014.
- [213] F. Traversi *et al.*, ‘Detecting the translocation of DNA through a nanopore using graphene nanoribbons’, *Nat. Nanotechnol.*, vol. 8, no. 12, pp. 939–945, Dec. 2013.

Acta Universitatis Upsaliensis

*Digital Comprehensive Summaries of Uppsala Dissertations
from the Faculty of Science and Technology 1825*

Editor: The Dean of the Faculty of Science and Technology

A doctoral dissertation from the Faculty of Science and Technology, Uppsala University, is usually a summary of a number of papers. A few copies of the complete dissertation are kept at major Swedish research libraries, while the summary alone is distributed internationally through the series Digital Comprehensive Summaries of Uppsala Dissertations from the Faculty of Science and Technology. (Prior to January, 2005, the series was published under the title "Comprehensive Summaries of Uppsala Dissertations from the Faculty of Science and Technology".)



ACTA
UNIVERSITATIS
UPSALIENSIS
UPPSALA
2019

Distribution: publications.uu.se
urn:nbn:se:uu:diva-384667